Rochester Institute of Technology
RIT Digital Institutional Repository

Theses

11-29-2022

Measuring Entanglement using Programmable Holograms

Jason Ziskind
jmz1040@rit.edu

Follow this and additional works at: https://repository.rit.edu/theses

Recommended Citation
Ziskind, Jason, "Measuring Entanglement using Programmable Holograms" (2022). Thesis. Rochester Institute of Technology. Accessed from

This Thesis is brought to you for free and open access by the RIT Libraries. For more information, please contact repository@rit.edu.

RIT | College of Science School of Physics and Astronomy

Measuring Entanglement using Programmable Holograms

By

Jason Ziskind

A Thesis Submitted in partial fulfillment of the requirements for the degree of Masters of Science in Physics in the

School of Physics and Astronomy
College of Science
Rochester Institute of Technology
Rochester, NY

Date: November 29, 2022

Approved by:_____

George Thurston, Ph.D — Date
Director, Physics

RIT | College of Science
School of Physics and Astronomy

CERTIFICATE OF APPROVAL

MASTER'S DEGREE THESIS

The Master's Degree Thesis of *Jason Ziskind* has been examined and approved by the thesis committee as satisfactory for the thesis requirement for the Master's degree in Physics.

Dr. Gregory Howland, Thesis Advisor

Dr. Edwin Hach, Committee Member

Dr. George Thurston, Committee Member

Dr. Benjamin Zwickl, Committee Member

Date_____

Dedication

First and foremost, I'd like to thank my teammates, you guys are my family. Thank you, Mrs. Visca, Mr. Dykstra, and Mr. Fagan for introducing me to physics and computer science. Thank you John "Blue" Mooney for introducing me to Burair Kothari, my time as a tutor transformed my life. Thank you Caleb, Dan, Logan, and Nash for being great friends and classmates. Thank you, Dr. Ed Hach and Dr. Michael Kotlarchyk for setting up my first physics research experience. I'd like to thank the entire quantum optics research group for technical support throughout this project. A big thanks to my advisor Dr. Greg Howland for their support, inspiration, and flexibility to allow me to produce a piece of work that I am proud of and represent our team in the lab and the physics department at RIT. Thank you to my parents for all the support, thanks Dad for helping set up that laser.

peace, love, and Run Fast

Abstract

The Einstein–Podolsky–Rosen (EPR) paradox proposes an entangled quantum state in high dimensional non-commuting observables, position and momentum. We experimentally demonstrate a novel method for measuring spatial correlations in joint position and joint momentum space for entangled photons in an EPR-like state. Research in the field of quantum optics can provide insight into quantum information processing, communication, quantum key distribution, and further investigation into the EPR paradox and locality. Unlike existing techniques, we take measurements of non-commuting observables using a static configuration. A 405nm pump laser incident on a Bismuth Borate nonlinear crystal produces an EPR state as a pair of 810nm photons through the process of spontaneous parametric downconversion. To measure spatial correlations, we take advantage of holograms displayed on digital micromirror devices (DMDs). This method allows for control over the basis that is measured only by changing what hologram is displayed on the DMD, without having to add lenses or other bulk optic components. The field interaction that generates a hologram can be computationally simulated and displayed on the DMD allowing for a momentum mode projection onto the incident state. Collection of joint position and joint momentum correlations provide an entanglement witness. Verification of entanglement using this technique provides the framework to investigate projections onto arbitrary states and explore further quantum communication advances.

Contents

List of Figures

List of Tables

Chapter 1

Introduction

This thesis presents a proof-of-concept experiment showing that entanglement can be observed using a digital micromirror device to perform holographic quantum state projections. A nonlinear crystal is the source of entangled photons. The position and momentum of photons were measured and calculations were performed to determine that the photons are in fact entangled. The novel technique presented is the use of holograms to measure the momentum distribution of the entangled photons. There are two primary advantages of our approach. First, no physical configuration changes are needed in the experiment to change the measurement basis. The second advantage of this system is that it can be expanded to project arbitrary spatial modes. The holographic technique for the measurement of entangled systems is a new practice and we report on the practical obstacles and challenges found when using this scheme. Along with an investigation of entanglement, our experiment promotes further investigation into the use of holograms to produce arbitrary modes for use in quantum communication and information.

1.1 Entanglement

1.1.1 Einstein–Podolsky–Rosen Paradox

One of the most interesting and impactful predictions of the theory of Quantum Mechanics is quantum entanglement. Entanglement describes a quantum state that represents a system composed of multiple entities that cannot be treated separately. Both mathematically in their description and conceptually in their behavior they are not separable into individual quantum systems. Our goal is to measure the characteristics of a system and observe the presence of entanglement.

There are two important measurement properties of entangled systems. A system is said to be maximally entangled if the following criteria are met. First, the single-particle measurement outcomes are completely random. For example, in an entangled system of spin 1/2 particles, when measuring the spin value of one particle, with no regard for the other, one sees completely random results between spin up and down. Second, when a pair of measurements are taken in a particular basis on the system, known as a joint measurement, the outcomes are perfectly correlated. Perfect correlations imply perfect predictive power over the measurement outcome for one particle given knowledge of the measurement outcome of the other. In the above example, one would measure the same spin values on both particles (or opposite spin for anti-correlated systems), where the particular values measured are random. This spin 1/2 example describes a maximally entangled system, but partially entangled systems also exist, exhibiting imperfect correlations. Maximally entangled systems also exhibit maximally mixed single-particle states.

We are particularly interested in Einstein–Podolsky–Rosen (EPR) type entanglement [1]. EPR entanglement was originally proposed as a thought experiment where each particle, when measured on its own, can have any position with equal probability. When considered as a joint system, both particles will be measured to have the same exact position. The wavefunction describing this state is [1] :

$$\Psi(x_1, x_2) \propto \delta(x_1 - x_2) \tag{1.1.1}$$

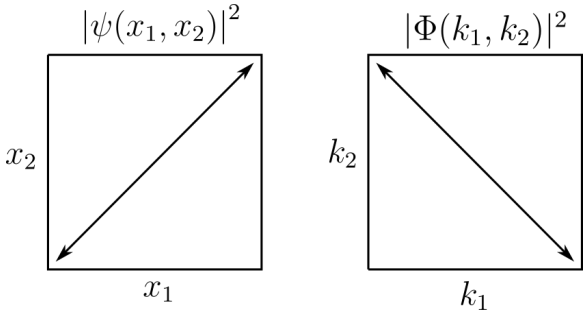

Figure 1.1: Joint position and joint momentum probability distribution for the EPR state in one dimension.

The state is infinite in extent, and infinitesimal in width as in Figure 1.1, therefore Eq. 1.1.1 can not be normalized or realized in its exact form. The EPR state is maximally entangled and has perfect correlations in both position and momentum. To describe the state in the conjugate space, take the Fourier transform of Eq. 1.1.1:

$$\Phi(k_1, k_2) \propto \delta(k_1 + k_2) \tag{1.1.2}$$

In this case, the momentum correlations manifest as anti-correlations, where each particle is traveling in opposite directions. This state is highly non-separable, which is the essence of a system being mathematically entangled.

The EPR state has interesting implications. An extension of the EPR thought experiment considers two observers, Alice and Bob, who have detectors for both the position and momentum of photons that head towards them from an EPR source [2]. Alice and Bob are spatially separated. Pairs of photons are generated in such a way as to observe EPR-like entanglement, as in Figure 1.2. One is then sent toward Alice and the other toward Bob. As photons reach them, they can choose to measure the position of their photons. From the definition of maximally entangled systems, the individual photons will arrive with random positions. Now consider that Alice measures the position of a single photon as it arrives and records its value. Given that Alice's and Bob's photons are entangled, Alice instantaneously knows that Bob's photon must be in an eigenstate of position, particularly the same random eigenstate that she measured. Alice could instead measure the momentum of her photons, obtain a value, and

Figure 1.2: Thought experiment to demonstrate EPR paradox. Alice and Bob can choose which measurements are being performed on their incoming particles.

conclude that Bob's particle must be in an eigenstate of momentum as well. The EPR state has the property that given a position measurement outcome of particle 1, there is perfect predictive power of the position measurement outcome of particle 2. The same relationship exists for measurements in the momentum basis, regardless of the separation of the observers [2].

Schrodinger called the ability to determine the eigenstate of the nonlocal particle that results from Alice and Bob's demonstration "steering" [2]. This thought experiment begs the question, if Bob's particle is in the eigenstate of the basis Alice chose to measure, how did Bob's particle "know" what kind of eigenstate to be in without information traveling between the parties? In accordance with the no signaling theorem, this scheme cannot be used to transmit information *faster* than the speed of light [3]. It is only when Alice and Bob meet up or communicate on a classical channel that they can combine their random single-particle measurements and obtain the measurement of the joint behavior of the particles, resulting in correlations. The paradoxical nature of the EPR situation *does* describe the conflict between the predictions of Quantum Mechanics and the predictions of locality. Locality is the idea that all cause-and-effect relationships only flow from positions that occupy the past light cone of a point in the present. An event in the present can only affect or send information to positions within its future light cone.

For a single particle, predictions of measurement outcomes of both position and momentum are limited by the uncertainty relation $\Delta x \Delta p \geq \frac{\hbar}{2}$ [4]. According to Quantum Mechanics, this limitation applies to all single-particle measurement predictions and is known as the Heisenberg uncertainty principle for position and momentum.

The Heisenberg uncertainty principle restricts single-particle measurement predictions, yet there are perfect predictive correlations in an EPR system. This is the root of the conflict between Quantum Mechanics and locality. Both the relationship attributed to single particle

uncertainties and joint uncertainties are valid within the theory of Quantum Mechanics, but a local description of the universe does not allow for both to be true. As proposed by Einstein, Podolsky, and Rosen there may be a more fundamental theory than Quantum Mechanics to describe this phenomenon that only includes local variables, which resolves the paradox. The alternative resolution is that the universe is nonlocal. The Bell inequality is a tool used to show there must be non-locality in the universe [5]. Bell shows that there is limited non-locality in the universe which is limited by the no-signaling theorem. We can look at the uncertainty relations quantitatively to further investigate the paradox.

The EPR paradox describes the incompatibility between a local universe and Quantum Mechanics being a complete description of reality. Entanglement is a quantum phenomenon that provides evidence against a local universe. Bell developed a theory-independent test of locality that further supports the incompatibility of Quantum Mechanics and locality [5]. Along with developing our fundamental understanding of the universe, nonlocality in quantum mechanics has implications for use in quantum information processing and secure communication [6] [7].

One cannot think of an entangled system as two individual systems, but it must be treated as a single system even when the constituent parts are not located in the same place. The measurement of the joint position and joint momentum that results in strong correlations indicates the observation of entanglement. A joint measurement is the consideration of the results of measurements on the set of observables $(\hat{x_1}, \hat{x_2})$ or $(\hat{k_1}, \hat{k_2})$.

The goal of our experiment is to make the joint measurements needed to observe correlations in a state that has EPR-like properties. Our experiment will generate a spatial EPR-like state. We show observation of both joint position and joint momentum correlations. A novel holographic technique is used to observe the joint momentum correlations. The realizable state that models the EPR paradox we employ is investigated in detail in Section 2.3. Measurements of strong correlations *along* with the closing of any loopholes described by Brunner et al. are the necessary procedures needed to properly witness entanglement [5].

We are interested in the uncertainty relation in terms of the incompatible, non-commuting,

Fourier transform pair: position and linear momentum. Other observable pairs could also be investigated in a similar way, such as orbital angular momentum modes. This thesis aims to realize an EPR-like state and make position and momentum measurements where correlations provide evidence of entanglement.

1.2 Related Work

Extensions of this research involving the use of position and momentum modes as well as the projection of arbitrary modes have implications in quantum communication and security. Various bases can be used to implement security protocols and investigate future quantum communication methods. Rather than two-state systems like spin $\frac{1}{2}$ or polarization systems, spatial variables such as position and momentum can be used to encode information. This is typically done where a particle's positions or momentum form a unit of information called a "qubit", the quantum analog of a classical computer bit. Qubits can relay information by taking advantage of the quantum properties of particles to impose security [8] [9]. Neves et al. provide a scheme to generate qudits (d dimensional qubits) using entangled photons [10]. Similarly, Solis-Prosser et al. use spatial light modulators to encode information in transverse momentum and position modes [11]. Continuous Variable Quantum Key Distribution involving the electric field operators to encode information is also gaining popularity [12]. Our research can provide a framework to either further investigate the use of position and linear momentum for communication methods, or be expanded to implement other bases, most notably, Orbital Angular Momentum (OAM) modes. Cox and Drozdov establish the production of OAM modes through Laguerre–Gauss modes using the same device and similar techniques as we use to produce linear momentum modes [13]. Ruan et al. [14] and Cozzolino et al. [15] also implement OAM modes for Quantum Key Distribution.

The realization of EPR-like states has been done in a variety of experiments. Sundaram produces entangled pairs on a quantum chip with spectral mismatch of telecom and visible wavelength photons [16]. Courme et al. use a spontaneous parametric downconversion entanglement source to investigate entangled photons propagating through a disturbed path using

both CCD and SPAD cameras [17]. Achatz et al. certify entanglement from a telecom wavelength SPDC source [18]. Defienne et al. were able to use a type-1 SPDC source and an EMCCD camera with a unique super-resolution technique to obtain position and momentum correlations. Along with parametric down-conversion, there are other ways to develop EPR like states like four-wave mixing [19] [20] and pump-poled quasi-phase matching [20].

Chapter 2

Witnessing Entanglement and the EPR Paradox

In this chapter, we will mathematically describe a state that has EPR-like entanglement and its properties. In our case, the entangled pair consists of photons generated from the illumination of a non-linear crystal. Then we provide the theoretical framework needed to set up an experiment that observes correlations and witnesses entanglement in the state. The position and momentum of each photon are measured using techniques described in Chapter 3 and 4.

2.1 Uncertainty relations from first principles

In order to observe entanglement, the relationship between measurement outcomes of particles 1 and 2 needs to be quantified. This section aims to answer the question "What does it mean for a system to be correlated and how correlated does a system have to be to be considered entangled?". Due to the nature of the calculations used in this report, careful attention is given to the derivation involving the uncertainty principle. Given the definition of the uncertainty of an observable $\langle(\hat{\Delta A})^2\rangle = \langle\hat{A}^2\rangle - \langle\hat{A}\rangle^2$, Sakurai [21] proves that the variance of two observables is related by:

$$\langle(\hat{\Delta A})^2\rangle\langle(\hat{\Delta B})^2\rangle \geq \frac{1}{4}|\langle[\hat{A},\hat{B}]\rangle|^2 \tag{2.1.1}$$

by invoking the Schwartz inequality and properties of Hermitian / Anti-Hermitian operators. One can predict the values of measurement results from compatible observables with arbitrary precision simultaneously, limited only by practical measurement techniques. For incompatible observables, which do not commute, "how much" they don't commute relates to the uncertainty in predictions of measurement outcomes of those observables [4]. We are interested in spatial degrees-of-freedom of photons, position ($\hat{x}$) and linear momentum ($\hat{p}$). The canonical commutation relation $[\hat{x},\hat{p}] = i\hbar$ can be shown as the result of momentum being the generator of translation [21]. Substituting $A \to x$ and $B \to p$ into Eq. 2.1.1:

$$\langle(\hat{\Delta x})^2\rangle\langle(\hat{\Delta p})^2\rangle \geq \frac{\hbar^2}{4} \tag{2.1.2}$$

It is convenient to refer to the wave vector $\vec{k} = \frac{\vec{p}}{\hbar}$. The Heisenberg uncertainty principal[4] is written as:

$$\langle(\hat{\Delta x})^2\rangle\langle(\hat{\Delta k})^2\rangle \geq \frac{1}{4} \tag{2.1.3}$$

For a quantum system comprised of a single particle, Eq. 2.1.3 describes the limit on the predictions we can make on the measurement outcomes of position and momentum. Consider a quantum system comprised of two particles. Any observables that act on particle 1 commute with the observables that act on particle 2:

$$[\hat{x_1},\hat{x_2}] = [\hat{k_1},\hat{k_2}] = 0 \tag{2.1.4}$$

$$[\hat{x_i},\hat{k_j}] = i\delta_{i,j} \tag{2.1.5}$$

The particular operators $\hat{x_1} \pm \hat{x_2}$ and $\hat{k_1} \pm \hat{k_2}$ are of interest for EPR-like states because measurements of these observables have the possibility to show correlations between the two

particles. For the ideal EPR state Eq. 1.1.1, a measurement of $\hat{x_1} - \hat{x_2}$ and $\hat{k_1} + \hat{k_2}$ results in zero, this is an important property of the EPR state.

The uncertainty relation between the sum and difference of position and momentum operators can be found by evaluating $[\hat{x_1} \pm \hat{x_2}, \hat{k_1} \pm \hat{k_2}]$ and $[\hat{x_1} \pm \hat{x_2}, \hat{k_1} \mp \hat{k_2}]$ using Eq. 2.1.4 and 2.1.5 and substituting the corresponding operators and results into Eq. 2.1.1. With $\langle(\Delta\hat{O})^2\rangle$ denoted as $\sigma^2_{\hat{O}}$, the relevant uncertainty relations are:

$$\sigma^2_{x_1-x_2}\sigma^2_{k_1+k_2} \geq 0 \tag{2.1.6}$$

$$\sigma^2_{x_1+x_2}\sigma^2_{k_1-k_2} \geq 0 \tag{2.1.7}$$

$$\sigma^2_{x_1+x_2}\sigma^2_{k_1+k_2} \geq 1 \tag{2.1.8}$$

$$\sigma^2_{x_1-x_2}\sigma^2_{k_1-k_2} \geq 1 \tag{2.1.9}$$

In general Quantum Mechanics allows for systems that obey the above relations. Quantum Mechanics doesn't necessarily tell us whether a system that can saturate these relations exists or what it might look like. Of these relations, Eq. 2.1.6 will be of interest for the EPR state described in Chapter 1. According to Quantum Mechanics, the restrictions on predictions of measurement outcomes for joint systems is different than the restrictions for single particle measurement predictions. The above inequalities describe the joint uncertainties, while predictions of single-party measurements are restricted by the uncertainty principle Eq. 2.1.3 [4].

Restrictions on our ability to make predictions about measurement outcomes differ between Quantum Mechanics and a local theory. A local theory predicts that a state is entirely defined by its past, all events in the past that could have sent information no faster than the speed of light to the state [22]. Consider particle 1 is outside the light cone of particle 2 and a measurement on particle 1 is made. In a local universe, the uncertainty of the measurement outcome on particle 1 conditioned on the results of some measurement on particle 2 can be no less than that of particle 1 with no conditional information. The following statement

encompasses the restrictions that locality imposes on measurement uncertainties:

$$\sigma_{x_1|x_2}\sigma_{k_1|k_2} \geq \sigma_{x_1}\sigma_{k_1} \tag{2.1.10}$$

The conditional uncertainty $\sigma_{x_1|x_2}$ is the standard deviation in the expectation value of a measurement result associated with x_1 given the measurement result of x_2. Knowledge of the measurement outcome of particle 2 should not allow for knowledge of the measurement outcome of particle 1 with any more certainty than a measurement of particle 1 itself. The independence of the uncertainty of measurements of particle 1 upon the results of measurements on particle 2 is represented by the expressions $\sigma^2_{x_1} = \sigma^2_{x_1|x_2}$ and $\sigma^2_{k_1} = \sigma^2_{k_1|k_2}$. Substitution of Eq. 2.1.10 into Eq. 2.1.3 provides the condition:

$$\sigma^2_{x_1|x_2}\sigma^2_{k_1|k_2} \geq \frac{1}{4} \tag{2.1.11}$$

for measurements taken in a local universe. Eq. 2.1.11 and mathematically equivalent forms will be referred to as an entanglement witness when violated. This is also referred to as a separability condition because all separable states must satisfy the inequality. Entanglement is witnessed when $\sigma^2_{x_1|x_2}\sigma^2_{x_1|k_2}$ is measured and found to violate the restriction stated in Eq. 2.1.10. In order to allow for the arbitrarily small uncertainty bound predicted by Quantum Mechanics for the observables $\hat{x_1} - \hat{x_2}$ and $\hat{k_1} + \hat{k_2}$, predicted by Eq. 2.1.6, to provide an entanglement witness, it is necessary to explore the relationship between $\hat{x_1} - \hat{x_2}$, $\hat{k_1} + \hat{k_2}$ and the conditional variances in the context of the EPR state.

2.2 Development of the Double Gaussian approximation to the EPR state

In this section, we will investigate the characteristics of a proposed state which provides a realization of the EPR state and can violate the local uncertainty relation. Measuring the properties of this state in the lab will allow us to estimate the uncertainty values needed to witness entanglement.

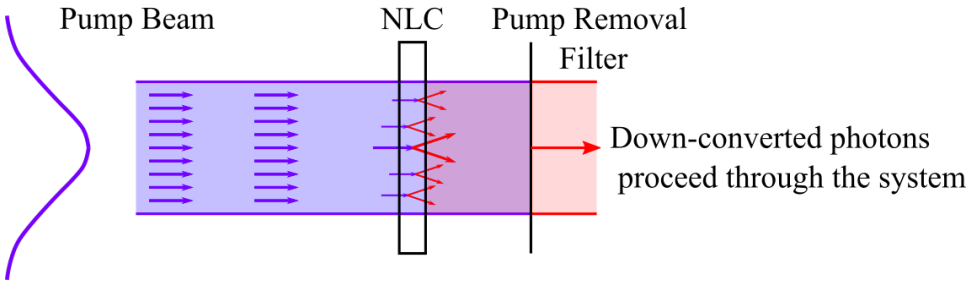

Figure 2.1: SPDC from an incident laser on a NLC.

Since creating an ideal EPR state is impossible due to its infinite extent and infinitesimal width, we aim to create an EPR-like state in the lab. An EPR-like state is a two-particle entangled state that has strong joint correlations and finite extent. While the EPR state has zero joint conditional uncertainty and can maximally violate Eq. 2.1.11, an EPR-like state has finite non-zero joint uncertainties and can still satisfy the entanglement witness. We aim to describe the mechanisms that can produce an EPR-like state and follow with a detailed description of the corresponding wave function.

2.2.1 Generation of Entangled Photons

We can create an EPR-like state in the lab by producing a pair of entangled photons from a non-linear crystal. Nonlinear crystals are able to change the color of light that interacts with them. When a nonlinear material is illuminated by an oscillating electric field, the response of the polarizability of the material is [20]:

$$\vec{P} = \chi^{(1)}\vec{E} + \chi^{(2)}\vec{E}^2 + ... \tag{2.2.12}$$

The first term is the linear response of the material, which exhibits a polarization that oscillates with the same frequency as the incident field. Higher-order interactions also take place. The field of nonlinear optics encompasses special materials with appreciable χ^n, $n \geq 2$ values. These materials have higher-order responses and exhibit interesting behavior. Some second-order responses, such as second harmonic generation or sum and difference frequency generation can be described by classical EM theory [20]. We use a second-order interaction

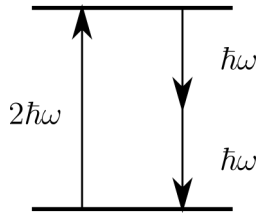

Figure 2.2: Energy diagram for degenerate down conversion.

called Spontaneous Parametric Down Conversion. Spontaneous Parametric Down Conversion (SPDC) can only be described by a quantum theory, as it requires energy present in the vacuum state [20] [23].

SPDC is the second-order process where one high-energy photon is converted into two lower-energy photons. Consider the incident photon "pump", and the outgoing photons "signal" and "idler". Most photons pass through the material without interacting in a nonlinear manner, this is due to the relatively low value of the second-order susceptibility values compared to the linear term. The interaction is probabilistic in nature so we can not predict which individual photons will be down-converted, hence the term spontaneous. Down conversion can take place in a variety of ways depending on the material and the characteristics of the incident light. Different photon polarization, wavelength, and propagation directions can allow down conversion to occur. Type 1 SPDC is when the output photons have the same polarization, which is orthogonal to the input. The term "collinear" describes SPDC signal and idler momentum distributions centered on the same optical axis. Fields that satisfy the conservation of energy condition $\omega_{signal} + \omega_{idler} = \omega_{pump}$ can provide SPDC as in Figure 2.2.

Degenerate SPDC is when signal and idler fields have the same frequency. In reality, the fields exhibit a bandwidth of frequencies centered on $\omega_{pump}/2$ such that the condition is satisfied by a small band of frequencies. Although the relative probability of SPDC is low, for Type 1 SPDC, it is significant enough for us to detect in this experiment. Generally, 100kHz to 1MHz pair rates can be routinely produced, see Section 3.1.2 Figure 3.4.

2.2.2 Phase matching

SPDC can only occur when the lattice of the material is oriented so the interaction can conserve total momentum [20][24][25]:

$$\vec{k}_{signal} + \vec{k}_{idler} = \vec{k}_{pump} \tag{2.2.13}$$

Birefringence describes a material that has different indices of refraction depending on the polarization [20]. Which wave vectors allow SPDC to occur depends on the material, wavelength, and direction inside the crystal. The conditions that must be satisfied are called phase matching conditions and are governed by the properties of the material. In order to conserve momentum, the wave vector of the pump photon must equal the sum of signal and idler wave vectors, as in Eq. 2.2.13. SPDC is an interaction with the bulk of the material, therefore there is uncertainty in the precise location of the generation of the photon pair. This uncertainty is related to the thickness of the crystal in the direction of the pump light. The region in the material that a particular pair might be found to be generated is its birth zone. If the light leaving the material is focused using an imaging configuration, the location of the pairs is preserved, this is known as the conservation of birthplace.

For type 1 SPDC, the orientation of the material changes the angle θ. When theta is near zero and the photons travel in the same direction, this configuration is referred to as "beam-like". When theta is appreciably bigger as in Figure 2.3, the extent of the transverse momentum anticorrelations is greater and the photons leave the material in a ring shape. Configurations that allow for this are referred to as "ring-like" phase-matching conditions. Rings can be easily seen by placing a camera down the optical axis of the pump field; using wavelength bandpass filters, a ring will appear. This is a canonical indicator of down conversion.

By adjusting the angle between the plane of the material and the incident pump beam, we can change the phase-matching conditions and control the size of the ring when viewed on a camera. Whether a beam-like or ring-like state is used is determined by experimental conditions or application. The extent of the positions where the down-conversion photon

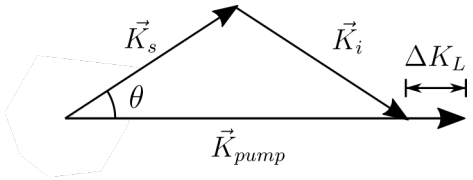

Figure 2.3: Phase matching conditions for the wave vectors involved in SPDC

pairs are generated is determined by the profile of the pump beam incident on the crystal, specifically the beam radius.

2.3 Description of SPDC State from First Principals

Largely derived by Schneeloch et al. [24], here we describe the state that is produced as a result of SPDC using a nonlinear crystal (NLC). Particularly, we aim to describe the bi-photon state that leaves a Type-1 NLC when illuminated by a pump laser. To do this, we operate in the paraxial regime. A pump laser beam that is of constant power, narrow band in frequency, and well collimated along with a thin crystal allow us to make the paraxial approximation. Since the longitudinal components of the momentum of pump, signal, and idler photons are much greater than the transverse, the crystal can be treated as a two-dimensional plane where SPDC takes place. The transverse components of position and momentum are the components that carry information about the spatial entanglement, therefore we write the spatial biphoton state in two spatial dimensions rather than three.

Under these assumptions, a wave function can be written to describe the bi-photon state that SPDC produces. Bandpass filters are optical elements that allow only light from a small band of selected wavelengths to pass. With the use of bandpass filters, we can consider only the degenerate SPDC case, $\omega_1 = \omega_2$ and $\Delta\omega = 0$. The SPDC wavefunction in the momentum representation is:

$$|\Psi_{SPDC}\rangle = C_0|0_1 0_2\rangle + C_1 \int\int d_{k_1}^2 d_{k_2}^2 \Phi(\vec{k_1}, \vec{k_2}) \hat{a}^\dagger(\vec{k_1}) \hat{a}^\dagger(\vec{k_2}) |0_1 0_2\rangle \tag{2.3.14}$$

at the plane of the crystal. $\vec{k_1}, \vec{k_2}$ are the two-dimensional transverse wave vectors of photon

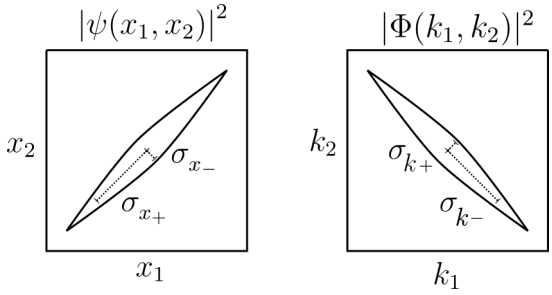

Figure 2.4: Double Gaussian approximation of the joint position and joint momentum probability distribution for the SPDC state in one spatial dimension. We use the term "extent" to refer to the breadth of modes where a distribution has a nonzero value, in this case, standard deviations σ_{x_+} and σ_{k_-} describe extent. We use the term "width" to refer to the correlation between particles 1 and 2, the standard deviation of the distribution perpendicular to the extent. In this case, σ_{x_-} and σ_{k_+} describe the correlation widths.

1 and 2. $|0_1 0_2\rangle$ is the vacuum state, $\hat{a}^\dagger$ is the creation operator for photons, $\Phi(\vec{k_1}, \vec{k_2})$ is the momentum wavefunction for the biphoton system, and C_0 and C_1 are normalization constants. Schneeloch et al. [24] use the mismatch in momentum conservation described by ΔK_z, phase matching conditions, and the collinear characterization to write a wave function to describe the SPDC state, which can be found in Appendix A. The wavefunction that represents the state of the bi-photon system at the plane of the crystal can be approximated by a double Gaussian distribution.

Figure 2.4 shows the characteristics of the Double Gaussian approximation. Similar to the ideal EPR state, the SPDC state has correlations in the position and anti-correlations in the momentum of the particles. Unlike the ideal EPR state, the SPDC state is finite in extent and has a non-zero correlation width. Although the true SPDC state is not separable in x and y, the Double Gaussian approximation is, therefore we can proceed in one spatial dimension. It is convenient to write the Double Gaussian approximation to the SPDC state in terms of the rotated coordinates :

$$k_\pm = \frac{k_1 \pm k_2}{\sqrt{2}} \tag{2.3.15}$$

$$x_\pm = \frac{x_1 \pm x_2}{\sqrt{2}} \tag{2.3.16}$$

The approximation to the SPDC wavefunction can then be written as :

$$\Phi(k_+, k_-) = N_k \exp\left(-\frac{k_-^2}{4\sigma_{k-}^2}\right) \exp\left(-\frac{k_+^2}{4\sigma_{k+}^2}\right) \tag{2.3.17}$$

$$\Psi(x_+, x_-) = N_x \exp\left(-\frac{x_-^2}{4\sigma_{x-}^2}\right) \exp\left(-\frac{x_+^2}{4\sigma_{x+}^2}\right) \tag{2.3.18}$$

From the Fourier transform relationship between Eq. 2.3.17 and 2.3.18 we can relate the width of the Gaussian distributions as :

$$\sigma_{x-}^2 = \frac{1}{\sigma_{k-}^2} \qquad\qquad 2\sigma_p^2 = \sigma_{x+}^2 = \frac{1}{4\sigma_{k+}^2} \tag{2.3.19}$$

where σ_p is the pump radius in position space, defined as the standard deviation of $\frac{x_1+x_2}{2}$. This is the mathematical description, using the double Gaussian approximation, of the spatial state the biphoton system exhibits at the crystal. σ_{k-} and σ_p are the uncertainties that can be calculated from the parameters of an experimental configuration. σ_{k-} describes the extent of momentum modes encompassed by the SPDC state due to phase matching conditions, which limits the correlation width σ_{x-} in conjugate position space. σ_p describes the extent of the position modes encompassed by the SPDC state. The extent of the allowed positions is directly related to the area of the crystal illuminated by the pump beam. σ_p then limits the correlation width in momentum space due to the Fourier transform relationship. We now have a fully determined representation of the predicted state at the plane of the crystal according to nonlinear interactions, conservation of energy, phase-matching conditions, and Quantum Mechanics.

The probability distributions associated with Eqs. 2.3.17 and 2.3.18 are:

$$P_k(k_+,k_-) = |\Phi(k_+,k_-)|^2 = N_k^2 \exp\left(-\frac{k_-^2}{2\sigma_{k_-}^2}\right)\exp\left(-\frac{k_+^2}{2\sigma_{k_+}^2}\right) \tag{2.3.20}$$

$$P_x(x_+,x_-) = |\Psi(x_+,x_-)|^2 = N_x^2 \exp\left(-\frac{x_-^2}{2\sigma_{x_-}^2}\right)\exp\left(-\frac{x_+^2}{2\sigma_{x_+}^2}\right) \tag{2.3.21}$$

Substituting the definition of the rotated coordinate systems into Eqs. 2.3.20 and 2.3.21 yields the following:

$$\Phi(k_1,k_2) = N_k \exp\left(-\frac{(k_1-k_2)^2}{8\sigma_{k_-}^2}\right)\exp\left(-\frac{(k_1+k_2)^2}{8\sigma_{k_+}^2}\right) \tag{2.3.22}$$

$$\Psi(x_1,x_2) = N_x \exp\left(-\frac{(x_1-x_2)^2}{8\sigma_{x_-}^2}\right)\exp\left(-\frac{(x_1+x_2)^2}{8\sigma_{x_+}^2}\right) \tag{2.3.23}$$

$$P_k(k_1,k_2) = N_k^2 \exp\left(-\frac{(k_1-k_2)^2}{4\sigma_{k_-}^2}\right)\exp\left(-\frac{(k_1+k_2)^2}{4\sigma_{k_+}^2}\right) \tag{2.3.24}$$

$$P_x(x_1,x_2) = N_x^2 \exp\left(-\frac{(x_1-x_2)^2}{4\sigma_{x_-}^2}\right)\exp\left(-\frac{(x_1+x_2)^2}{4\sigma_{x_+}^2}\right) \tag{2.3.25}$$

The rotated coordinates represent nonlocal quantities due to the fact that each coordinate carries information about both particles. The variance when written here is important in establishing the Fourier transform relationship. In Section 2.4 the connection between the variance of the SPDC state and the entanglement witness is made.

Written in this form, we see the connection between the SPDC state and the EPR state. As $\frac{\sigma_{x_-}}{\sigma_{x_+}} \to 0$ and $\frac{\sigma_{k_+}}{\sigma_{k_-}} \to 0$, the double Gaussian approximation approaches the ideal EPR state. In other words, as the correlation widths σ_{x_-} and σ_{k_+} go to zero the extents of the correlations go to infinity.

2.4 Connecting Uncertainty and the Double Gaussian Approximation

The double Gaussian approximation allows us to investigate the conflict between quantum mechanics and locality. As discussed in Section 2.1, a local theory predicts the restriction $\sigma^2_{x_1|x_2}\sigma^2_{k_1|k_2} \geq \sigma^2_{x_1}\sigma^2_{k_1} \geq \frac{1}{4}$. Quantum Mechanics predicts an arbitrarily small variance product $\sigma^2_{x_1-x_2}\sigma^2_{k_1+k_2}$. We also have a model for an entangled EPR-like state in terms of $\sigma^2_{x_-}$ and $\sigma^2_{k_+}$. The aim of this section is to clearly state the connections needed to measure the joint space for the SPDC state and observation of entanglement.

Given we can measure the probability distributions Eqs. 2.3.24 and 2.3.25, estimates for $\sigma^2_{x_\pm}$ and $\sigma^2_{k_\pm}$ can be obtained. These estimates can then be related to the entanglement witness as follows.

First:

$$\sigma_{x_\pm} = \frac{\sigma_{x_1 \pm x_2}}{\sqrt{2}} \tag{2.4.26}$$

$$\sigma_{k_\pm} = \frac{\sigma_{k_1 \pm k_2}}{\sqrt{2}} \tag{2.4.27}$$

can be found by invoking the definition of the rotated coordinate system. Alternatively, explicit calculation of the variance of sums and differences in terms of the covariance using properties of the double Gaussian distribution can be done [24]. Using Eqs. 2.4.26, 2.4.27, and measurements of $P_k(k_1, k_2)$ and $P_x(x_1, x_2)$, the value of $\sigma_{x_-}\sigma_{k_+}$ can be transformed to yield a value for $\sigma_{x_1-x_2}\sigma_{k_1+k_2}$.

The relationship between $\sigma^2_{x_1-x_2}\sigma^2_{k_1+k_2}$ and $\sigma^2_{x_1|x_2}\sigma^2_{k_1|k_2}$ can be found by further application of the properties of the double Gaussian distribution [24], such as :

$$\sigma^2_{x_1|x_2} = \frac{2\sigma^2_{x_+}\sigma^2_{x_-}}{\sigma^2_{x_+} + \sigma^2_{x_-}} \tag{2.4.28}$$

Substitute Eqs. 2.4.26 into Eq. 2.4.28:

$$\sigma^2_{x_1|x_2} = \frac{2\left(\frac{\sigma^2_{x_1+x_2}}{2}\right)\left(\frac{\sigma^2_{x_1-x_2}}{2}\right)}{\left(\frac{\sigma^2_{x_1+x_2}}{2}\right)+\left(\frac{\sigma^2_{x_1-x_2}}{2}\right)} \tag{2.4.29}$$

$$\sigma^2_{x_1|x_2} = \frac{\sigma^2_{x_1+x_2}\sigma^2_{x_1-x_2}}{\sigma^2_{x_1+x_2}+\sigma^2_{x_1-x_2}} \tag{2.4.30}$$

Since $\frac{\sigma^2_{x_1+x_2}}{\sigma^2_{x_1+x_2}+\sigma^2_{x_1-x_2}} \leq 1$, then:

$$\sigma^2_{x_1-x_2} \geq \sigma^2_{x_1|x_2} \tag{2.4.31}$$

Eq. 2.4.31 is true independent of the specific joint distribution. For momentum, the same steps can be taken:

$$\sigma^2_{k_1|k_2} = \frac{\sigma^2_{k_1+k_2}\sigma^2_{k_1-k_2}}{\sigma^2_{k_1+k_2}+\sigma^2_{k_1-k_2}} \tag{2.4.32}$$

then $\frac{\sigma^2_{k_1-k_2}}{\sigma^2_{k_1+k_2}+\sigma^2_{k_1-k_2}} \leq 1$ and:

$$\sigma^2_{k_1+k_2} \geq \sigma^2_{k_1|k_2} \tag{2.4.33}$$

Substituting Eq. 2.4.31 and 2.4.33 into the separability condition Eq. 2.1.11, the entanglement witness can be written :

$$\sigma^2_{x_1-x_2}\sigma^2_{k_1+k_2} \geq \frac{1}{4} \tag{2.4.34}$$

The SPDC state is a valid candidate to witness entanglement because it occurs in the regime where $\sigma_{x_+} \gg \sigma_{x_-}$ therefore Eq. 2.4.31 is saturated. Similarly when $\sigma_{k_-} \gg \sigma_{k_+}$ then Eq. 2.4.33 is saturated.

One can also invoke Eq. 2.4.28 written as Case C in Table 2.1 with estimates for $\sigma_{x_\pm}$ and $\sigma_{k_\pm}$ and calculate the conditional uncertainty product directly. In that case, the extent of the correlations is used along with the correlation width. Eq. 2.4.34 is the preferred entanglement

	Variance	Std. Dev.
A	$\sigma^2_{x_1\|x_2}\sigma^2_{k_1\|k_2} \geq \frac{1}{4}$	$\sigma_{x_1\|x_2}\sigma_{k_1\|k_2} \geq \frac{1}{2}$
B	$\sigma^2_{x_1-x_2}\sigma^2_{k_1+k_2} \geq \frac{1}{4}$	$\sigma_{x_1-x_2}\sigma_{k_1+k_2} \geq \frac{1}{2}$
C	$\sigma^2_{x_-}\sigma^2_{k_+} \geq \frac{1}{16}$	$\sigma_{x_-}\sigma_{k_+} \geq \frac{1}{4}$
D	$\frac{\sigma^2_{x_-}}{\sigma^2_{x_+}} \geq \frac{1}{4}$	$\frac{\sigma_{x_-}}{\sigma_{x_+}} \geq \frac{1}{2}$
E	$\frac{\sigma^2_{k_+}}{\sigma^2_{k_-}} \geq \frac{1}{4}$	$\frac{\sigma_{k_+}}{\sigma_{k_-}} \geq \frac{1}{2}$

Table 2.1: Mathematically equivalent forms of the entanglement witnesses in the context of the double Gaussian approximation to the SPDC state. Also referred to as separability conditions since all states separable between particles 1 and 2 satisfy the inequality.

witness as it only takes into account the experimentally determined correlation widths. Details about experimental restrictions can be found in Section 3.1.7.

Table 2.1 includes the statements of entanglement witness. Given σ_{x_-} and σ_{k_+} are the experimentally determined values and all others can be derived from them, the statements in Table 2.1 are all equivalent.

Case D and E must invoke the relations in Eq. 2.3.19 and should be calculated from σ_{x_-} and σ_{k_+} alone to provide an entanglement witness. The entanglement witness we aim to employ takes into account only correlation widths. The goal of this experiment is to violate the inequality and observe entanglement using holograms as momentum projections.

Chapter 3

Measuring Spontaneous Parametric Down Conversion

3.1 Experiment

The goal of the experiment is to generate spatially entangled photon pairs and measure the joint position and joint momentum distributions. SPDC is the entangled photon source. Those photons are imaged onto the projection device. We will use Digital Micromirror Devices to project position and momentum states onto the entangled photons. The photons that pass through the projection filters are coupled into multimode fibers and detected by single photon detectors. The photodetectors are connected to a time bin correlator where the presence of entangled pairs is counted.

3.1.1 Optical Set Up

The pump photons are produced by a 405nm CUBE Coherent diode laser operating at 5-50mW [26]. A 405 nm cleanup filter is used following the laser to eliminate unwanted wavelengths of light from the beam. The pump laser is then incident on the center of a NLC. The NLC is a 3mm long Bismuth Borate (BiBO) nonlinear crystal oriented for type-I, degenerate, collinear SPDC. This means signal and idler photons will have the same polarization, the

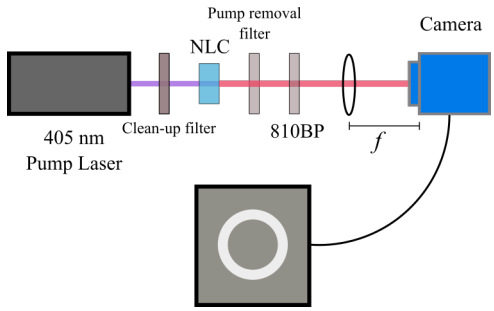

Figure 3.1: Viewing down conversion directly with the pixel fly photon sensitive camera.

same wavelength, and the same emission cone. Since the incident pump beam is 405nm, the output photon pairs have wavelengths centered on 810nm. The crystal length and orientation determine the birth zone size and phase matching conditions described in Section 2.2.2.

Consider first a simple viewing configuration for down conversion. A camera is placed directly following the NLC as in Figure 3.1. A PCO Pixelfly low light camera with up to 62% quantum efficiency is used [27]. The camera is fitted with a pump light removal filter, an 810nm band pass filter, and a lens. The lens puts the sensor of the camera in the Fourier plane of the crystal allowing us to see the momentum of the down-converted photons. This allows us to confirm the presence of down-converted photons and adjust the phase-matching conditions. By rotating the crystal, the phase matching conditions that allow for SPDC to occur inside the crystal change, and the resulting momenta of signal and idler change. The emission cones of the entangled photons narrow or widen with changes in the orientation of the crystal. A particular entangled pair of photons will be traveling with opposite transverse momenta and will appear on opposite sides of the ring in a Fourier plane image like the ones in Figure 3.2.

3.1.2 Coincidence Detection

In order to measure the entangled pairs, they need to be separated and then detected. The type of detection used for entangled optical systems is referred to as coincident detection. A beam splitter is used to separate the signal and idler photons. When the photon pair arrives at the beam splitter, each individual photon can either transmit or reflect. Coincidence detection

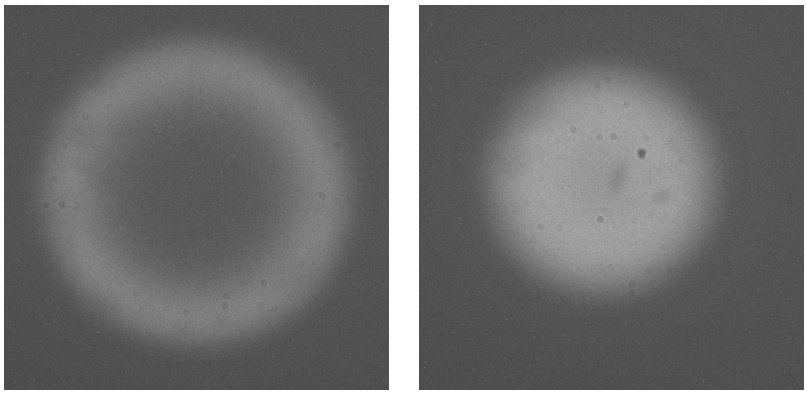

(a) (b)

Figure 3.2: Direct viewing of Down Conversion beam in ring-like (a) and beam-like (b) phase matching conditions.

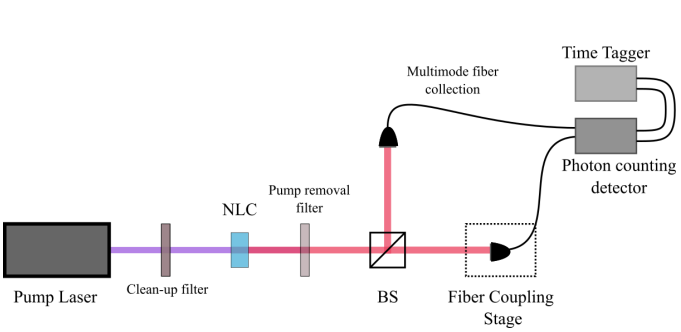

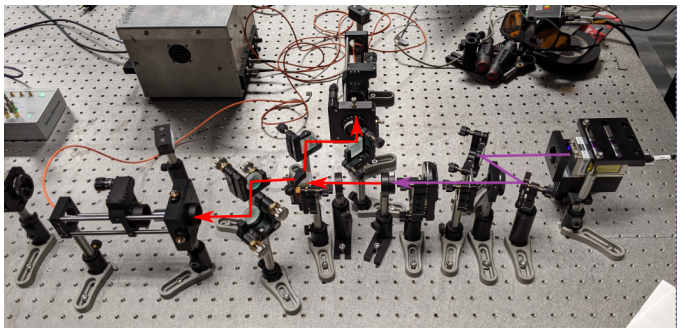

(a) (b)

Figure 3.3: Direct Coupling of Down Conversion light into photodetectors.

allows us to post-select the case where one photon is transmitted and the other is reflected.

In order to establish an initial count rate for entangled pairs that will reach the detector, coupling of all spatial modes of signal and idler will be used. In what we refer to as a "direct" coupling configuration, photons travel from the beam splitter directly to the detection device with no spatial projections or filtering. From the two output ports of the BS, signal and idler photons are guided by steering mirrors to a fiber coupler consisting of an objective lens and a multimode fiber. The two fibers are coupled into two channels of the photon detector Excelitas Single Photon Counting Module 4 Channel Array [28]. The photon detector converts the analog optical signal to an analog electrical signal. The electrical signal is connected to a Swabian Instruments Time Tagger [29], which records the arrival times of the photons and

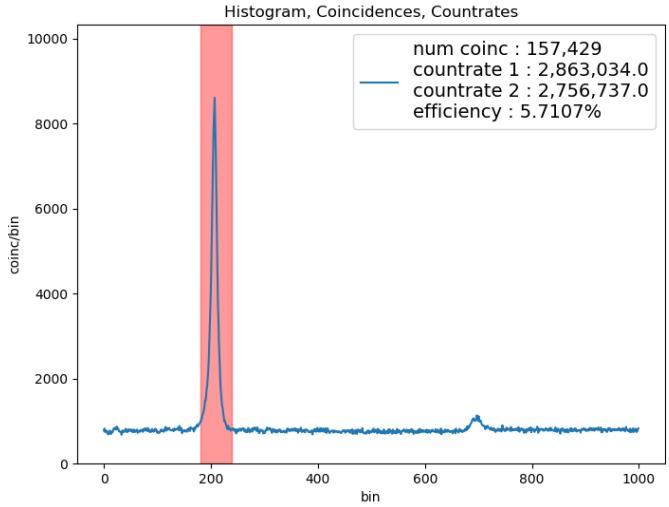

Figure 3.4: Initial Coincidence with direct fiber coupling at 5mW pump power and 0.5s acquisition time. The coincidence window is highlighted in red.

calculates the relative arrival times. This is known as a time correlation measurement and is used to interpret the analog signal and perform timing calculations. The Time Tagger provides a histogram of the relative arrival times of single photons and the single detector count rates.

Coincidence detection involves obtaining the arrival times of single photons on both arms of the experiment and determining the number of pairs versus the corresponding relative arrival times of those photons. A photon pair is generated at a single instance in time, within uncertainty, and the optical path lengths are fixed for both arms of the experiment. Therefore all photons generated from SPDC on the crystal should arrive with the same relative arrival time and are said to exhibit "coincidence". The goal of this detection scheme is to obtain a significant signal of time-correlated photons. The uncertainty in the arrival time of the photons is most significantly attributed to detector timing jitter and finite time bin resolution. All individual photons captured by the detector have random arrival times, but when calculating the relative arrival times of pairs, the intended signal can be separated from the noise. Noise includes room light, residual pump light that pass through the filters, and photon pairs that travel down the same path, which all arrive with no time correlations. We can plot a histogram of the relative arrival times of photon pairs. A significant spike in the histogram represents

photons arriving with the same relative arrival time, this is known as a coincidence peak. The number of coincidence counts is measured as a sum of coincidences in the peak. The Time Tagger Python module is used to retrieve the histogram from the device. From the histogram and singles count rates reported by the device, the coincidence rate, accidental rate, and coincidence efficiency can be calculated. The single count rate is calculated as the number of photons that are counted by the detector per second. The accidental coincidence is calculated as the average number of coincidences detected by the time correlator that do not fall within the coincidence peak, per the coincidence window we select to use on the peak. Accidental coincidences are coincidence counts that don't come from the entangled photon pairs. Efficiency is calculated as the proportion of coincidences to the (lesser) singles count rate.

The horizontal axis $t_{signal} - t_{idler}$ is in units of bins that are 100 ps wide. Coincidence window size varies throughout the experiment. Depending on the use case, a typical coincidence window is 2-4 ns wide. The quantum efficiency of the detectors is $\approx 50\%$ [28]. The dark counts, coincidence rate, and singles rates that are measured when the pump laser is powered off were found to be ≈ 700 single photon counts and ≈ 0.1 coincidence pairs per second.

In the direct detection configuration, forward alignment with an intense alignment laser is sufficient to establish the fiber coupling and capture down conversion light. A visible laser near the wavelength of the down-converted photons is directed to overlap the path of the pump beam. The alignment laser beam allows us to measure the power that travels through the fiber. Fine adjustments of the fiber tip position and the angle of the steering mirrors are made to optimize the power transmitted through the fibers. Forward alignment can provide a configuration that yields some initial coincidence which is useful because it is difficult to align the invisible weak down conversion beam without any initial coincidence to optimize. After the alignment beam power is optimized, we remove the alignment laser and perform the same adjustment procedure, this time optimizing the singles count rate and the coincidence of down-converted photons. Once coupling with no spatial projections is achieved the optical path will be adjusted to accommodate the DMDs. The DMDs will be placed in the image

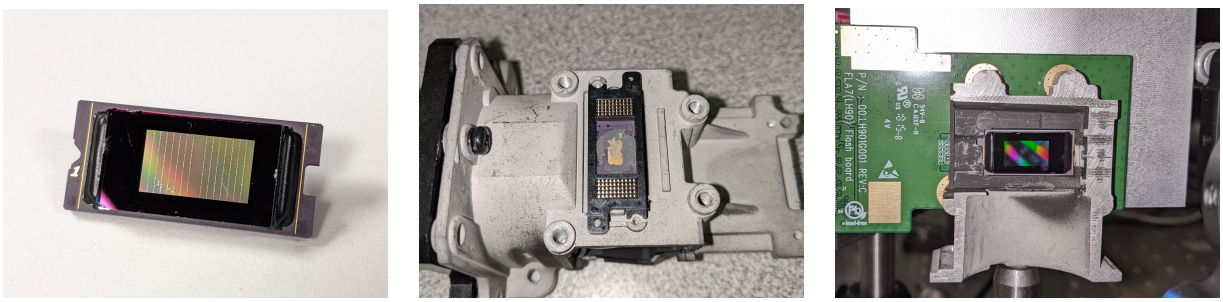

(a) (b) (c)

Figure 3.5: (a) DLP® 0.47 1080p DMD (b) DMD in original projector mount. (c) DMD mounted as a stand-alone device on a custom machined mount.

plane of the crystal where they are used to perform projections onto the state of the incident light. The introduction of the DMDs introduces loss as discussed in Section 4.2.

3.1.3 Digital Micromirror Devices

The tool used to make projections onto particular position or momentum modes is a pair of Digital Micromirror Devices (DMDs). A DMD is a digital micromirror array, in our case, a 1920x1080 grid of individually addressable actuating mirrors. The terms pixel and mirror will be used interchangeably. DMDs can be controlled as external monitors where pixel-perfect manipulation can be achieved by displaying 1920x1080 images over an HDMI display. Each pixel in an image displayed on the DMD is mapped to a mirror in either the "ON" position or the "OFF" position. For binary images where the pixels are purely black and white, the mirrors are in either the ON position or the OFF position. Although only binary images were used in this experiment, grayscale can be achieved by rapidly switching the mirror between the two positions ON and OFF. When facing the 4710 model DMD, an ON pixel is pitched 17 degrees upward in the vertical direction, and an OFF pixel is pitched 17 degrees in the horizontal direction (the right-hand side when facing the exposed mirrors) as seen in Figure 3.6. See Section 4.2 for practical considerations for light interacting with the DMD.

We used a pair of Texas Instrument DLP LightCrafter Display 4710 Evaluation Module (EVM) Gen2 devices [30]. The model of the DMD that is housed in the EVM is the DLP4710 [31]. The original product is housed in a projector where there are RGB LEDs that cycle and

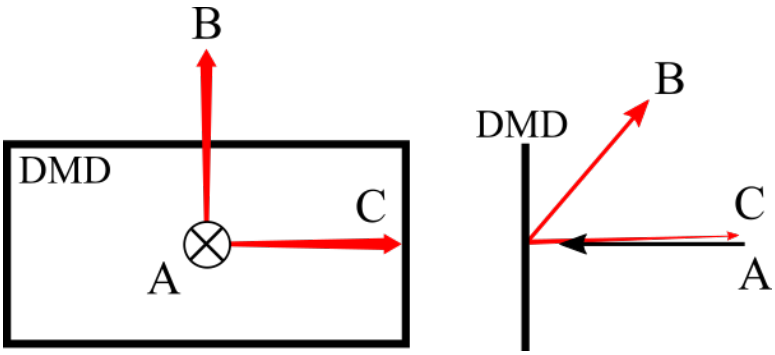

Figure 3.6: General Orientation of incoming and outgoing beams interacting with the DMD. A: an incoming beam, B: a Beam corresponding to mirrors in the "ON" state, C: a Beam corresponding to mirrors in the "OFF" state. This depiction does not include the diffractive effects of the mirror array. Distinct diffraction orders would be centered along beams B and C. See Section 3.1.5 for the extinction relationship between ON and OFF states.

illuminate the DMD. One color channel cycles at 60hz, to display RGB images the mirrors can actuate at 180hz. The DMD was removed from the EVM's projection optics and mounted as a standalone device, roughly following the procedure from Cox and Drozdov using the DLP4710 for holographic mode projection [13]. Custom software configurations were used to bypass the original use case with the LEDs connected using a USB connection.

The periodic spacing of the mirrors on the array results in a reflective diffraction grating. As seen in Figure 3.8, the diffraction occurs in both horizontal and vertical orientations because the mirrors form a two-dimensional diffraction grating.

3.1.4 DMD alignment

After confirming the coincidence from a spatially unfiltered coupling of the down conversion beams, the DMDs are installed on each arm of the experiment at the image plane using three-axis translational stages. Various techniques were used to identify the image plane and ensure the DMDs are in the image plane oriented properly. These include forward and backward propagation alignment, and image plane identification of the crystal using a camera as seen in Figure 3.7.

The individual mirrors have a diffraction effect according to $n\lambda = d\sin\theta$, where n is the order number, $d = 5.4\mu m$ is the spacing between centers of the mirrors, θ is the angle

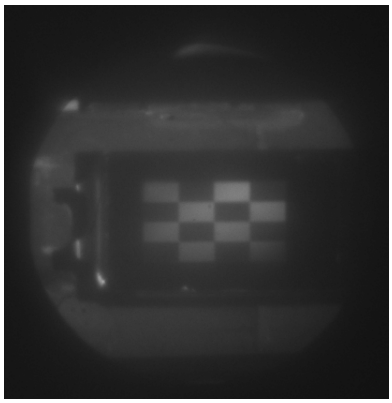

Figure 3.7: DMD showing a test pattern in focus with the aperture of the NLC illuminated by white light. A technique used to establish the DMDs location in the image plane of the crystal.

the nth order leaves the DMD relative to the normal. The diffraction occurs for spacing in both the vertical and horizontal directions. Due to the diffraction grating that the mirrors create, there will always be light occupying those diffraction orders. The orientation of the individual mirrors determines the intensity of each diffraction order. The relative intensity of the diffractive orders results from the shape of the mirrors, the diffraction grating spacing, the relative number of mirrors in ON and OFF positions, and the rectangular orientation of the array.

Of the diffraction orders of the DMD, the brightest is identified with a Thorlabs optical power monitor. This single brightest diffractive order was identified in space using an 810nm alignment laser. The other orders are found to replicate the field that is intended in the primary order but distorted by large diffraction angles. Non-primary orders will not be incident on the objective lens and not coupled into the fiber, being effectively discarded. Diffraction is an unavoidable and significant source of detected coincidence loss.

Using forward and backward propagation alignment techniques, the selected diffraction order of the 810nm down conversion beam is coupled into the fiber. The first step in establishing a coupling configuration that detects light reflected off the mirror array is to set all the mirrors in the array in a single direction. In this case, the DMDs are set to all "OFF", which reflects light incident on the DMDs to the side as in Figure 3.6.

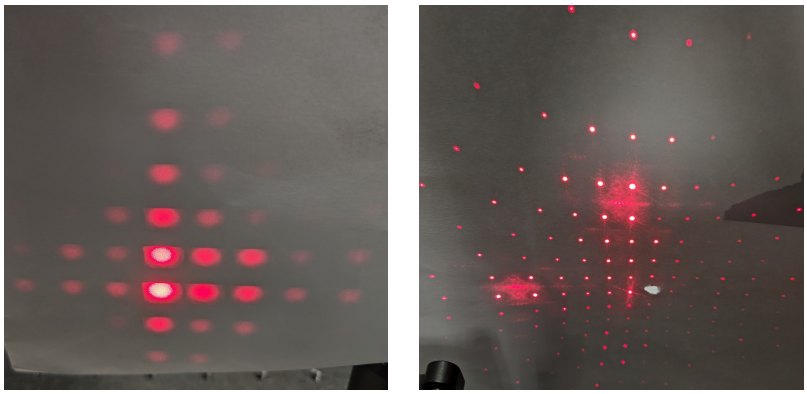

(a) (b)

Figure 3.8: (a) Diffraction pattern of DMD illuminated with an expanded beam. (b) Diffraction pattern of DMD illuminated by laser directly. Angular *spacing* of diffraction orders is constant, but the wavefront shape and intensity of the orders depend on the state of the mirror array

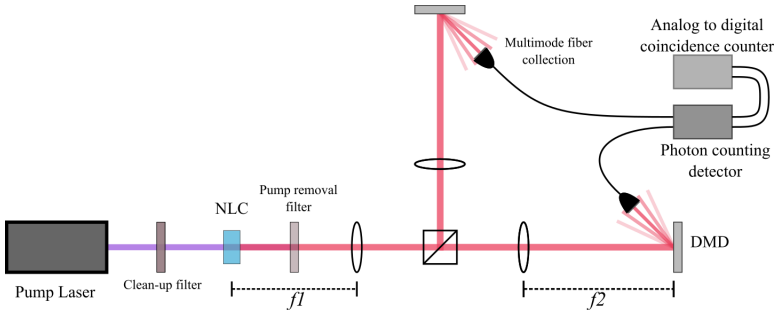

Figure 3.9: Full Experimental set up for projections of both position and momentum modes.

The steering mirrors are adjusted while the DMDs on both arms are reflecting all the incident light toward the detectors to optimize the count rates and the number of coincidences per second.

Once the fibers are properly capturing entangled photons that are reflected from the pair of DMDs, the DMDs are adjusted to maximize the portion of the two beams that are being captured. The position of the DMDs is adjusted by translating them in the plane perpendicular to the incident beam. The first technique used to verify the DMDs are in the image plane and centered on the beam properly is to "take a picture of the beam".

Power Characteristics

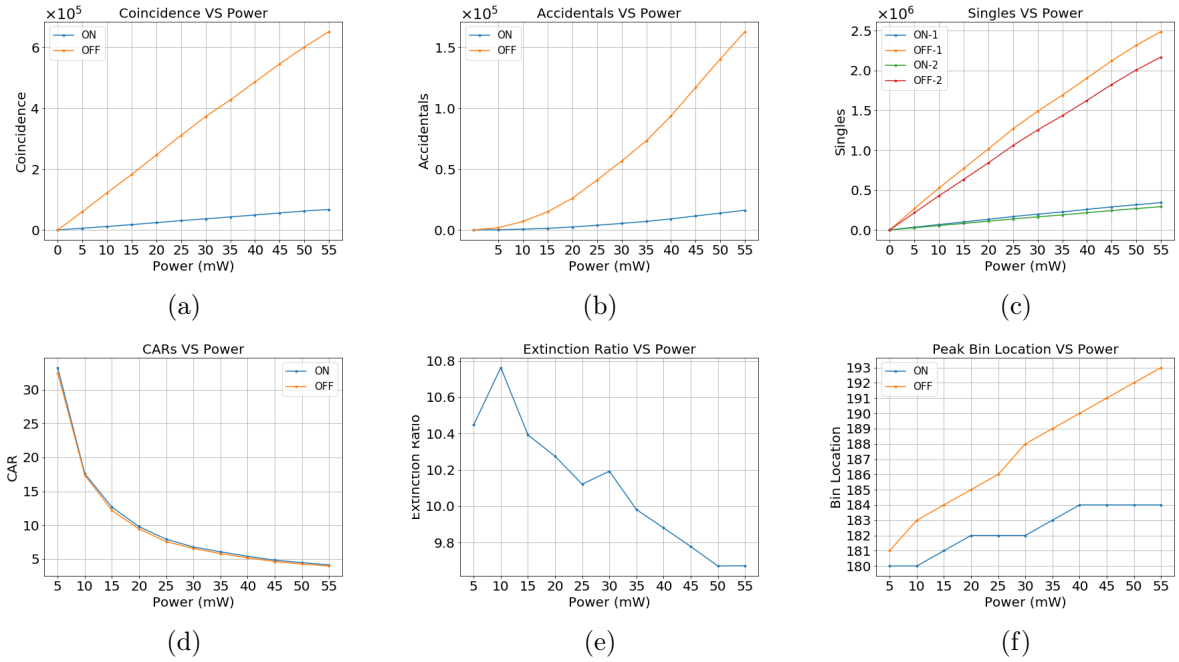

Figure 3.10: (a) Coincidence vs Power, (b) Accidental count rate vs Power, (c) Singles count rate from DMD1 vs Power, (d) CARs vs Power, (e) Extinction Ratio vs Power, (f) Peak bin location vs Power. Laser Power is recorded as the nominal power setting of the laser by remote control. Each data point is taken for 15s acquisition time. The OFF state corresponds to all black pixels (toward the detector) and the ON state corresponds to all white pixels (away from the detector). Notes : (e) Low overall extinction ratio posed a challenge for discerning the coincidence from selected states versus background coincidence. (f) The bin number of the coincidence peak changes as a function of power, requiring the coincidence window to adapt depending on the parameters of particular data set.

3.1.5 System characterization

We found that about 3% of the incident light is reflected by the DMDs in the primary diffractive order and captured by the fiber optic coupling mechanism. In general, 15s acquisition time and 45mW pump power yield the most consistent results. Accidental subtraction from the coincidence counts was used to provide a more accurate coincidence rate. The peak coincidence bin is the time bin in the time correlation detection that has the maximum coincidence count number. We found that the coincidence bin that the peak falls in depends on incident power on the detectors, likely caused by the saturation of the detectors. The coincidence window is shifted accordingly to allow for a narrow coincidence window when acquiring

Acquisition Time Characteristics

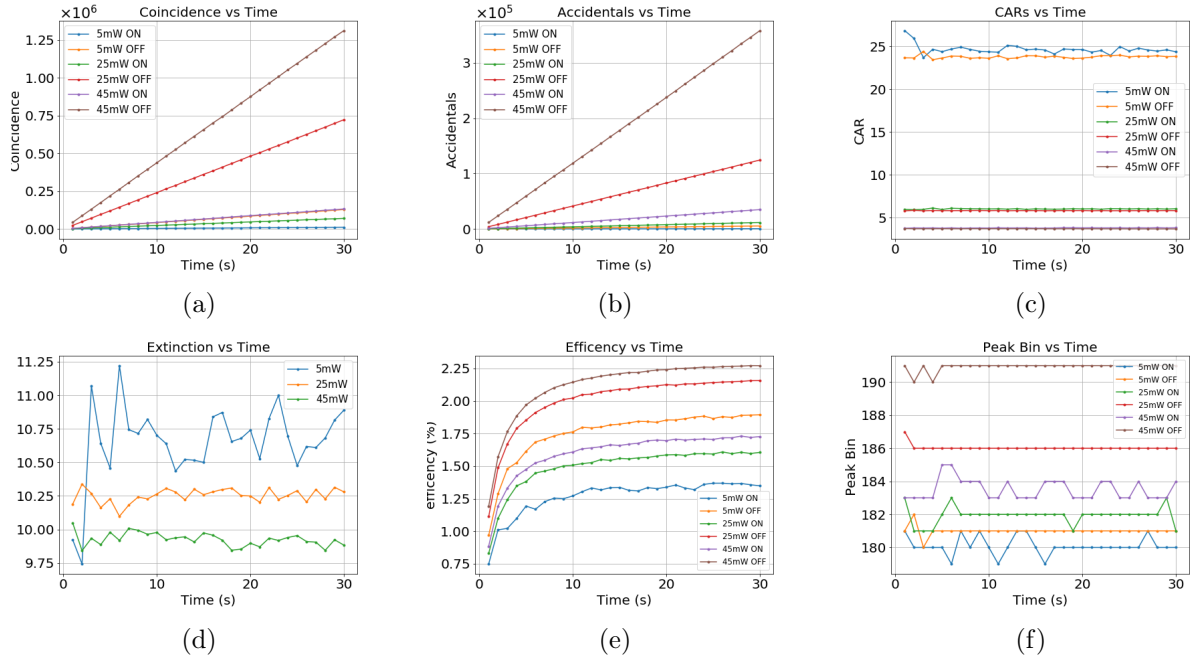

Figure 3.11: (a) Coincidence vs t_{aq}, (b) Accidental count rate vs t_{aq}, (c) Singles count rate from DMD1 vs t_{aq}, (d) CARs vs t_{aq}, (e) Extinction Ratio vs t_{aq}, (f) Peak bin location vs t_{aq}. For each t_{aq}, a data point is taken at various nominal power levels.

data. The extinction ratio for this detection scheme is calculated as the ratio of the coincidence when all the mirrors on both DMDs are in the ON position to the coincidence when all the mirrors are in the OFF position. Coincidence to Accidental Ratio (CARs), Extinction Ratio, and the coincidence peak bin are strongly dependent on the pump power.

3.1.6 Position Measurements

A position measurement is an identification of the location of a photon at the measurement plane. When the measurement plane coincides with an image plane of the crystal, a position measurement provides the birth zone of an entangled photon that results from SPDC. Combining coincidence detection and position measurements, joint positions of the entangled photon pairs can be determined. Schneeloch et al. provide a comprehensive description of the birth zone and why it is not a singular point for the pair [24]. A birth zone size is related to the uncertainty in the position of the pump photon incident on the crystal. Our goal is to use a

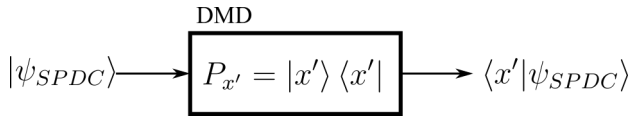

Figure 3.12: DMD acts as a sum of projection operators. The output is proportional to the amount of $|x'\rangle$, the selected position state, present in the input. Discarded components are reflected away from the detector. $|x'\rangle$ is defined in Eq. 3.1.1

device to "select" positions to pass through the system and be detected. The DMD can act as a spatial filter and be used to sort photons by position and send them either toward or away from a detector.

In order to obtain the joint position probability distribution, a measurement of the position coordinate of both signal and idler in an image plane is needed.

The position measurements we employ require the image plane of the crystal down the optical system to be identified. This will allow for a measurement of the positions of the particles at the plane of the crystal. A $f = 100mm$ lens follows the crystal, followed by a beam splitter and 2 $f = 500mm$ lenses for each output port. $M = 5$ magnification is chosen to fill the measurement device area appropriately. Since the DMD is an amplitude-only device we are only replicating the spatial intensity of the beam at the plane of the crystal, not the phase.

The type of image displayed on the DMD determines the mode that is projected onto the incident light. Since the DMD is in the image plane, coordinates on the DMD correspond to coordinates on the crystal, up to the magnification of the imaging system. The images we use to project position modes we refer to as partitions. Partitions are rectangular groups of mirrors that can be used to conceptually divide the total mirror array into various resolutions.

One-dimensional position measurements use R vertical or R horizontal partitions, see Figure 3.13. Two-dimensional measurements use a partition made up of a square group of mirrors that divide a square subspace of the total mirror array up into RxR square regions. In this experiment, a variety of resolutions are used to take position measurements, from 4x4 grids for alignment to 64x64 for high-resolution images. High-resolution patterns that use fewer mirrors per partition can result in less light coupled into the detector. Therefore high-resolution

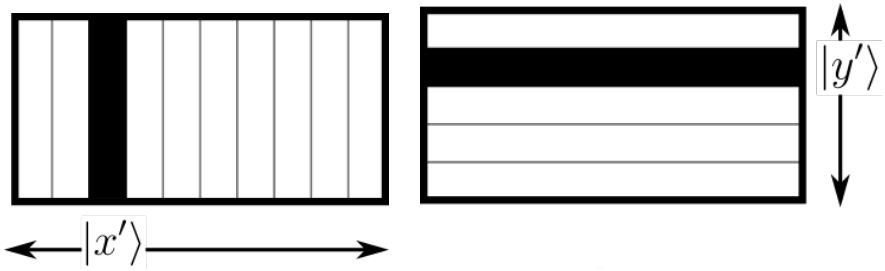

Figure 3.13: (a) The DMD display for an x measurement is a vertical slice at the chosen resolution R. (b) The DMD display for a y measurement is a horizontal slice. The color black represents mirrors oriented to reflect light toward the detector.

images require higher pump power and longer acquisition times.

The intensity of detection given a particular partition is being displayed on the DMD provides a measure of the amount of light that is incident on that partition, this is a measurement of the position of the photons at the image plane. This intensity is the coincidence detected. Note that although the DMD projects discrete partitions of positions, the analysis is continuous in position space. This is because the mirrors of the DMD select a window of positions, ignoring the space between the mirrors, within the continuous space:

$$|x'\rangle = \int_{x'-\frac{a}{2}}^{x'+\frac{a}{2}} dx|x\rangle \tag{3.1.1}$$

Where $|x'\rangle$ is the state being projected when the DMD is displaying the partition associated with the position x', and a is the width of a mirror.

When position measurements are taken in an image plane of the crystal, the spatial probability distribution for incident photons can be determined. The combination of the DMD displaying images with the fiber coupler and detectors forms a camera-like device.

3.1.7 Raster Scan Image of Down Conversion Beam

With a scheme to select positions to pass to the detector, the overall region on the DMDs that the down conversion beam is incident upon can be identified. Using a raster scan, we can "take a picture" of the incident beam on the DMDs. The main purpose of a raster scan

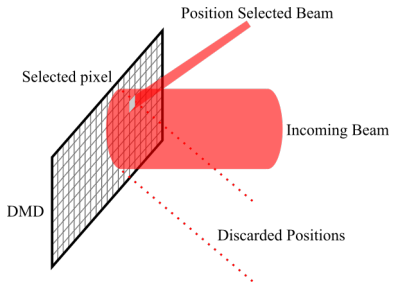

Figure 3.14: DMD interaction for position measurements

picture is to orient the DMDs. We are able to determine that the beam is incident on the center of the DMDs.

Consider all the mirrors on DMD 1 are directed toward the detector, therefore *all* the signal photons are collected. DMD 2 will raster scan over positions. A raster scan corresponds to scanning the partition over the area of the DMD and recording the coincidence per partition. We expect, from Section 2.3 that the position of the single photons and coincidence pairs is a projection of the pump beam profile and is a radially symmetric Gaussian. One-dimensional beam scans in Figure 3.15 show approximately Gaussian profiles as well as provide insight as to how much of the DMD surface we are using to interact with the incoming field. We can extend this to two dimensions and get an intensity that varies over the two-dimensional positions on the DMD, this is what we call a "beam picture". We can use the singles rates as a function of the partition position as it varies over the surface of the DMD to center up the DMD positions and make fiber coupling orientation adjustments. The coincidence as a function of partition position informs us as to how much overlap there is in the joint space between the two beams. A beam picture is the coincidence detected as one DMD scans over all possible positions and the other reflects all photons toward the detector.

Ghost images are also a useful alignment technique to allow feedback for fine DMD position adjustments in the transverse plane. Abouraddy et al. provide an excellent mathematical treatment of ghost images for a biphoton system and their uses in imaging and image processing [32]. Consider one DMD now displays a binary image with a simple pattern and the other scans over the position partitions as it did in the beam picture operation. Only coincidences from those photons that interact with the "ON" portion of the image should be detected.

One Dimensional Beam Scans using Coincidence

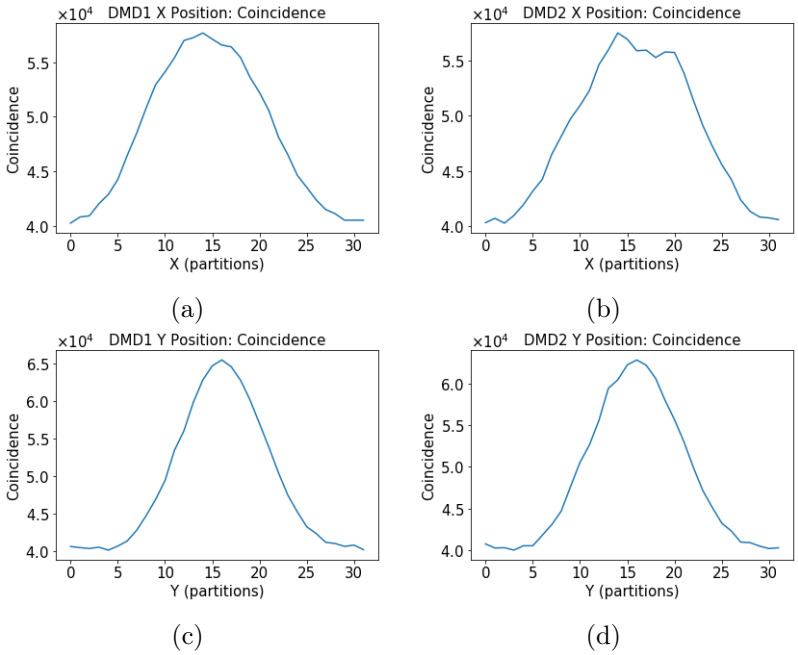

Figure 3.15: (a) One-dimensional scan over the x position on DMD 1. (b) One-dimensional scan over the x position on DMD 2. (c) One-dimensional scan over the y position on DMD1. (d) One dimensional scan over the y position on DMD 2.

In order to precisely measure the joint photon positions and the correlation width of the joint position probability distribution of the SPDC state, the DMDs need to be centered and perfectly located in the image plane dictated by the lens configuration. A cross pattern is used for alignment. 1 single partition on DMD1 should correspond to 1 single partition DMD2. When there is positional mismatch, the ghost image will be blurry. Algorithm 1 includes the pseudocode for performing a ghost image scan. R is the chosen resolution, and t_{aq} is the chosen acquisition time.

The resulting 2 dimensional coincidence array will capture the image that is displayed on DMD 2, modulated by the pump beam profile, see Figure 3.18. The cross pattern ghost image is used to line up the position of the DMDs up to the precision allowed by the coupling configuration.

The measurement of the joint position probability distribution is the overall goal of making position mode projections. The process of acquiring a joint space measurement is included in

Full Data Set Obtained from a Beam Picture

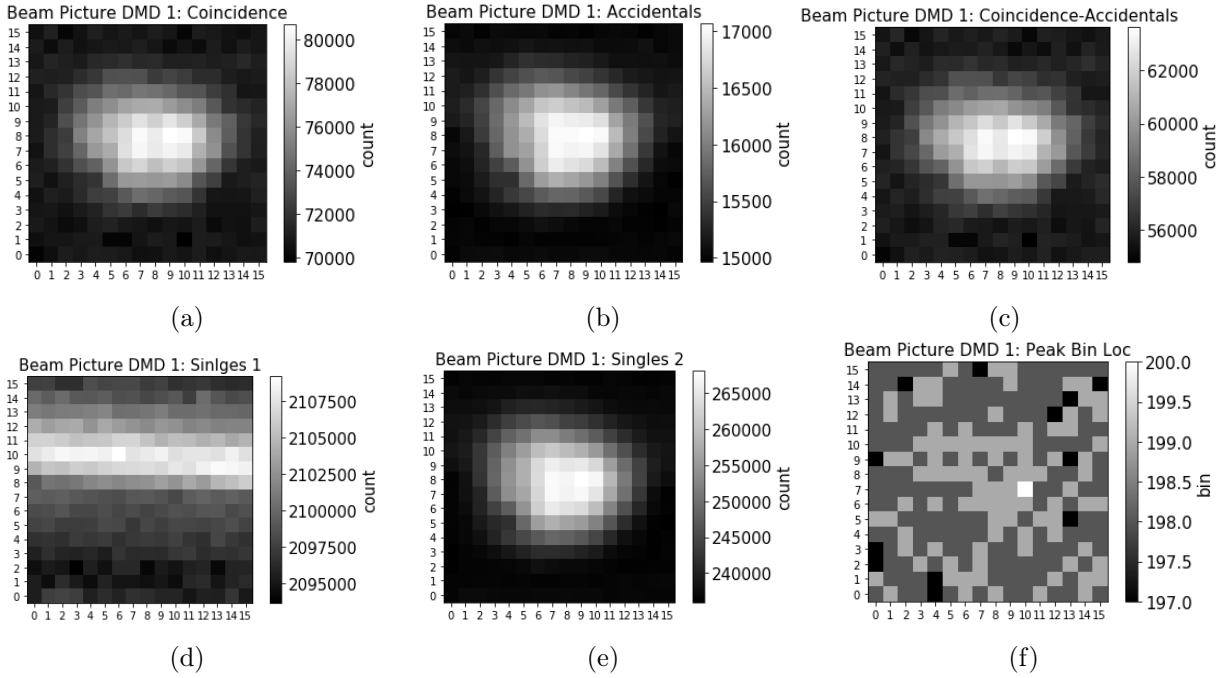

Figure 3.16: All the data collected from a beam picture, in this case using 45mW pump power and $t_{aq} = 15$. Note that for the singles rate on DMD1 we would expect a constant count since the DMD projection is not changing, but small fluctuations in pump power over time can lead to stripe patterns. Both singles rates from the scanning DMD and coincidence counts have high noise floors due to the imperfect extinction of the DMDs.

Algorithm 1 The 2 dimensional ghost imaging algorithm. Note that when the image is uniform the ghost image becomes a beam picture.

Declare data as array[R,R]
Display Ghost Image on DMD1
for x_2' in [0,R] **do**
  for y_2' in [0,R] **do**
    Display partition (x_2', y_2') on DMD2
    coinc ← Acquire Coincidence from TimeTagger for t_{aq}
    data[x_2',y_2'] ← coinc
  end for
end for

2 Dimensional Beam Pictures at Various Resolutions

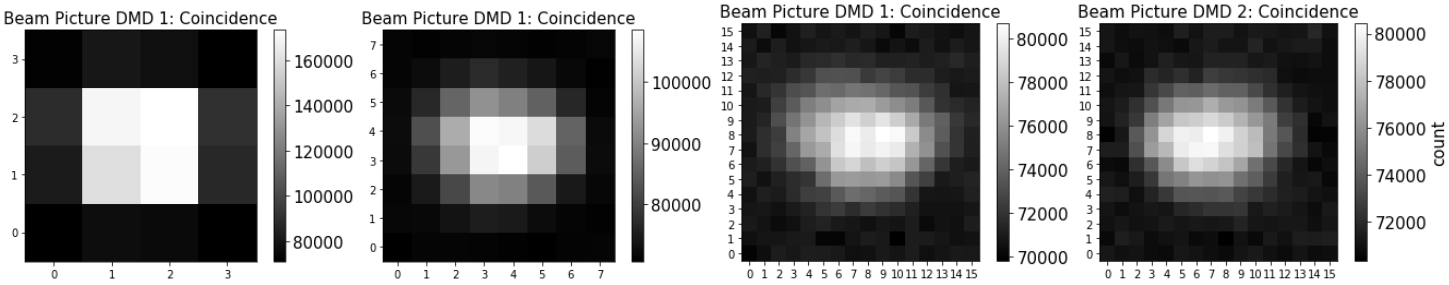

(a) (b) (c) (d)

Figure 3.17: Beam pictures at various resolutions. Figures (a)-(c) are images taken on DMD 1 while Figure (d) is taken on DMD 2. Note the alignment of the beams is relatively similar.

Ghost Images of a Cross Pattern

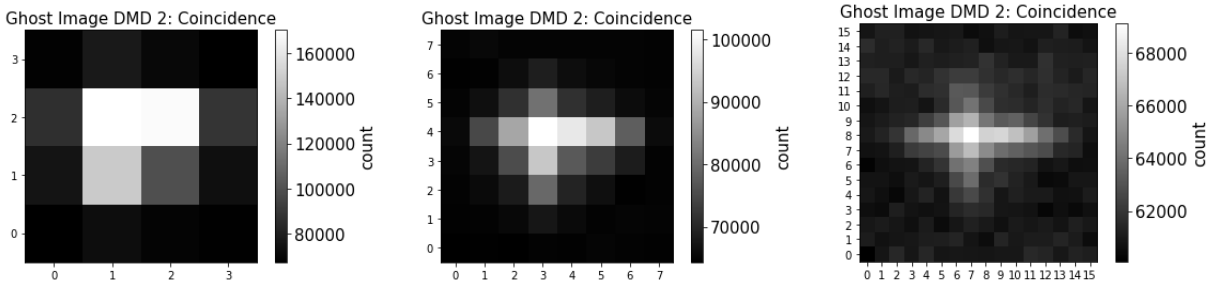

(a) (b) (c)

Figure 3.18: Ghost Images taken using a cross pattern to perform alignment adjustments

Algorithm 2.

The result is a two-dimensional measurement of the intensity of the system as a function of x_1 and x_2. This can be done for both vertical and horizontal partitions. Where both partitions are displayed on the same relative location for both signal and idler beams, each party of the entangled pair will be detected and coincidence will be counted. When the partitions are mismatched, the photons that DMD1 directs toward the detector are not paired with the photons that DMD2 sends toward the detector, and no coincidence will be detected. As seen in Figure 3.19, the choice of resolution, as well as the over all alignment of the system can effect the extent of the correlation. The total amount of position modes that can be captured by the system is limited. For this reason, we choose an entanglement witness that requires experimentally determined values of only the correlation width, not the extent.

Joint Y Position Scans

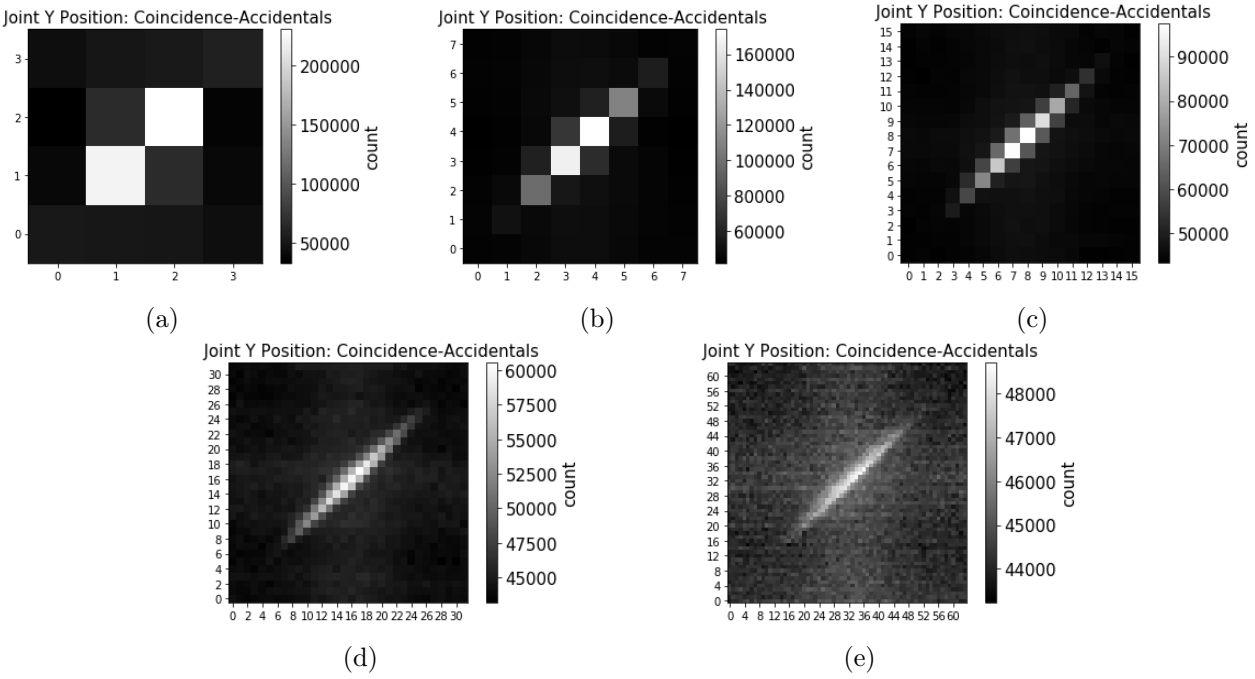

Figure 3.19: Joint Position Scans in the transverse Y direction. Each scan is taken using 45mW pump power and $t_{aq} = 15s$. This data is used first used to align the positions of the DMDs. Once aligned, correlation width can be determined from the data

Algorithm 2 The Joint Raster Scan algorithm.

Declare data as array[R,R]
for x_1' in [0,R] **do**
  for x_2' in [0,R] **do**
    Display partition x_1' on DMD1
    Display partition x_2' on DMD2
    coinc ← Acquire Coincidence from TimeTagger for t_{aq}
    data[x_1',x_2'] ← coinc
  end for
end for

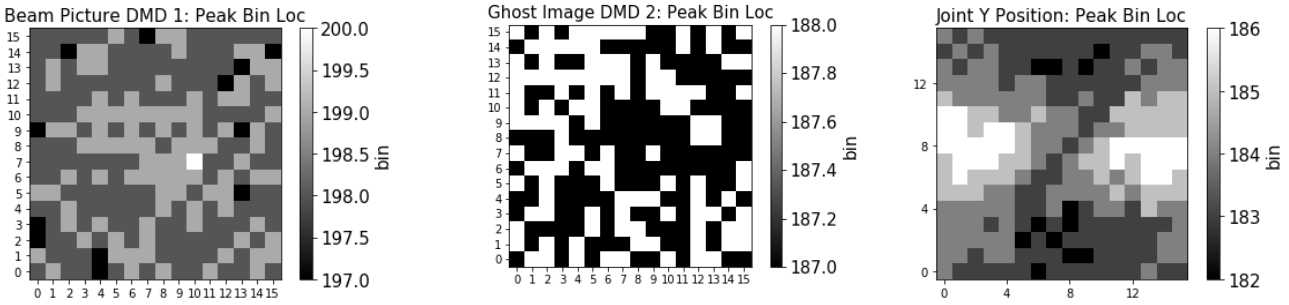

(a) (b) (c)

Figure 3.20: (a) Beam picture peak bin location vs position. (b) The ghost image of a cross pattern peak bin location vs position. (c) Joint Y position peak bin location vs position.

One challenge presented while investigating position measurements is the location of the coincidence peak within the histogram. The amount of light captured by the detectors changes depending on the type of data set taken. For beam pictures, ghost images, and joint position measurements, the incident power on the detectors is different. Within each type of scan, the peak bin varies by 1-2 bins (0.1-0.2ns) but the larger discrepancy between types of scans requires prior average coincidence peak bin identification before scanning data is taken. Given an average bin, a scan can be done with a constant coincidence window centered on that bin. Identifying the peak bin is important because we aim to use a coincidence window size that encompasses the peak without capturing the surrounding noise. Some peak bin data has structure, like Figure 3.20 (c). For a joint position scan, there appears to be structure in the peak bin data as the DMDs vary the projected position mode. This is likely a result of variable coupling efficiency associated with each partition on the DMDs.

Chapter 4

Holographic Projections Using DMDs

4.1 Calculating Holograms Analytically

4.1.1 Background

Traditionally, in order to investigate the momentum spectrum of the SPDC state, the measurements are taken in the Fourier plane of the NLC. Schneeloch and Howland use two separate optical paths, where one path measures in an image plane of the crystal and the other measures in the Fourier plane of the crystal [33]. The choice of basis is made using polarizers and a polarizing beam splitter that function as a switch between types of measurements. Howell et al. achieve spatial resolution by varying the position of thin slits preceding bucket detectors and the choice of basis is made by replacing the imaging system with a Fourier transforming system by changing the lenses used [34].

Moreau et al. [35] and Edgar et al. [36] both show spatial correlations using electron-multiplying charge coupled devices (EMCCD) cameras, in separate near and far field configurations. Ndagnao et al. perform a similar experiment using single photon avalanche diode (SPAD) cameras. Defienne et al. compare EMCCD and CCD cameras in correlation measurements [37]. Lastly, Achatz et al. scan transverse position using optical fibers on translation stages in the image plane and Fourier plane by adding or removing a lens preceding the fiber tips [38]. All of these examples have one thing in common, there is a physical configuration

change that needs to be made by the operator to change basis.

The goal of the technique used in this experiment is to avoid a change in configuration. Configuration changes can be cumbersome and do not extend to arbitrary mode projection. The advantage of holograms is that no change is needed to the configuration and the location of the DMD with respect to the incoming beam is constant. The disadvantages arise from the theory of holograms as well as the effects of the mirror array itself.

Because holograms can encode interference, holograms provide a potential scheme to project an incident state onto momentum modes without having to change the optical configuration. The process known as matched filtering [39] will allow for a selection of momentum modes, just as raster scanning from Section 3.1.6 allows for a selection of position modes. Holograms can be realized by devices that can impose a spatial mask on the incident light, such as film with variable transmittance, etching on a solid surface, or an array of mirrors [39]. The DMD provides a surface that can impose a spatial mask onto the reflected light. The DMD is fit to display holograms because it has very high reflectivity, high-resolution control, and can display any hologram that is chosen to be displayed. The mirrors themselves are small enough to encode interference fringes which is required to display a hologram with high precision. We are able to employ a programmable diffraction grating using DMDs that allows us to project different momentum modes. Unlike traditional holography where a new film would need to be created for each use case, we computationally calculate all holograms needed and display them on a DMD.

4.1.2 Defining Holograms

A hologram is the encoding of the interference pattern of a reference field and an object field. In traditional holography, a scene is illuminated with a coherent reference field. An intensity sensitive film records the interference pattern of the illumination light with the light transmitted or reflected off the object present. This is referred to as the recording problem [39]. Later, that film can be reilluminated and the output will have a component that replicates the original object field.

Imaging vs Fourier Transforming Configurations

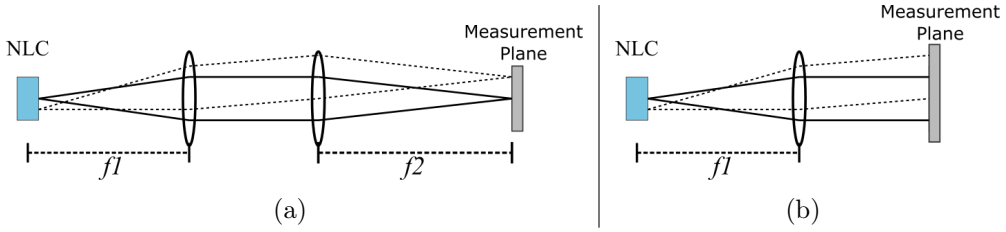

Figure 4.1: (a) The configuration for imaging the crystal. A measurement device like a camera or DMD can be placed in the image plane and directly measure the position of photons. (a) is the configuration chosen for this experiment. (b) The configuration for directly measuring the momentum distribution of photons from the crystal. A Fourier plane measurement can be accomplished by using holograms in the image plane instead of changing the experimental configuration.

In this chapter, we will explore the general descriptions of holograms and how they can be used for momentum mode projections. Holography uses amplitude-controlled devices such as special types of holographic film or mirror arrays. There are benefits of using holography over spatial light modulators that control phase directly. Spatial light modulators can be very expensive, while DMDs are inexpensive and widely available, providing potential scalability. There are also drawbacks to using holographic projections, some inherent to the theory of holograms, as well as practical considerations.

In general, a hologram is a recording of the intensity of the interference pattern of a reference field interacting with an object field. The SPDC state is not in general a single wavelength state, but as we did in Chapter 2 we consider only the degenerate case. Examples will be done with coherent illumination.

A hologram is typically written as:

$$H(x,y) = |A(x,y) + a(x,y)|^2 \tag{4.1.1}$$

Where $A = |A(x,y)| \exp(i\phi(x,y))$ is the reference field, and $a = |a(x,y)| \exp(i\psi(x,y))$ is the object field. A hologram encode phase information when expanded:

$$H(x,y) = (A+a)(A+a)^* = |A|^2 + |a|^2 + aA^* + a^*A \rightarrow$$
$$|A|^2 + |a|^2 + |a||A|\exp(-i\phi)\exp(i\psi) + |a||A|\exp(i\phi)\exp(-i\psi) \rightarrow$$
$$|A|^2 + |a|^2 + 2|a||A|\cos(\phi - \psi) \quad (4.1.2)$$

Where the first line in Eq. 4.1.2 is the form we will invoke the most often. Note regardless of the illumination field, the hologram itself will yield three components. A component with a uniform phase front, $|A|^2 + |a|^2$, which Goodman refers to as a "uniform component". The two other components aA^* and a^*A whose phase fronts vary in space and encode the phase profile of the input fields are referred to as "field components" [39]. We will only need to employ object and reference fields that have uniform constant amplitude, which we normalize such that $|A(x)|^2 + |a(x)|^2 = 2$. The "recording problem" can be confined to computational simulations of the interference pattern.

It is important to note some properties of the plane wave. For a plane wave, the wave vector points in the direction of propagation, $|\vec{k}| = \frac{2\pi}{\lambda}$, and with transverse component$|\vec{k_T}| = |\vec{k}|\sin\theta$, where the transverse plane is perpendicular to the primary optical axis $\hat{z}$. We will again be operating in the paraxial regime where the longitudinal component of the wave vector is much greater than the transverse components, $k_z \gg k_x, k_y$. In the paraxial regime we can make the small angle approximation: $|\vec{k}|\sin\theta \approx |\vec{k}|\theta$. A plane wave $p(\vec{x})$ propagating in an arbitrary direction is defined as:

$$p(\vec{x}) = e^{i\vec{k}\cdot\vec{x}} \quad (4.1.3)$$

Consider a plane wave with a single transverse $\hat{x}$ component which is evaluated at a plane perpendicular to the chosen propagation axis defined by $z = z_0$ and written as:

$$p^x = e^{i(k_x = k_T)x} \cancelto{1}{e^{i(k_y=0)y}} \cancelto{\text{constant phase}}{e^{i(k_z=k_L)z_0}} \rightarrow e^{ik_x x} \quad (4.1.4)$$

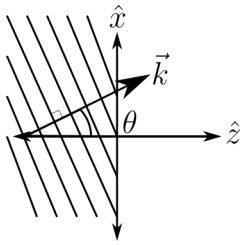

Figure 4.2: Plane wave in arbitrary direction $\vec{k}$ shown in the xz plane with transverse component angle θ

To perform a momentum mode projection, we consider the reference field A as a plane wave. When writing a hologram, we are representing the interference pattern of a reference field and an object field we are interested in. There are two equivalent ways to write a hologram that encodes the angle between these two fields in the interference pattern. The first is where the reference field itself can be written as a plane wave with a non-zero transverse component. The second is where the given object field can be multiplied by a plane wave component:

$$|e^{ikx} + a(x)|^2 = |1 + e^{-ikx}a(x)|^2 \tag{4.1.5}$$

Given Eq. 4.1.5, all the positional dependence can be encompassed by the object field and the reference field can be written as $A(x) = 1$. To understand the relationship between the 3 hologram components, we will first describe the output field for the simplest object case and build a framework to make momentum mode projections.

The hologram we will consider first is that of a plane wave object field:

$$H_1(x) = |1 + e^{ik_0 x}|^2 = 2 + e^{ik_o x} + e^{-ik_o x} \tag{4.1.6}$$

Where $k_o = \vec{k_o} \cdot \hat{x}$ is the object field component.

4.1.3 Illumination of a Hologram

The illumination of a hologram in position representation is simply the multiplication of the illumination field with the transmission mask of the hologram. The hologram acts as a spatial mask that allows light to either transmit or absorb (reflect toward or away) depending

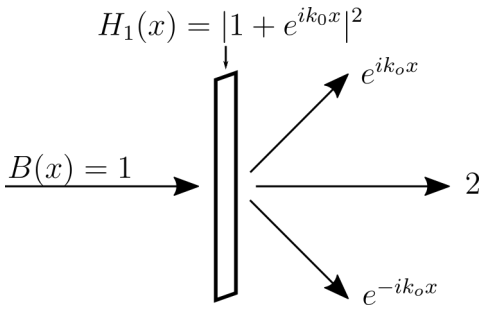

Figure 4.3: Hologram output components of H_1 illuminated by $B(x) = 1$. The vectors represent the direction of propagation for each output plane wave.

on position [39]. We call the general illumination field $B(x)$. To observe the effects of the hologram, illumination by the plane wave $B(x) = 1$ is useful. The output field is:

$$B \times H_1 = 1 \times H_1 = 2 + e^{ik_o x} + e^{-ik_o x} \tag{4.1.7}$$

Shown in Figure 4.3 all three output hologram components are a plane wave, the uniform component is parallel to the primary optical axis, and the field components are comprised of an exact replication of the object field and its conjugate.

To observe the output dependence on the illumination field, let $B = e^{ik_i x}$. Let the angle of incidence for the illuminating plane wave be encompassed by k_i. This interaction is represented by the field interaction:

$$e^{ik_i x} H_1 = e^{ik_i x}(2 + e^{ik_o x} + e^{-ik_o x}) = 2e^{ik_i x} + e^{i(k_i + k_o)x} + e^{i(k_i - k_o)x} \tag{4.1.8}$$

An important property of this interaction is that the change in the angle of incidence for a collimated illumination beam shifts the propagation direction of all three hologram components by a constant amount in k space. Changing k_i shifts all the hologram components in the same direction, while the shift due to changing k_o shifts the two field components away or toward the uniform component, without changing the uniform component angle. In the paraxial regime shift in k_i corresponds to all three components shifted by a constant angle. Although the incident state in this experiment is comprised of multiple transverse momentum modes, the center illumination angle is fixed parallel to the primary optical axis.

4.1.4 Matched Filtering

By programming the value of the object field plane wave propagation direction, k_o, we can use holograms to investigate an unknown illumination field. Projections onto plane wave fields allow for the decomposition of the illumination state into plane waves traveling in various directions. Measuring the amount of light that passes through the projections is an investigation into the transverse momentum spectrum that makes up the input state. The concept of matched filtering will be used to separate out the modes as an investigative technique to determine the composition of the incident field.

Matched filtering is the use of a lens and an aperture to separate output modes from the output of an illuminated hologram. As described in Goodman [39], the placement of a thin lens centered on the primary optical axis along with an aperture at the focal point allows for the selection of output modes that are plane waves with no transverse momentum components. This is because a field whose propagation direction is parallel to the $\hat{z}$ axis will be focused to a bright point at a distance f from the lens along the $\hat{z}$ axis. At that point, an aperture can be placed such that only the component of the field incident on the lens that is "flat" will pass. Contributions to the output field of the hologram that have non-zero transverse components will be focused by the lens, but due to the shift in momentum space, the point of focus will appear with a non-zero transverse coordinate. These modes will not pass through the aperture. Therefore varying the angle of the plane wave encoded in the object field using a choice of k_o allows us to control the mode that passes through the aperture and is collected. In this experiment, the lens is realized by the objective lens, and the tip of the fiber that collects the light acts as the aperture.

The detection condition for matched filtering is the presence of a component that has no transverse momentum. In the ideal case, no light will be detected unless k_o "matches" a mode that is present in the illumination field B, hence matched filtering. For example, when $k_o = k_i$ in Eq. 4.1.8, the second term is a wavefront that is uniform and perpendicular to the $\hat{z}$ axis and will be detected. k_o is the parameter we control during an experiment, each value of k_o corresponds to a transverse momentum mode partition. We display the

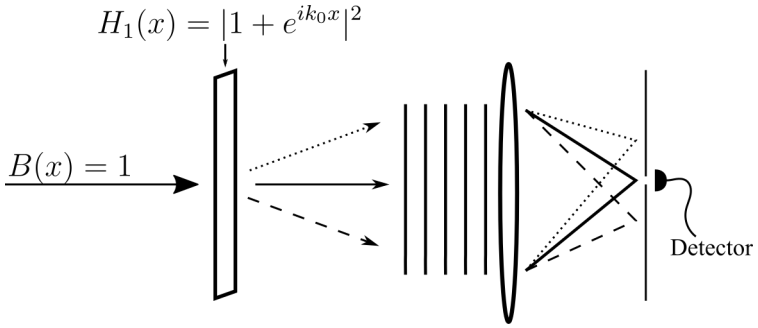

Figure 4.4: Matched filtering configuration for Eq. 4.1.7.

image that represents the hologram on the DMDs with various values of k_o. We measure the amount of light that passes through the aperture for each k_o using the same detector and fiber coupling configuration as we did for the position measurements. A projection onto a momentum mode by displaying various holograms corresponding to values of k_o is analogous to displaying position partitions corresponding to various values of x' in Section 3.1.6. For the interaction in Eq. 4.1.8, given an ideal matched filtering apparatus, detection occurs when $k_o = \pm k_i$.

Algorithm 3 The Joint Momentum Hologram Scan algorithm.

Given Parameters: λ, θ_{ymax}, R
List holos ← Calculate list of holograms from corresponding to $-\theta_{ymax}$ to θ_{ymax} in R steps
Declare data as array[R,R]
for i in [0,R] **do**
  for j in [0,R] **do**
    Display holo[i] for θ_1' on DMD1
    Display holo[j] for θ_2' on DMD2
    coinc ← Acquire Coincidence from TimeTagger for t_{aq}
    data[i,j] ← coinc
  end for
end for

4.1.5 Indistinguishability Problem

A major consideration when using one-dimensional holograms to make momentum mode projections is the indistinguishability of the output components. Given Eq. 4.1.8 represents illumination by a single plane wave component, scanning over k_o would yield detection from

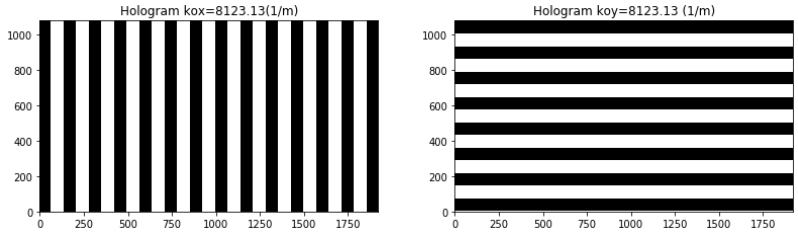

(a) (b)

Figure 4.5: (a) Binary hologram displayed on the DMD to project momentum mode corresponding to the single transverse momentum mode $k_o = 8123.12m^{-1}$ in the $\hat{x}$ direction. (b) Similar hologram for $k_o = 8123.12m^{-1}$ in the $\hat{y}$ direction. Simulation and "binarization" are described in Section 4.2.4.

Subset of Holograms used for Y Momentum Scan

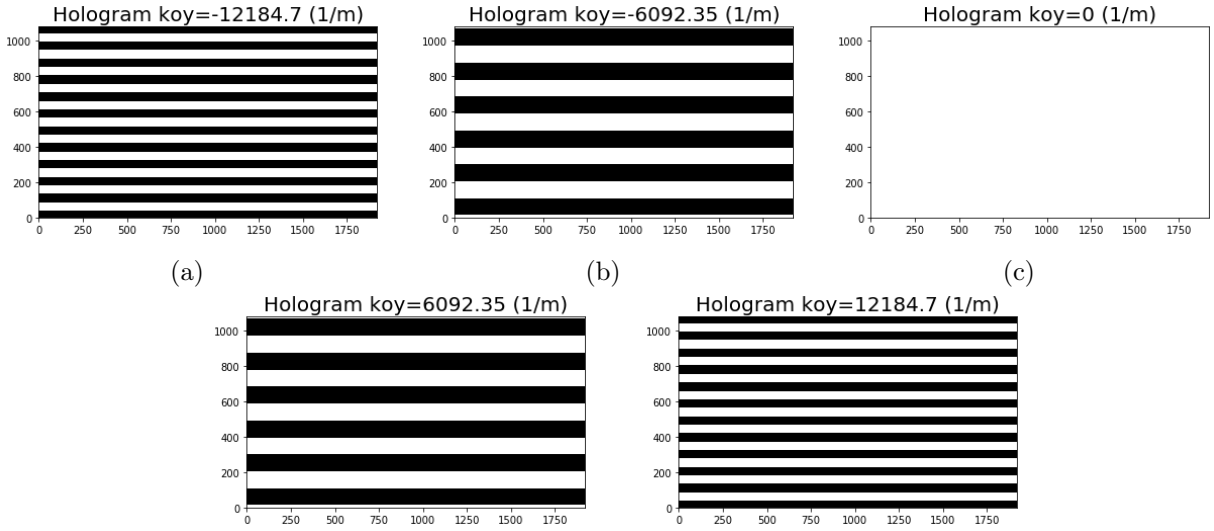

(a) (b) (c)

(d) (e)

Figure 4.6: Subset of Holograms used in a joint scan over Y momentum. k_{oy} is the transverse wave vector value for the object field programmed. (c) Is the hologram for zero transverse momentum, so there is no interference pattern encoded in the hologram. All light is either reflected toward or away from the detector. It is important to note that the holograms for k_o and $-k_o$ are the same.

matched filtering at both $k_o = k_i$ and $k_o = -k_i$. Without knowledge of the illumination state, the sign of momentum modes present would not be obtainable. This creates a challenge for observing the anticorrelations for the momentum spectrum of an EPR-like state. Indistinguishability can be confirmed by observing the holograms themselves, as in Figure 4.5, the fringe spacing is related to the *relative* difference of angle between the reference and object field propagation directions, calculation of holograms corresponding to k_o and $-k_o$ yield the exact same holograms.

The goal of this section is to model the field interaction for two holograms H_1 acting on the signal and idler biphoton system, simulate the detection procedure and compare the model to experimental results. The indistinguishability problem can be modeled explicitly by calculating the field interaction with the holograms for the biphoton state and modeling matched filtering as a small range of accepted modes in momentum space. With insight into the explicit field interaction, we propose a solution to the indistinguishability problem.

Let the illumination field be the double Gaussian approximation to the SPDC state Eq. 2.3.23. Here we are concerned with the biphoton field, where x_1 and x_2 are independent such that operators that act on them commute.

$$B(x_1, x_2) \propto \exp\left(-\frac{(x_1 - x_2)^2}{8\sigma_{x_-}^2}\right) \exp\left(-\frac{(x_1 + x_2)^2}{8\sigma_{x_+}^2}\right) \tag{4.1.9}$$

The illumination of the holograms with field B is the interaction of the SPDC state with the spatial mask the holograms impose. The field just after the hologram interaction is written in terms of the hologram H_1 from Eq. 4.1.6 parameterized by the object wave vectors in position space as:

$$B(x_1, x_2)H_1(x_1 : k_{o1})H_1(x_2 : k_{o2}) \propto \Psi(x_1, x_2)|1 + e^{ik_{o1}x_1}|^2|1 + e^{ik_{o2}x_2}|^2 \tag{4.1.10}$$

The interaction between the SPDC state and the holograms is simpler in momentum space, the Fourier transform of H_1 from position space to momentum space is:

$$\mathcal{F}\left[H_1(x:k_o)\right] = \mathcal{F}\left[|1+e^{ik_o x}|^2\right] \propto 2\delta\left(k\right) + \delta\left(k+k_o\right) + \delta\left(k-k_o\right) \tag{4.1.11}$$

The Fourier transform of the output state is:

$$B(k_1,k_2) * H_1(k_1:k_{o1}) * H_1(k_2:k_{o2}) \propto$$
$$\Phi(k_1,k_2) * \left[2\delta\left(k_1\right) + \delta\left(k_1+k_{o1}\right) + \delta\left(k_1-k_{o1}\right)\right]\left[2\delta\left(k_2\right) + \delta\left(k_2+k_{o2}\right) + \delta\left(k_2-k_{o2}\right)\right] \tag{4.1.12}$$

Where $*$ is the convolution operation, and the convolution of operators of independent variables is multiplication. Convolution of a function with a Dirac delta applies a shift in the distribution. The resulting output state Φ' is comprised of 9 double Gaussians terms in transverse momentum space and is written as:

$$\Phi'(k_1,k_2:k_{o1},k_{o2}) \propto 4\Phi(k_1,k_2) +$$
$$2\Phi(k_1+k_{o1},k_2) + 2\Phi(k_1-k_{o1},k_2) + 2\Phi(k_1,k_2+k_{o2}) + 2\Phi(k_1,k_2-k_{o2}) +$$
$$\boxed{\Phi(k_1+k_{o1},k_2+k_{o2}) + \Phi(k_1-k_{o1},k_2-k_{o2})} + \underline{\Phi(k_1-k_{o1},k_2+k_{o2}) + \Phi(k_1+k_{o1},k_2-k_{o2})} \tag{4.1.13}$$

Recall we control the output state by varying k_{o1} and k_{o2}, the parameters that determine the angle of the plane wave object fields for each hologram. The first term in the output state Φ' does not depend on our choice of k_{o1} and k_{o2}, we refer to this as the uncontrolled term. The next four terms only depend on k_{o1} or k_{o2}, but not both, we refer to these terms as marginally controlled terms. The last four terms depend on both k_{o1} and k_{o2} and are referred to as fully controlled field terms. Figure 4.7 is a visualization of the state. Note that the constant term is centered in k space, and is not shifted by hologram control. All three types of contributions to the output state are needed to model detection. Each term in the output state corresponds to one of the three hologram output fields discussed in Section 4.1.3. Indistinguishability arises since we are detecting the desired output field as well as its conjugate.

Simulation of Φ'

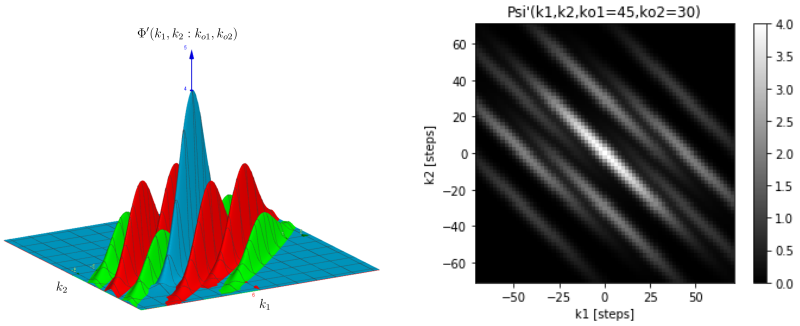

(a) (b)

Figure 4.7: (a) 3D rendering of Φ', amplitudes to scale. Blue Gaussian is the constant term, red Gaussians are the marginal terms, and green Gaussians are the fully controlled terms. (b) 2D simulation of Φ', amplitudes to scale. In both cases, the scale of k_1 and k_2 reflects the scale of raw data collection, and convenient choices of k_{o1} and k_{o2} are made to demonstrate the separation between the terms.

In order to model the detection of the output state, we can sum the output state over a small range of k_1 and k_2 values centered on zero. This is represented by the aperture that precedes the detector in Figure 4.4. This can be done because the fiber coupling configuration is originally coupled to provide the most intense coincidence measurement when all mirrors are oriented toward the fibers. It is assumed the fibers are coupled into the center of the outgoing beams for the calculation of the ideal detection scheme. In reality, there is imperfect coupling in terms of the direction of the beam, distortion for the diffraction of the mirror array, and alignment of the objective lens. Assume the detection window in k space that represents the acceptance of modes onto the fiber tip has width W_k. Accepted modes then are modes propagating away from the DMDs with transverse wave vectors $\frac{-W_k}{2} \leq k \leq \frac{W_k}{2}$. The probability of detection parameterized by k_{o1} and k_{o2} is the probability of the output state occupying the modes in the detection window:

$$P(k_{o1}, k_{o2}) = \int_{\frac{-W_k}{2}}^{\frac{W_k}{2}} \int_{\frac{-W_k}{2}}^{\frac{W_k}{2}} dk_1 dk_2 \left|\Phi'(k_1, k_2 : k_{o1}, k_{o2})\right|^2 \tag{4.1.14}$$

We visualize the simulation output corresponding to H_1 in two ways. First, the state itself in terms of k_1 and k_2, as in Figure 4.7 (b). Next, the probability of detecting coincidence in

Comparing Simulated Detection to Experiment

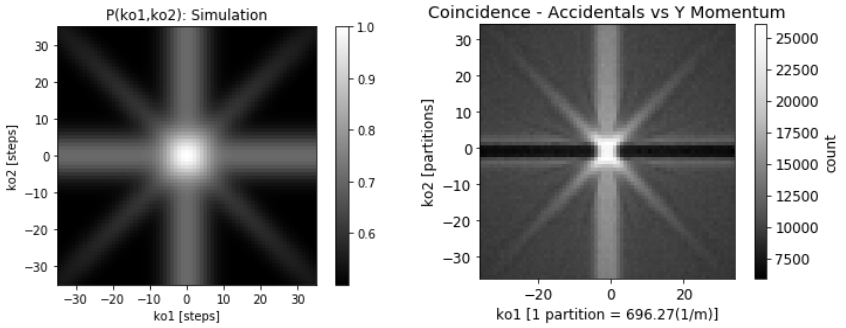

(a) (b)

Figure 4.8: (a) Simulation of Eq. 4.1.14. Each integral is estimated by a sum of 50 terms. (b) Coincidence data collected displaying H_1 on each DMD. Both plots as functions of k_{o1}, k_{o2} in step sizes of $696.27m^{-1}$. The corresponding range of k_o values is $\left(-24369m^{-1} \leq k_{o1}, k_{o2} \leq 24369m^{-1}\right)$

terms of the hologram control variables k_{o1} and k_{o2} as in Figure 4.8. Eq. 4.1.14 is numerically evaluated, normalized, and plotted against values of k_{o1}, k_{o2}, shown in Figure 4.8 (a).

Simulation and data collection both support the presence of the indistinguishability problem. When matching on k_{o1} and k_{o2}, the boxed terms in Eq. 4.1.13 contribute to the appropriate detection of the modes present in the illumination state. The output term $\Phi(k_1 - k_{o1}, k_2 - k_{o2})$ for example is all that is needed to use matched filtering to determine the joint transverse momentum of photon pairs. The underlined terms have a sign mismatch between the signal and idler projections and equally contribute to the detection for the given values of k_{o1}, k_{o2}. Therefore, when making momentum mode projections using H_1, the sign of the illumination mode can not be determined, so the tight correlations in $k_1 + k_2$ manifest as "correlations" and "anticorrelations". The presents of both correlations and anticorrelations as well as other detection patterns seen in the experimental results are confirmed by the simulation. There is a high noise present in the experimental data which is the result of the uncontrolled term present in the output state. This uncontrolled term does not vary with any control parameters. The uncontrolled output term is analogous to the uniform term in equation 4.1.7. Marginal control terms in the output state include a control parameter for only one of the two photons, therefore the resulting detection data appears to have vertical and

horizontal stripe patterns. These patterns are found in both the simulation and the experimental results. The horizontal stripe in the experimental results differs from the prediction of the simulation in that the experimental data is disrupted by a drop in the coincidence, which is likely due to detector saturation. The correlation/anticorrelation patterns are from the fully controlled terms in the output state. The model in Figure 4.8 (a) accurately describes the artifacts seen when momentum mode projections are made using H_1.

Recall the goal is to measure the correlation width as in Figure 2.4. The artifacts present in this form provide a challenge to fit the measurement results with a double Gaussian and obtain a correlation width. Contributions from the marginal terms are unavoidable using H_1. Details of all experimental artifacts that deviate from the simulation are explored further in Section 4.2.

4.1.6 Solution to the Indistinguishability Problem

The indistinguishability arises because there are fully controlled terms for each combination of $\pm k_{o1}$ and $\pm k_{o2}$ that can not be isolated through matched filtering detection. We propose the addition of a Constant Plane Wave Offset (CPWO) to the object field in the complementary transverse direction to eliminate the symmetry. Consider the second hologram used in this experiment:

$$H_2(x) = |1 + e^{ik_C y} e^{ik_0 x}|^2 = 2 + e^{ik_C y} e^{ik_0 x} + e^{-ik_C y} e^{-ik_0 x} \tag{4.1.15}$$

where the term $p^y = e^{ik_C y}$ is the CPWO, a fixed shift in transverse momentum on the $\hat{y}$ direction of the object field.

We again explicitly calculate the output field of the SPDC state after it interacts with the two DMDs displaying H_2. To simulate detection, we write the double Gaussian approximation to the SPDC state in terms of both transverse $\hat{x}$ and $\hat{y}$ variables:

Subset of Holograms used for Y Momentum Scan with CPWO of 0.0275^o

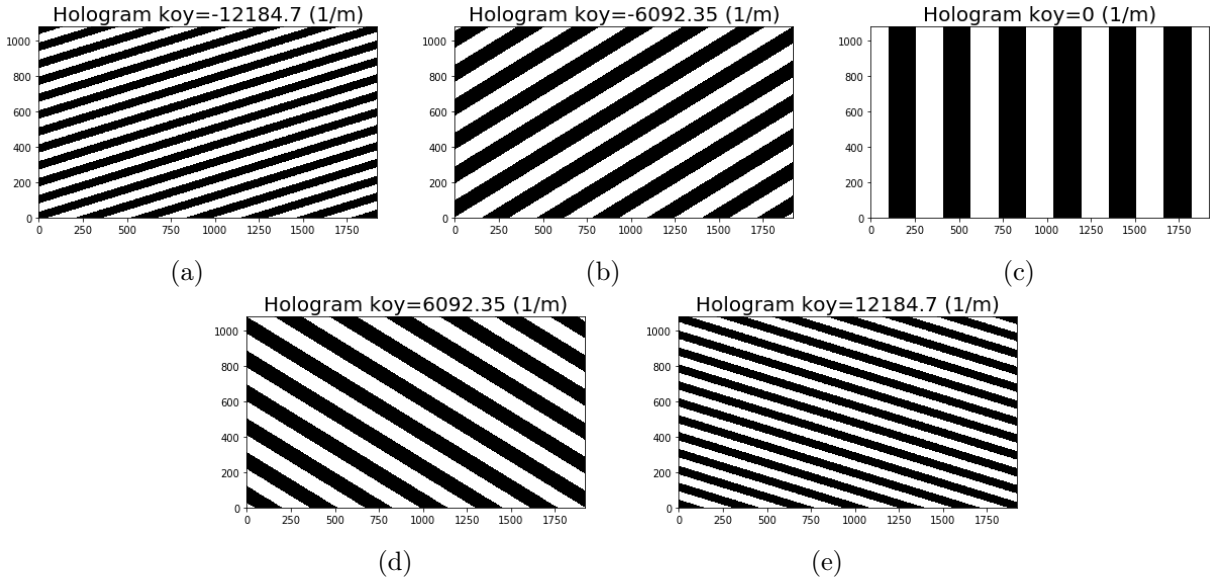

Figure 4.9: Two important features to note about the set of holograms that include the CPWO. 1) Holograms for k_o and $-k_o$ are not the same, which supports the CPWO as a solution to the indistinguishability problem. 2) the center mode $k_o = 0$ is not uniform but includes the Hologram component of the CPWO. This subset of holograms represents a variable transverse Y component, and a CPWO in X, so the number of fringes in the horizontal direction is constant, while the number of fringes in the vertical direction varies.

$$B \to \Psi(\vec{r_1}, \vec{r_2}) = \Psi_x(x_1, x_2)\Psi_y(y_1, y_2) \propto$$
$$\exp\left(-\frac{(x_1 - x_2)^2}{8\sigma_{x_-}^2}\right) \exp\left(-\frac{(x_1 + x_2)^2}{8\sigma_{x_+}^2}\right) \exp\left(-\frac{(y_1 - y_2)^2}{8\sigma_{y_-}^2}\right) \exp\left(-\frac{(y_1 + y_2)^2}{8\sigma_{y_+}^2}\right) \quad (4.1.16)$$

The output state is then

$$\Psi_x(x_1, x_2)\Psi_y(y_1, y_2)H_2(x_1, y_1 : k_{o1}, k_C)H_2(x_2, y_2 : k_{o2}, k_C) =$$
$$\Psi_x(x_1, x_2)\Psi_y(y_1, y_2)|1 + e^{ik_C y_1}e^{ik_{01}x_1}|^2|1 + e^{ik_C y_2}e^{ik_{o2}x_2}|^2 \quad (4.1.17)$$

Expanding the H_2 terms and Fourier transforming the system yields the output state Φ' in momentum space:

$$\begin{aligned}
\Phi'(k_{x1}, k_{x2}, k_{y1}, k_{y2}) = \Phi_x(k_{x1}, k_{x2})\Phi_y(k_{y1}, k_{y2}) * \Big[& 4\delta(k_{x1})\delta(k_{x2})\delta(k_{y1})\delta(k_{y2}) + \\
& 2\delta(k_{x1})\delta(k_{y1})\left[\delta(k_{x2} - k_{o2})\delta(k_{y2} - k_C) + \delta(k_{x2} + k_{o2})\delta(k_{y2} + k_C)\right] + \\
& 2\delta(k_{x2})\delta(k_{y2})\left[\delta(k_{x1} - k_{o1})\delta(k_{y1} - k_C) + \delta(k_{x1} + k_{o1})\delta(k_{y1} + k_C)\right] + \\
& \boxed{\delta(k_{x1} - k_{o1})\delta(k_{x2} - k_{o2})\delta(k_{y1} - k_C)\delta(k_{y2} - k_C)} + \\
& \boxed{\delta(k_{x1} + k_{o1})\delta(k_{x2} + k_{o2})\delta(k_{y1} + k_C)\delta(k_{y2} + k_C)} + \\
& \underline{\delta(k_{x1} - k_{o1})\delta(k_{x2} + k_{o2})\delta(k_{y1} - k_C)\delta(k_{y2} + k_C)} + \\
& \underline{\delta(k_{x1} + k_{o1})\delta(k_{x2} - k_{o2})\delta(k_{y1} + k_C)\delta(k_{y2} - k_C)}\Big]
\end{aligned} \quad (4.1.18)$$

Again, considering the experiment will scan over the value of k_{o1} and k_{o2}, there are three different types of contributions: uncontrolled terms, marginally controlled terms, and fully controlled terms. The difference between the state in Eq. 4.1.18 and Eq. 4.1.13 is that the former state contains terms whose distribution in terms of k_y are shifted by $\pm k_C$. In Eq.

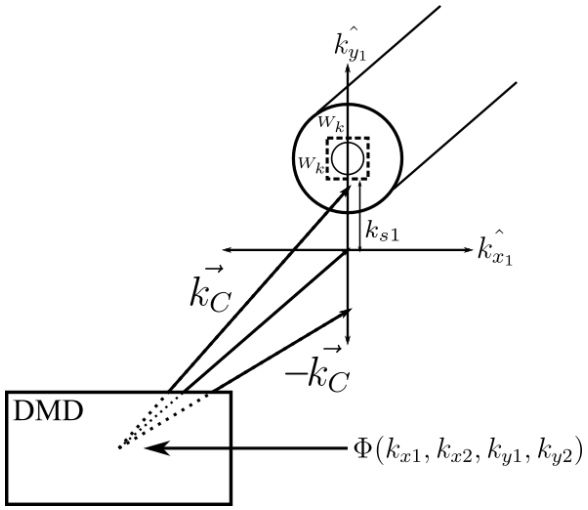

Figure 4.10: Coupling configuration (omitting the matched filtering lens for simplicity). For H_2, the coupling configuration has a significant effect on the components of the output field that are detected.

4.1.18, the boxed terms are sign matched for the projection of the momentum modes in k_x controlled by k_{o1} and k_{o2}. The boxed terms are also sign matched in their shift in k_y space. The underlined terms are sign mismatched in their controlled k_x distributions and are also sign mismatched in their constant shift in k_y space by the CPWO. The use of H_2 couples together the k_x and k_y components in such a way that the state is not separable. The mechanism that imposes the inseparability is the various shifts of the original distribution in the 4 dimensional biphoton transverse momentum distribution.

From Eq. 4.1.18, we say that using H_2 allows for an investigation of the k_x distribution of the input state on a constant off-center slice in k_y space. The CPWO shifts the direction the output states propagate away from the holograms. Therefore the boxed terms shift signal and idler in the same direction in k_y space, and the underlined terms shift signal and idler in opposite directions in k_y space.

Using H_2, the two-dimensional hologram that includes a CPWO, the coupling configuration can be shifted to accept modes shifted by $\pm k_C$ in k_{y1} and k_{y1}. Let k_{s1} and k_{s2} be shifts in the location in momentum space of the detection window for photons 1 and 2. Similar to Eq. 4.1.14, the probability of detection is the sum of modes accepted by the detection window:

Simulation of Φ' using H_2 to Show Fully Controlled Term Isolation

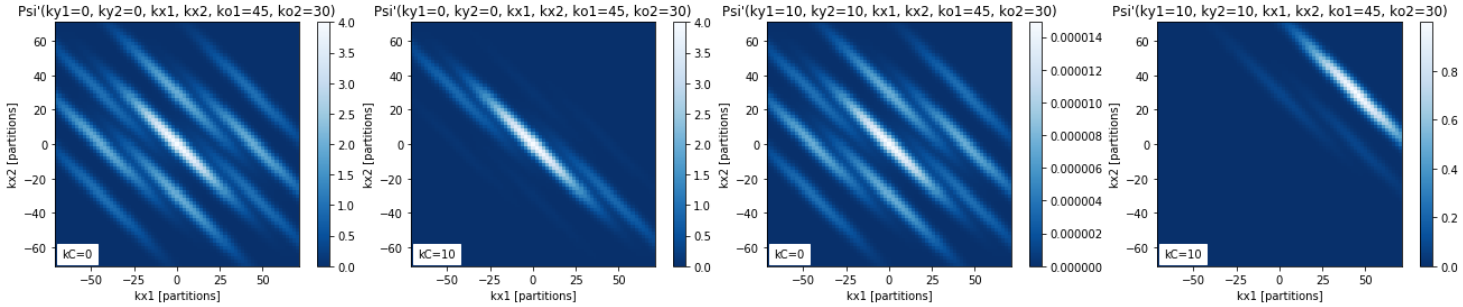

(a) (b) (c) (d)

Figure 4.11: Visual description of the isolation of the matched sign fully controlled term. (a) Φ' evaluated at $k_{y1} = k_{y2} = 0$, convenient choices of k_{o1} and k_{o2} are made to display the separation the holograms impose on the components. With $k_C = 0$ the state is reduced to Eq. 4.1.13. (b) nonzero CPWO narrows the band of components with significant relative amplitude. For the center slice in k_y space, the uncontrolled term is isolated. (c) Φ' without a CPWO, but here the off-center slice in k_y space is evaluated, notice the distribution of components is identical to (a) but the amplitude is greatly reduced. (d) Evaluating Φ' at $k_{y1} = k_{y2} = k_C$ isolates the matched sign fully controlled component. Each component can be identified by omitting the others from the simulation.

$$P(k_{o1}, k_{o2} : k_{s1}, k_{s2}) = \int_{\frac{-W_k}{2}}^{\frac{W_k}{2}} \int_{\frac{-W_k}{2}}^{\frac{W_k}{2}} \int_{\frac{-W_k}{2}+k_{s1}}^{\frac{W_k}{2}+k_{s1}} \int_{\frac{-W_k}{2}+k_{s2}}^{\frac{W_k}{2}+k_{s2}} dk_{x1}, dk_{x2}, dk_{y1}, dk_{y2} \left|\Phi'(k_{x1}, k_{x2}, k_{y1}, k_{y2} : k_{o1}, k_{o2})\right|^2 \tag{4.1.19}$$

Unlike H_1, H_2 includes both the transverse $\hat{x}$ and transverse $\hat{y}$ dimensions and a multitude of control variables imposed by the hologram and experimental configuration. Figure 4.11 describes Φ' itself for various configurations. Evaluating Φ' at a slice in k_y space is directly related to the shift in the detection window in k_y. Hologram H_2 is found to produce the distinguishability needed to identify the sign of the modes being investigated.

To detect the transverse components of momentum, holograms are used to decompose the unknown illumination state into components of transverse momentum. The programmer will display the hologram Eq. 4.1.15. The programmer can then scan through a range of values for the transverse momentum on the $\hat{x}$ direction, corresponding to values of the object plane wave k_{oi} for each DMD. Tracking the intensity of the light that passes through the matched filtering elements as the hologram varies with k_{oi}, the composition of the unknown illumination field can

Simulated Detection for Various Configuration

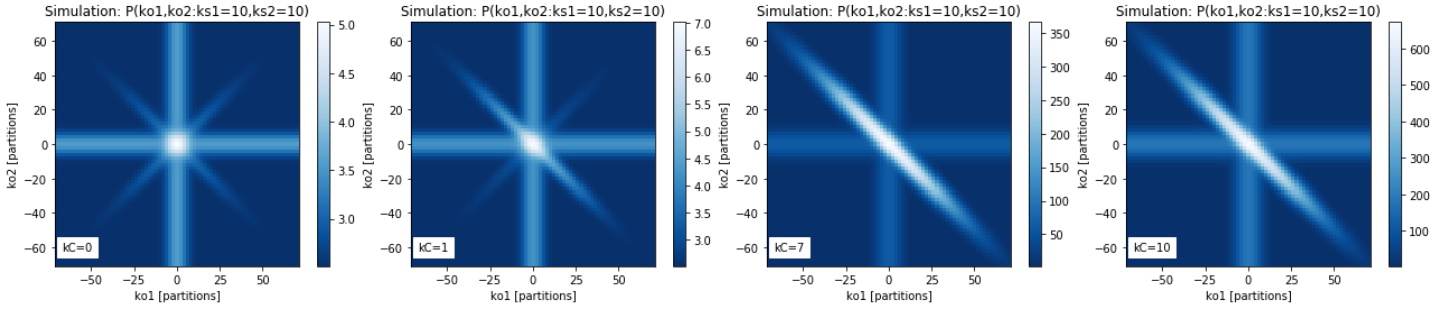

(a) (b) (c) (d)

Figure 4.12: Simulation of detection at various CPWO values for a constant coupling condition. (a) No CPWO which is equivalent to using H_1. When using a shift in the coupling window, this configuration yields lower relative amplitude and includes a significant contribution from the marginal terms and the sign mismatched fully controlled term. (b) Introduction of the CPWO. The contribution from the sign mismatched fully controlled term is less. (c) k_C nears k_{s1} and k_{s2}. The simulation indicates this is the ideal set of configuration parameters since the sign matched fully controlled terms are the most significant. (d) $k_C = k_{s1}, k_{s1}$. The simulation indicates this is the most significant sign-matched contribution but there is a revival of the marginal control contributions. More detailed modeling is needed to investigate the true expected state from detection as we did not see significant contributions from the marginal control terms for larger CPWO use.

be exactly reconstructed from its spectrum in transverse momentum in the $\hat{x}$ direction. This is the method used in this experiment. Many interesting anomalies, artifacts, and limitations arise when using holograms, described in Section 4.2. Artifacts will refer to any property of the data that does not match the predicted SPDC state. From the data, there is a rich array of artifacts that can inform on the intricacies of hologram use for quantum state projections. The primary advantage of a scheme where holograms are displayed in the image plane of the crystal is that other bases can easily be investigated, including OAM modes and LG modes [13].

The simulations provide interesting comparisons to the experimental results. The relative amplitude between different simulations did not match the detected coincidence. The comparison between simulation and acquired data is only used qualitatively. We use the simulations as a confirmation that the contributions to the experimental data reflect the overall model described by equation Eq. 4.1.18. Each type of term predicted by calculating the output

Variable CPWO for Y Momentum Projections

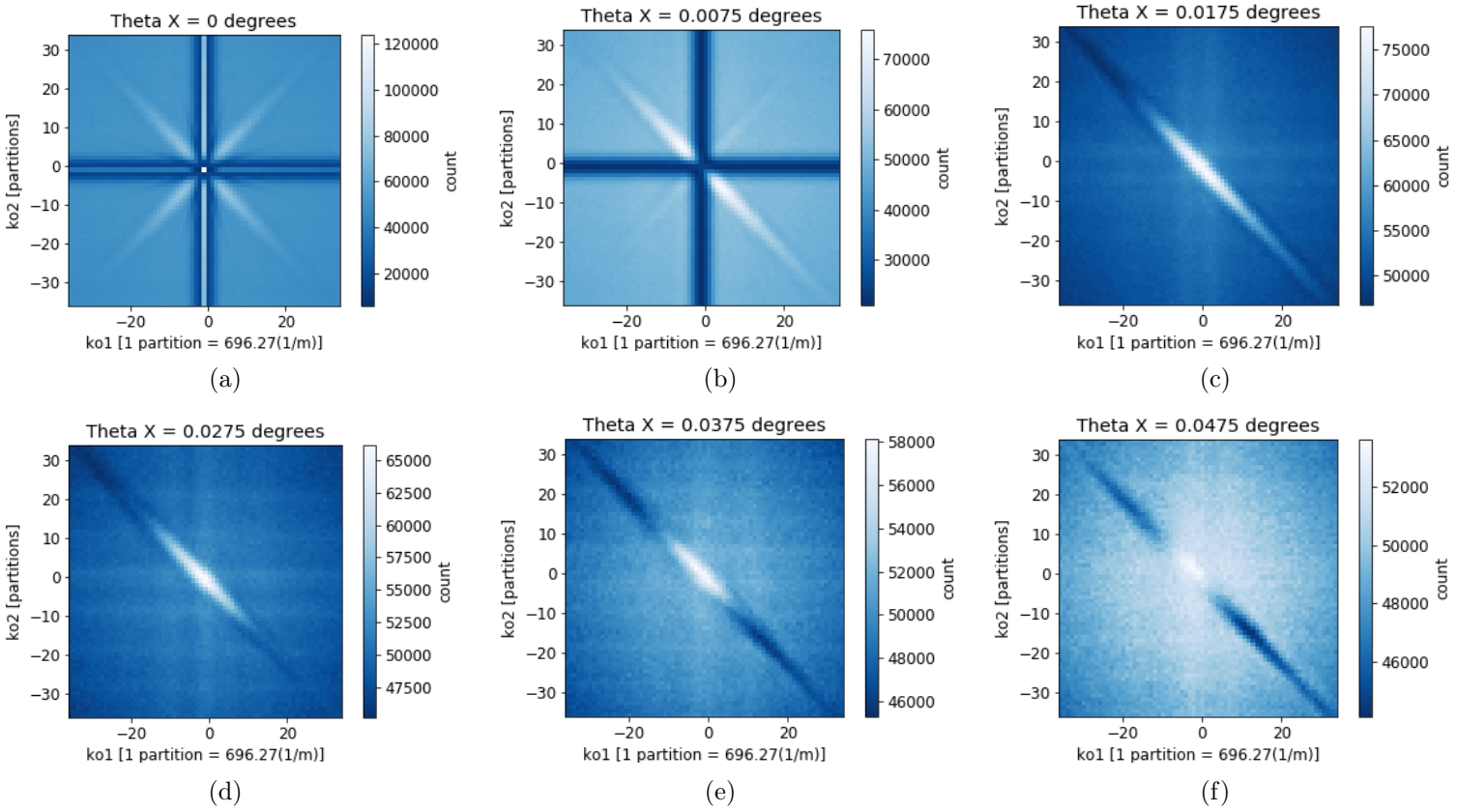

(a) (b) (c)

(d) (e) (f)

Figure 4.13: Experimental results of variable CPWO in the x direction for transverse momentum scans in y directions given a constant experimental coupling configuration. Range of k_o values correspond to $-0.18^o \leq \theta_y \leq 0.18^o$. Each picture represents data acquired with a different CPWO offset with the corresponding angles : (a)$\theta_x = 0^o$. (b)$\theta_x = 0.0075^o$. (c)$\theta_x = 0.0175^o$. (d)$\theta_x = 0.0275^o$. (e)$\theta_x = 0.0375^o$. (f)$\theta_x = 0.0475^o$. Various artifacts arise, some expected from the simulation, like marginal control term contributions. Others like the coincidence dips for larger CPWO used are not predicted by the simulations.

state, uncontrolled, marginally controlled, and fully controlled, is present in the experiment under different conditions.

Horizontal and vertical patterns found in the measured transverse momentum probability distributions arises purely from the prediction of holograms and the theoretical description of the state as it leaves the interaction plane and heads toward the detectors. Indistinguishability and marginal control terms present in the output state contribute to these patterns.

4.2 Practical and Experimental Considerations

In this section, we aim to identify the challenges we encountered when making joint momentum mode projections using holograms displayed on DMDs. The following sections describe issues not predicted by the calculated state 4.1.18 and detection probability 4.1.19 that also impact correlation width measurements.

4.2.1 Inaccessible Modes

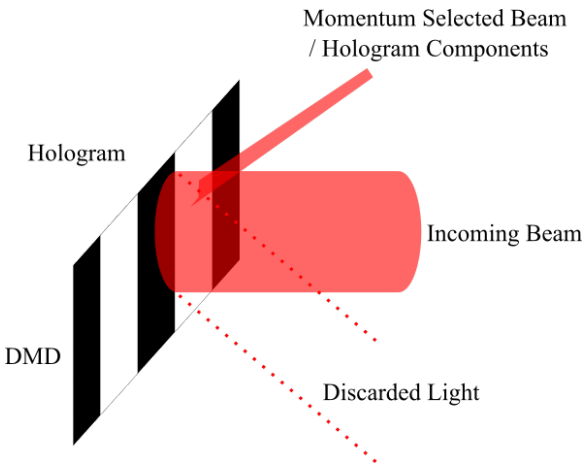

Figure 4.14: Model for hologram interaction for inaccessible modes. Shown here is the binary hologram that represents a momentum shift of 0.01^o. Note how the beam is only incident upon one fringe. The effective number of fringes is not enough for diffractive effects to be detectable.

For holograms corresponding to relatively small shifts in transverse momentum, the fringes are large and farther apart. When the incoming beam interacts with the DMD, the beam is

incident on a small number of fringes. The result is a detection that does not accurately correspond to the momentum mode programmed on the hologram. With a finite beam size, non-realizable modes are an unavoidable issue. The extreme case consists of a range of holograms that reflect the beam either entirely toward or away from the detector. In this case, the transverse momentum shifts programmed in the hologram contain fringes whose width is larger than the incident beam width. The beam is incident upon a uniform region of mirrors and the outgoing beam does not experience any interference effects.

Inaccessible modes and some other anomalies can be investigated by looking at the singles rates, the overall rate of photons incident on the detectors regardless of coincidence. When there is a drop in the detected singles rate, a corresponding drop in coincidence is not necessarily related to whether that particular mode is present in the quantum state or not. It may simply be the inaccessibility of that mode due to the fringe width of the hologram, reflecting all the photons away from the detector. Further investigation can be done to learn about the transition between the inaccessible modes and the modes that experience strong interference effects. Particularly the relationship between the beam width and the fringe width could be identified to determine the minimum number of fringes needed to effectively project a momentum mode.

4.2.2 Incomplete Extinction

As described in Figure 3.10(e) and Figure 3.11(d) there is not complete extinction between the fully ON and fully OFF states for the DMDs. The orientation of the mirrors on the 4700 DMDs is unique in that the combination of the diffractive properties of the mirror array and the mirror orientations themselves create an asymmetric extinction relationship between the ON and OFF modes. Because of the orientation of the modes in the plane parallel to the table, beam C in Figure 3.6, was easily accessible given the mounting configuration, the mode with a lower extinction ratio was used in the experiment. Future iterations of this experimental setup would require the mounts to be rotated 90^o around the z axis such that the currently discarded mode is the new detected mode and the roles of the ON and OFF pixels swapped.

Negating the CPWO and Comparison to Transverse X Momentum

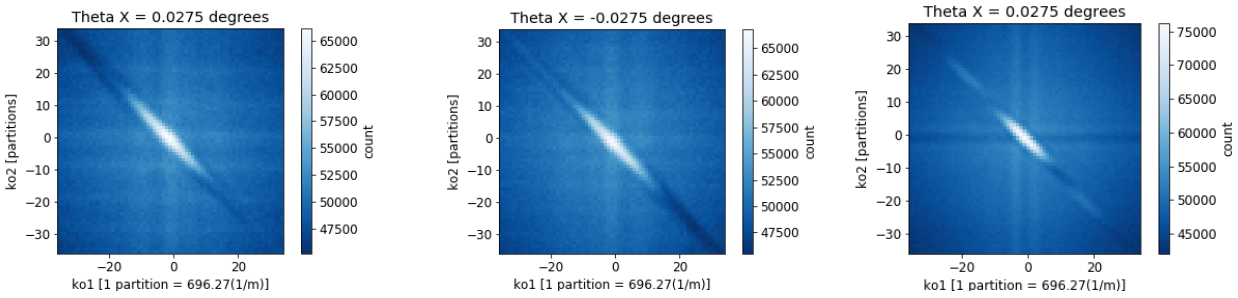

(a) (b) (c)

Figure 4.15: Results of Negation of the CPWO angle and the complementary measurement configuration. (a)(b) show opposite CPWO values used where the dark band is reflected over the origin. (c) is the same data set taken with the roles of x and y swapped. This is included as a reference for the results of a scan over the transverse momenta k_x for the SPDC state. From this, we can see that the positional in x is not as aligned with the coupling mechanism as it is in y. The k_x mode correlation lacked significant extent, which may be related to the presents of the dark bands in the k_y scans.

A higher extinction ratio would allow for a lower noise floor when investigating correlation for both position and momentum.

4.2.3 Unexplained Dark Band in Coincidence for Joint Correlations

Figure 4.15, as well as Figure 4.13, display one of the most interesting findings of this experiment. For most configurations used, the anticorrelations are present, a double Gaussian shape can be identified in the joint coincidence data. The use of H_2 imposes a dip in the coincidence rate along the length of the double Gaussian. There appears to be only a small window of CPWO values that yield a valid double Gaussian profile. Smaller CPWO values allow for marginal control term artifacts and larger CPWO values introduce the coincidence dip. It is unclear what contribution from Φ' or experimental condition causes the dip in coincidence. It is possible that the contribution to coincidence from the fully controlled terms behaves uniformly across the extent of the correlations but the uncontrolled and marginal terms vanish there, leading to lower overall coincidence at the location of the dip. It is also possible the overall particular experimental conditions are not able to detect coincidence for those particular modes for some unknown reason.

Hologram Inversion

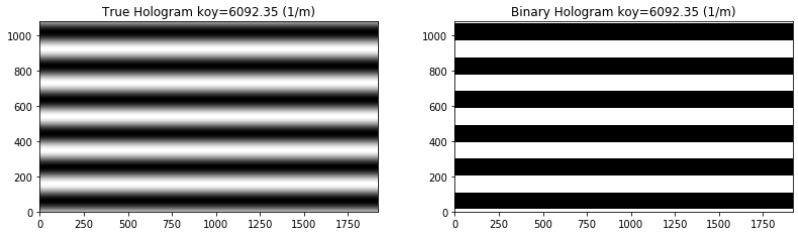

(a) (b)

Figure 4.16: (a) Hologram directly calculated from the interference pattern of the object and reference field. (b) The Binary hologram for the same interference.

Figure 4.15 (a) and (b) show two data sets corresponding to a particular CPWO and the relation to the offset. The coincidence dip reflects over the origin relative to the correlation extent. Future iterations of this experiment may be able to identify the cause of the coincidence dip and take advantage of a predictable dark band shape to reinforce a correlation width measurement.

4.2.4 Binarization and Resolution

Algorithm 4 Binary Hologram Generation algorithm.

field $\leftarrow A(x, y) + a(x, y)$
I $\leftarrow$ field $\times$ Conjugate(field)
I $\leftarrow$ I-Min(I)
I $\leftarrow$ I / |(Max(I)|
Output round(I)

The hologram is calculated as a continuous range of amplitude transmittance. The DMD is a binary-controlled device so the hologram amplitude values are normalized and rounded. The result is a binary hologram.

Although the binarization itself does not cause detection issues, the utilization of holograms with high-frequency fringes may be limited by device parameters. If the fringe spacing is calculated to be less than the pixel size, the hologram is not realizable given the display device. There may also be some pattern revivals dues to the aliasing effect and Moiré patterns of high-frequency modes.

Hologram Inversion

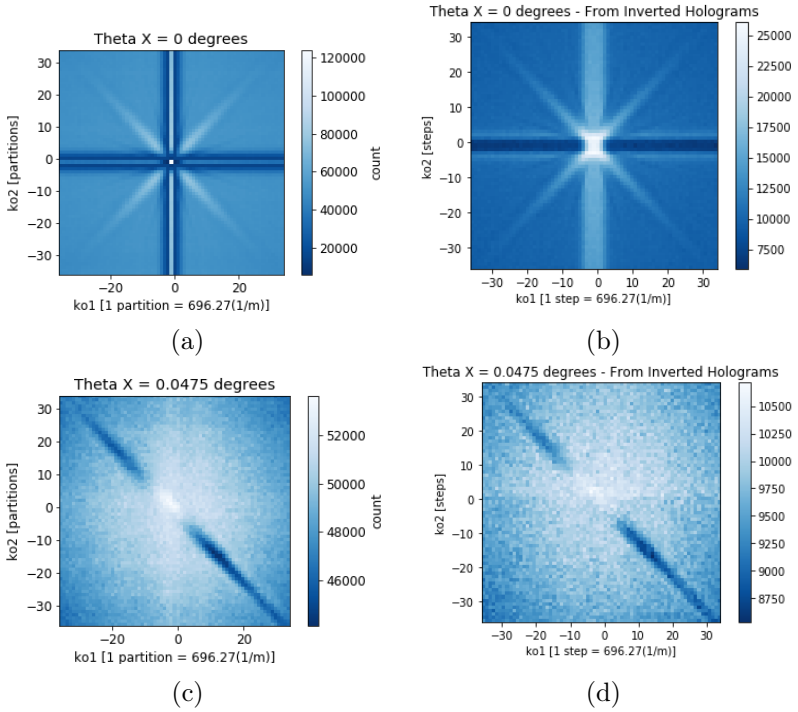

Figure 4.17: Inversion of binary Holograms: (a)(b) H_1 used. There are vertical and horizontal patterns that arise along with the expected marginal control term contributions. The discrepancy between the high coincidence vertical pattern and the low coincidence horizontal pattern can be attributed to a shift in the coincidence peak outside of the coincidence window used. Inversion of the hologram has a significant effect on modes near $k_o = 0$. (c)(d) H_2 used. Here there is no difference in the artifacts between the hologram and its inverse. The CPWO used shifts all the modes projected away from $k_o = 0$ so there are significant diffractive effects for every step used in the scan.

4.2.5 Hologram Inversion

Given that the Hologram is binary when displayed, the inverse (ON and OFF mirrors swap roles) of the holograms can also be displayed. The result is a hologram that carries the same information. From experiments using holograms and their inverses, we find that configurations that result in one dimension vertical and horizontal patterns are most significantly affected by the inversion of the hologram. These patterns can be a result of the presents of marginal control terms in the output state as well as the inaccessibility of modes near the center of the distribution. Hologram inversion changes the state (ON or OFF) of the center fringe which is the primary interaction for inaccessible modes. Figure 4.17 (a) is an example of the effects

of using the hologram inverse, which changes the nature of the artifacts. While Figure 4.17 (b) shows for larger CPWO the use of the inverse holograms is inconsequential because the hologram used includes a significant number of fringes and therefore significant diffractive effects. It is clear that hologram inversion affects the modes relatively close to the center momentum mode. For larger CPWO values, inaccessible modes are not present so hologram inversion has less effect. Overall inverting the hologram does not change the information we can obtain about the joint momentum correlations but does affect the artifacts that arise in the detection scheme.

4.2.6 Summary of Hologram Investigation

Among the interesting artifacts found when using H_2 to investigate momentum distributions of the SPDC state, the vertical and horizontal patterns seen have multiple potential sources. The theory predicts some vertical and horizontal patterns representing an increase in detection (coincidence) as a narrow band of k_o values centered at zero, as seen in Figure 4.12 from the presents of the marginal control terms in the output state. The source of this artifact is further complicated by the same configuring being used with inverted holograms and the presents of inaccessible modes. Inversions of the hologram also change the center ($k_o = 0$) mode behavior. Inverting a hologram should not change the information that it encodes, but center modes do not simply interact as holograms but are affected largely by whether the center fringe in the pattern is "ON" or "OFF".

Overall the hologram H_2 from Eq. 4.1.15 allows for the projection of transverse momentum modes and the corresponding joint space coincidence measurements that yield a correlation width predicted by the SPDC state. Configurations are identified that yield clear double Gaussians and correlation widths that can be measured.

Chapter 5

Results Estimating Entanglement

In this chapter, we will develop quantitative predictions for entanglement witnesses to compare with experimental results. We must consider the discrete nature of the detection scheme as well as the shape of the probability distribution we are measuring. We will investigate the discrete detection of an EPR state, the ideal detection of the SPDC state, and the combined consideration of the discrete detection and the double Gaussian approximation of the SPDC state. From Section 2.4, we employ the entanglement witness written in the form $\sigma_{x_-}\sigma_{k_+} \geq \frac{1}{4}$. We interpret experimental data, determine the correlation width, compute an entanglement witness, and compare it with our predictions.

5.1 Entanglement Witness Predictions

5.1.1 Discrete Detection of the Ideal EPR State

First, we must investigate the limitations of using a discrete detection scheme to collect joint spatial probability distributions for the ideal EPR source and calculate an entanglement witness. We assume perfect detection of joint correlations and the detection amplitude is uniform across all joint correlated modes. The ideal EPR state measured using discrete partitions in joint position and joint momentum space would yield a measured joint position probability distribution as in Figure 5.1.

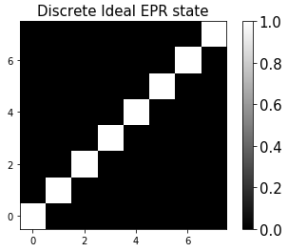

Figure 5.1: Probability distribution for a discrete measurement of the ideal EPR state. Calculation of an entanglement witness for this probability distribution is useful because it informs on the relationship between the entanglement violation and the resolution of the spatial detection.

Determining the relationship between the resolution used in the detection and the entanglement witness is important because the experimental quality of the results is affected by the choice of resolution. This is particularly important when using position partitions, where the resolution directly affects both the amount of light captured and the minimum correlation width that can be resolved. Low-resolution scans obtain higher coincidence counts but can not resolve a small enough correlation width to observe entanglement. High resolutions suffer from lower coincidence per partition but can resolve the detected state. The physical dimensions of the position partitions as programmed on the DMD can be calculated:

$$W_x = a \cdot N_m = \frac{a \cdot N_T}{R_x} \tag{5.1.1}$$

$$W_{x\pm} = \sqrt{2} W_x \tag{5.1.2}$$

where W_x is the width of a position partition, $W_{x\pm}$ is the diagonal width of a joint partition pixel, $a = 5.4\mu m$ is the size of a single mirror [31], $N_T = 1024$ is the total height and width of the active area used on the DMDs in number of mirrors, and N_M is the number of mirrors per partition. R_x is the resolution, the number of partitions we choose to use in a joint position scan, defined as the ratio of the partition size to the total length of the active area used on the DMD. Half the total diagonal width of a joint partition W_{x-} is an estimate for the correlation width σ_{x-} of the joint position probability distribution.

To calculate an estimate for the entanglement witness we also need the limit for the joint momentum correlation width. For the joint momentum probability distribution, each hologram corresponds to a particular transverse momentum mode. We traverse the joint momentum space using a fixed angular step size. The angular step size between each hologram defines the width of the partition for that joint momentum scan. The physical dimensions of the momentum partitions using angular step sizes of W_θ can be calculated:

$$W_\theta = \frac{2\theta_{max}}{R_\theta} \tag{5.1.3}$$

$$W_k \approx |k| W_\theta = \frac{2\pi}{\lambda} W_\theta \tag{5.1.4}$$

$$W_{k\pm} = \sqrt{2} W_k \tag{5.1.5}$$

where W_k is the width of a momentum partition in terms of wave vectors, $W_{k\pm}$ is the diagonal width of a joint momentum partition pixel and λ is the wavelength of the down-converted photons. The effective resolution of a discrete momentum scan using holograms can be calculated by dividing the total angular window width of momentum modes accessed in the scan by the step size. Half the total diagonal width of a joint partition W_{k+} is an estimate for the correlation width σ_{k_+} of the joint momentum probability distribution.

Given an ideal EPR state is detected using discrete spatial partitions, the minimum correlation widths that could be measured are limited by the resolution chosen. This is the maximum amount of entanglement we can certify using the chosen resolutions. To calculate this limit, we can use the diagonal width of the joint partition as an estimate for the correlation width. Therefore the estimate of the violation of the inequality is:

$$\sigma_{x_-}\sigma_{k_+} \approx \frac{W_{x-}}{2}\frac{W_{k+}}{2} = \frac{\sqrt{2}aN_T}{2R_x}\frac{\sqrt{2}\ 2\pi 2\theta_{max}}{2\lambda R_\theta} \tag{5.1.6}$$

An example of a configuration used in this experiment uses the values $\theta_{max} = 0.18^o$, $R_x = 32$, $R_\theta = 71$, which is an angular step size of $W_\theta = 8.85 \times 10^{-5}$radians. The resulting

product of the widths is:

$$\sigma_{x_-}\sigma_{k_+} \approx \frac{W_{x-}}{2}\frac{W_{k+}}{2} = (1.222 \times 10^{-4}m)(485.402m^{-1}) = 0.059 < \frac{1}{4} \tag{5.1.7}$$

The result Eq. 5.1.7 confirms that reasonable choices of resolution for discrete measurements of joint spatial probability distributions yield a valid witness of entanglement.

5.1.2 Theoretical Prediction of an Entanglement Witness

The next useful value of the entanglement witness to compare experimental results to is from the SPDC state directly. We determine the correlation widths as predicted by the double Gaussian approximation of the SPDC state. The correlations are described by the physical parameters discussed in Section 2.3. From Eq. 1.0.5 we find $\sigma_{k_-} = \sqrt{\frac{3\pi}{L_z\lambda_p}} = 62277.68m^{-1}$ for the 3mm BiBo crystal used. For the position correlation width, the physical parameter involved is the radius of the pump beam. The beam diameter at $\frac{1}{e^2}$ power is reported as 1.4mm [26]. From the definition of the $\frac{1}{e^2}$ width, σ_p is found to be $2.9 \times 10^{-4}m$. Invoking Eq. 2.3.19 yields:

$$\sigma_{x_-}\sigma_{k_+} = (8.02851 \times 10^{-6}m)(1213.32m^{-1}) = 0.0097 < \frac{1}{4} \tag{5.1.8}$$

Eq. 5.1.8 describes the minimum values of correlation width that the process of SPDC can produce. In other words, Eq. 5.1.8 is the case for a measurement of the SPDC state with infinite resolution. This is confirmation that a precise measurement of the SPDC state is in fact an observance of entanglement. Note that σ_{k_+} in the resolution limited case Eq. 5.1.7 is less than that predicted by the physical parameters of the SPDC state. By choosing to use high resolution, we can over-resolve the joint momentum probability distribution. This does not necessarily mean that high resolution is unnecessary, a high-resolution scan of the joint momentum space reveals the finer structure of the joint state and does not affect the correlation width.

We also consider both the discrete nature of the detection and the double Gaussian approximation of the SPDC state in a single estimate for the product of correlation widths. We assume that the total diagonal width of a joint partition pixel is the FWHM of a Gaussian model in the rotated coordinate system for the detection of the SPDC state. From the definition of FWHM with respect to standard deviation we write the estimate for the position correlation width:

$$\sigma_{x_-} = \frac{FWHM}{2\sqrt{2\ln 2}} \approx \frac{W_{x_-}}{2\sqrt{2\ln 2}} = \frac{W_x}{2\sqrt{\ln 2}} \tag{5.1.9}$$

Similarly for the estimate of the momentum correlation width:

$$\sigma_{k_+} = \frac{FWHM}{2\sqrt{2\ln 2}} \approx \frac{W_{k_+}}{2\sqrt{2\ln 2}} = \frac{\sqrt{2}W_k}{2\sqrt{2\ln 2}} = \frac{\pi W_\theta}{\lambda\sqrt{\ln 2}} \tag{5.1.10}$$

Using the same experimental parameters as we did in Eq. 5.1.6:

$$\sigma_{x_-}\sigma_{k_+} = (1.04 \times 10^{-4} m)(412.26 m^{-1}) = 0.0428 < \frac{1}{4} \tag{5.1.11}$$

Both Eqs. 5.1.7 and 5.1.11 are important when considering under-sampling (low-resolution scans) which is the case for some joint position measurements. High-resolution measurements have lower coincidence rates and are subject to more noise. Higher resolutions yield much lower coupling efficiency and coincidence therefore there is a practical limit to the resolution. If greater extinction ratios could be achieved, higher-resolution position scans would be feasible. The choice of resolution for momentum mode projections is limited only by the size of the mirrors displaying the holograms. Since transverse momentum step sizes can be chosen smaller than the expected correlation width, under-sampling is not an issue.

5.2 Correlation Width Calculations

Fitting Joint Measurements with Double Gaussian Models

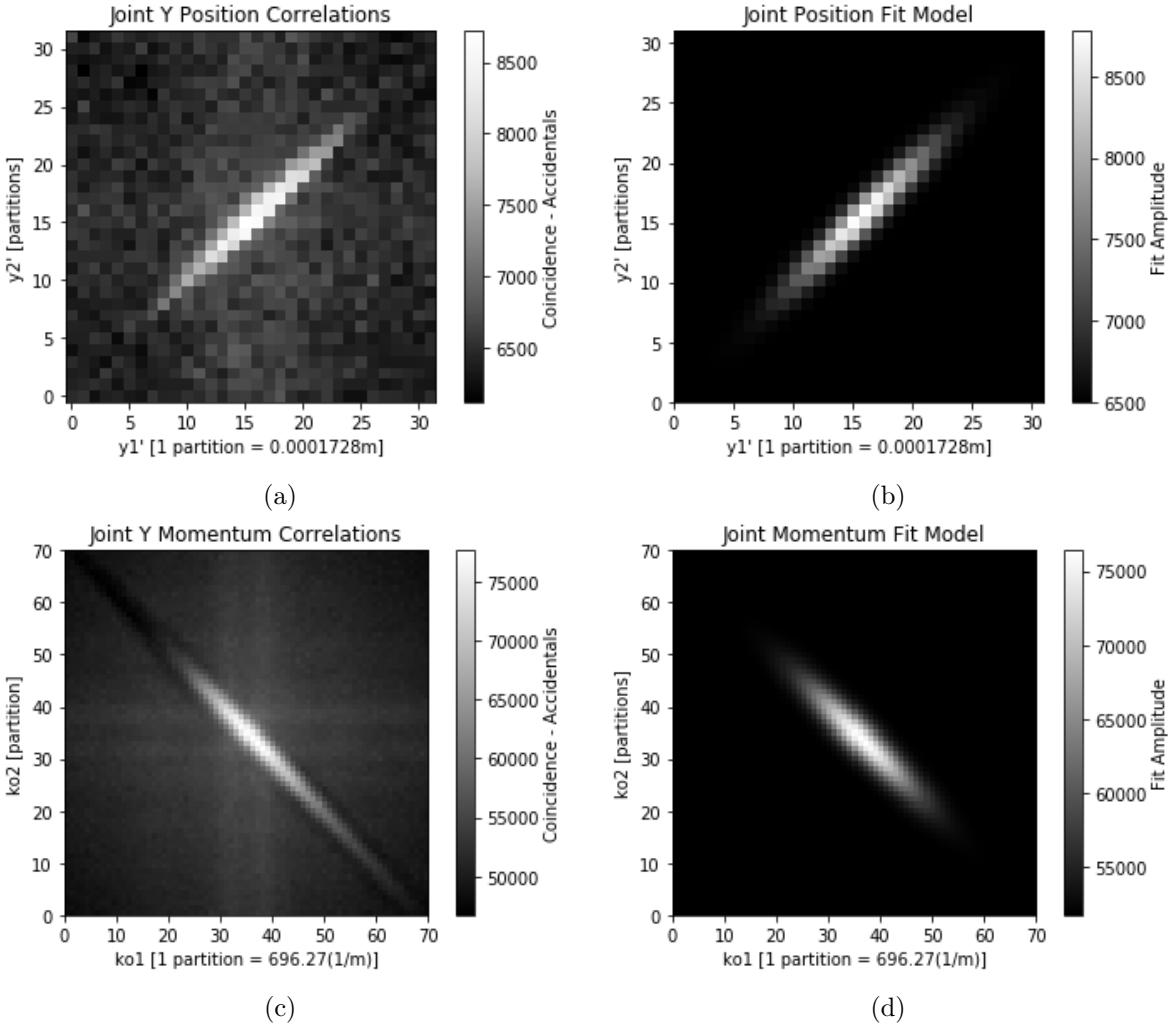

Figure 5.2: Data sets and the fitted double Gaussian approximations. For the position data, $R_x = 32$, $t_{aq} = 2s$, and a coincidence window of $3ns$. For momentum data, $R_\theta = 71$, $t_{aq} = 5s$, CPWO $\theta_x = 0.0175^o$ was used and a coincidence window of $2ns$. Transverse momentum modes corresponding to $[-0.18^o, 0.18^o]$ were scanned. For both 45mW pump power was used.

As discussed in Section 3.1.7 and 4.1.6, measurements of the joint spatial probability distributions are obtained through the projection of position and momentum modes. Data is collected and fit with a double Gaussian model. The joint measurement results are fit using the Python Scipy.optimization.curve_fit function, which includes the uncertainty in the counting statistics from the probability distribution of counts ($\sigma_{coincidence} = \sqrt{coincidence}$) in

the calculation to determine the uncertainty in the resulting fit parameters. The function used a nonlinear least squares fitting method to calculate the fitting parameters. The probability distributions Eq. 2.3.25 and 2.3.25 are fit to the data in the form:

$$P_k(k_1,k_2) = A_k \exp\left(-\frac{(k_1-k_2+b_{k-})^2}{4\sigma_{k-}^2}\right)\exp\left(-\frac{(k_1+k_2+b_{k+})^2}{4\sigma_{k+}^2}\right)+C_k \tag{5.2.12}$$

$$P_x(x_1,x_2) = A_x \exp\left(-\frac{(x_1-x_2+b_{x-})^2}{4\sigma_{x-}^2}\right)\exp\left(-\frac{(x_1+x_2+b_{x+})^2}{4\sigma_{x+}^2}\right)+C_x \tag{5.2.13}$$

Extra fitting parameters b and C are needed to represent the noise floor and coordinate shift, respectively. Among the valid configurations, Figure 5.2 are the data sets that yield the smallest correlation widths.

The fit parameters are first calculated in units of partitions for position and momentum. For both position and momentum, the fit parameters for the standard deviation can be converted from units of partitions to the physical units that they correspond to. The conversions are as follows:

$$\sigma_{x-} = \sigma_{x-}^{data} \times W_x \tag{5.2.14}$$

$$\sigma_{k+} = \sigma_{k+}^{data} \times \frac{2\pi}{\lambda} W_\theta \tag{5.2.15}$$

The minimum correlation widths are found to be $\sigma_{x-} = (1.47 \pm 0.02) \times 10^{-4} m$ and $\sigma_{k+} = (1398 \pm 2) m^{-1}$ whose product is $0.205 \pm 0.003 < \frac{1}{4}$ which satisfies an entanglement witness. The parameters of the particular data sets that yield minimum variance were determined by testing various resolutions, acquisition times, and power levels until a violation was found. The magnitude of the violation strongly depends on how well the system is aligned.

Notice that the value of $\sigma_{x-} = 1.47 \times 10^{-4} m$ calculated from the joint position data is greater than the estimated width from the discrete ideal EPR limit $1.04 \times 10^{-4} m$ as the measured correlation width is greater than 1 partition. The measured value of σ_{x-} is also

Best Fit Parameters for Experimental Joint Measurement Data

Fit Parameter	Position	Momentum
A	2330 ± 30 counts	24670 ± 50 counts
C	6499 ± 3 counts	51752 ± 3 counts
σ_-	$\boxed{(1.47 \pm 0.02) \times 10^{-4} m}$	$(7060 \pm 13) m^{-1}$
σ_+	$(9.6 \pm 0.1) \times 10^{-4} m$	$\boxed{(1398 \pm 2) m^{-1}}$
b_-	$(-4.0 \pm 0.3) \times 10^{-5} m$	$(1910 \pm 20) m^{-1}$
b_+	$(-5.44 \pm 0.02) \times 10^{-3} m$	$(48773 \pm 4) m^{-1}$

Table 5.1: The output of the best-fit algorithm used to determine the double Gaussian model for the chosen data sets.

much greater than the width predicted from the SPDC state directly, $8.03 \times 10^{-6} m$. We can conclude that the experimental condition like the alignment of the system and low extinction ratios that restrict our ability to use high-resolution scans are the most significant experimental restriction to a more significant violation in terms of position and raster scanning.

For momentum, the SPDC state predicts a correlation width of $1213 m^{-1}$, which is within an order of magnitude of our experimentally determined value, unlike the position correlation width. Determining hologram generation parameters like the CPWO used and further analysis of the biphoton state as it leaves the hologram interaction can also inform techniques to improve correlation width measurements. The presents of the asymmetric coincidence dip along the extent of the correlation as in Figure 5.2 restricts the accuracy of the fit.

Comparing Entanglement Witness Prediction to Experimental Results

Estimates	σ_{x_-}	σ_{k_+}	$\sigma_{x_-}\sigma_{k_+}$
Discrete Ideal EPR	$1.22 \times 10^{-4} m$	$485 m^{-1}$	0.059
Discrete Ideal DG Fit	$1.04 \times 10^{-4} m$	$412 m^{-1}$	0.0428
SPDC Parameters	$8.03 \times 10^{-6} m$	$1213 m^{-1}$	0.0097
Experimental Data	$1.47 \times 10^{-4} m$	$1398 m^{-1}$	0.205

Table 5.2: Summary of Entanglement Witness predictions. The experimental measurements of correlation width yield the smallest violation of the entanglement inequality.

5.3 Further Study

This experiment opens the door for a wide range of further exploration into using holograms as a tool to perform mode projections on photon states. This includes investigation into the unexplained correlation dip, matched filtering, and alignment techniques. There is also an interesting possible experiment where the DMDs can be placed in the Fourier plane of the crystal and directly measure transverse momentum modes while holograms can now serve as a projection for position modes.

The goal of this experiment was to certify entanglement in position and linear momentum for an entangled biphoton system. One extension of this project that can be significant for the quantum optics community would be the certification of entanglement using orbital angular momentum (OAM) modes. If holograms can be developed to produce angle and OAM modes, holograms could be shown to be a promising technique to perform arbitrary mode projections. As discussed in Appendix C.1, we can also control beam focus and direction using holograms, which is a promising foundation for producing arbitrary fields, 3D projections, and using DMDs for sensing techniques.

5.4 Conclusion

The goal of this thesis is to observe entanglement in an EPR-like state using the novel technique of holograms for transverse momentum mode projections. We described the criteria needed to observe entanglement and developed a realizable EPR-like state that we can create in the lab. We related this state to the uncertainty principle and entanglement through the properties of the correlations associated with the biphoton state produced by spontaneous parametric down-conversion. We use digital micromirror devices to make selections of position and transverse momentum modes for entangled pairs of photons. Using measurements of joint position and joint momentum probability distributions, we fit these with a double Gaussian model and estimate the correlation widths of the SPDC state. The variance product measured does in fact violate the separability condition and we observe entanglement. Along the way,

we discovered the challenges and open questions involved with using holograms interacting with photon quantum states. We hope this work is informative and provides the quantum optics community with the foundation and inspiration to develop holograms for a wide array of applications and future work.

Apendices

Appendices

Appendix A

SPDC State Derivation

This section is a summary of the derivation of the SPDC state wavefunction by Schneeloch et al. [24]. This is important because it gives the wavefunction physical context in terms of the laser, the crystal, conservation of momentum, and SPDC. From the phase matching constraints, the wave function $\Phi(\vec{k_1}, \vec{k_2})$ that appears in Eq. 2.3.14 is :

$$\Phi(\vec{k_1}, \vec{k_2}) = N\text{sinc}\left(\frac{\Delta K_z L_z}{2}\right)\nu\left(\vec{k_1} + \vec{k_2}\right) \tag{1.0.1}$$

where $\vec{k_p} = \vec{k_1} + \vec{k_2}$ is the collinear condition for transverse momentum coordinates, ν is the pump beam amplitude distribution and $\Delta k_z = k_{1z} + k_{2z} - k_{pz}$. The sinc dependence comes from the Fourier transform of the rectangular profile of the crystal. Assume the pump beam profile is Gaussian $\nu(\vec{q_p}) = A_p \exp(-\sigma_p^2 |\vec{q_p}|^2)$, where σ_p is the pump radius in position space, defined as the standard deviation of $\frac{x_1+x_2}{2}$. Substituting the phase matching conditions Eq. 2.2.13 into Eq. 1.0.1, the state can be written:

$$\Phi(\vec{k_1}, \vec{k_2}) = N\text{sinc}\left(\frac{\lambda_p L_z}{8\pi}|\vec{k_1} - \vec{k_2}|^2\right)\exp\left(-\sigma_p^2 |\vec{k_p}|^2\right) \tag{1.0.2}$$

where the amplitude prefactor is taken such that the probability distribution is normalized. Correlation width is a propriety of the SPDC state which provides a measure of the conditional uncertainty and provides an entanglement witness. We aim to write $\Phi(\vec{k_1}, \vec{k_2})$ in a form that

can be easily related to measurements of correlation width in the joint position and joint momentum space.

A useful approximation to the joint momentum wavefunction Eq. 1.0.2 is to approximate the sinc with a Gaussian. When writing the wavefunction using a Double Gaussian approximation to the SPDC state, the wavefunction is separable in transverse directions $\hat{x}$ and $\hat{y}$, so the analysis may proceed considering only one spatial dimension. A Double Gaussian approximation to Eq. 1.0.2 provides an approximation for the SPDC state in both position and momentum space that can quantify the correlation width of the entangled photons. The wavefunction in momentum space from Eq. 1.0.2 is not separable in k_1 and k_2 therefore the Fourier transform in terms of position coordinates x_1 and x_2 is not clear. This is why we employ the rotated coordinate system Eqs. 2.3.15 and 2.3.16. A Double Gaussian approximation in terms of the entangled coordinates allows us to take the Fourier transform and determine the joint position wavefunction.

In general, a Gaussian can approximate a sinc^2 in the paraxial regime, where the argument is small. A double Gaussian takes the form:

$$DG(x_1, x_2) = A \exp\left(-\frac{(x_1 - x_2)^2}{2\Delta_-^2}\right) \exp\left(-\frac{(x_1 + x_2)^2}{2\Delta_+^2}\right) \tag{1.0.3}$$

where the widths Δ_+ and Δ_- can be related to physical quantities. $\Phi(k_1, k_2)$, the joint transverse momentum space representation of the SPDC state, can be approximated by the form of Eq. 1.0.3 by taking the following steps. Substitution of the rotated coordinates Eq. 2.3.15 into Eq. 1.0.2 yields the wavefunction:

$$\Phi(k_+, k_-) = N\text{sinc}\left(\frac{\lambda_p L_z}{4\pi} k_-^2\right) \exp\left(-2\sigma_p^2 k_+^2\right) \tag{1.0.4}$$

The k_+ dependence is already in a Gaussian form. In order to write the state in terms of a Double Gaussian we need to approximate the k_- dependence term. By integrating over k_+ and squaring, the marginal probability distribution for k_- can be written as:

$$P(k_-) = \frac{3}{4}\sqrt{\frac{a}{\pi}}\text{sinc}^2\left(ak_-^2\right) \approx N' \exp\left(-\frac{k_-^2}{2\sigma_{k_-}^2}\right) \tag{1.0.5}$$

where $a = \frac{L_z\lambda_p}{4\pi}$. Eq. 1.0.5 can be approximated by a Gaussian with variance $\sigma_{k_-}^2 = \frac{3}{4a} = \frac{3\pi}{L_z\lambda_p}$. The transverse momentum wavefunction can now be written in terms of a double Gaussian distribution as a function of k_+ and k_-:

$$\Phi(k_+, k_-) = \sqrt{N' \exp\left(-\frac{k_-^2}{2\sigma_{k_-}^2}\right)\exp\left(-4\sigma_p^2 k_+^2\right)} = N_k \exp\left(-\frac{k_-^2}{4\sigma_{k_-}^2}\right)\exp\left(-2\sigma_p^2 k_+^2\right) \tag{1.0.6}$$

In this form, the position wavefunction can be determined by performing an inverse Fourier transform on the state above. As k_1 and k_2 form an orthonormal Fourier pair with x_1 and x_2, the Fourier conjugates of the rotated coordinates $k_\pm$ are $x_\pm$.

$$\begin{aligned}\mathcal{F}^{-1}\left[\exp\left(-\frac{k_-^2}{4\sigma_{k_-}^2}\right)\right] &= \frac{1}{\sqrt{2\pi}}\int_\infty^\infty \exp\left(-\frac{k_-^2}{4\sigma_{k_-}^2}\right)e^{ik_-x_-}dk_- \\ &= \sqrt{2}\sigma_{k_-}\exp\left(-\sigma_{k_-}^2 x_-^2\right)\end{aligned} \tag{1.0.7}$$

$$\begin{aligned}\mathcal{F}^{-1}\left[\exp\left(-2\sigma_p^2 k_+^2\right)\right] &= \frac{1}{\sqrt{2\pi}}\int_\infty^\infty \exp\left(-2\sigma_p^2 k_+^2\right)e^{ik_+x_+}dk_+ \\ &= \frac{1}{2\sigma_p}\exp\left(-\frac{x_+^2}{8\sigma_p^2}\right)\end{aligned} \tag{1.0.8}$$

The bi-photon wave function in joint position space can be written up to a normalization constant N_x:

$$\Psi(x_+, x_-) = N_x \exp\left(-\sigma_{k_-}^2 x_-^2\right)\exp\left(-\frac{x_+^2}{8\sigma_p^2}\right) \tag{1.0.9}$$

Given the standard form of a Gaussian is $Ae^{-\frac{(x-x_0)^2}{2\sigma^2}}$, we can make a convenient choice of coefficients in the exponent when writing of the wave functions:

$$\Phi(k_+, k_-) = N_k \exp\left(-\frac{k_-^2}{4\sigma_{k_-}^2}\right) \exp\left(-2\sigma_p^2 k_+^2\right) \rightarrow N_k \exp\left(-\frac{k_-^2}{4\sigma_{k_-}^2}\right) \exp\left(-\frac{k_+^2}{4\sigma_{k_+}^2}\right) \quad (1.0.10)$$

$$\Psi(x_+, x_-) = N_x \exp\left(-\sigma_{k_-}^2 x_-^2\right) \exp\left(-\frac{x_+^2}{8\sigma_p^2}\right) \rightarrow N_x \exp\left(-\frac{x_-^2}{4\sigma_{x_-}^2}\right) \exp\left(-\frac{x_+^2}{4\sigma_{x_+}^2}\right) \quad (1.0.11)$$

where the variance relationships can be found by matching the terms in the above expressions, which yields Eq. 2.3.19 and is reported in Section 2.3.

Appendix B

Addition Results

B.1 Fit Data and Plots

Figure B.1 includes select data sets that yield low correlation widths. A variety of experimental parameters were used to isolate a representative measurement. Some power, time, and resolution combinations were not compatible due to low extinction, high noise, or low overall coincidence counts. It is unclear if there is an ideal configuration for the setup, ideally, the alignment would be perfect and any scan with high enough resolution should yield a proper measurement. The need for high power, small oscillation in pump power, and interference from various hologram artifacts pose a challenge to determining the ideal set. Incomplete extinction could also be investigated further by taking a coincidence measurement for "OFF" states. Since there is a coincidence signal while partitions are in the "OFF" state, this background contribution varies with position across the DMD. Handling incomplete extinction needs special attention to separate the coincidence that is due to the DMD control and the coincidence that is always present per partition.

B.2 Further investigation into correlation coincidence dip

Here we include all the data taken from a joint momentum scan where there is a significant pair of coincidence dips or dark bands in the coincidence data where we expect only a double

Additional Correlation Data

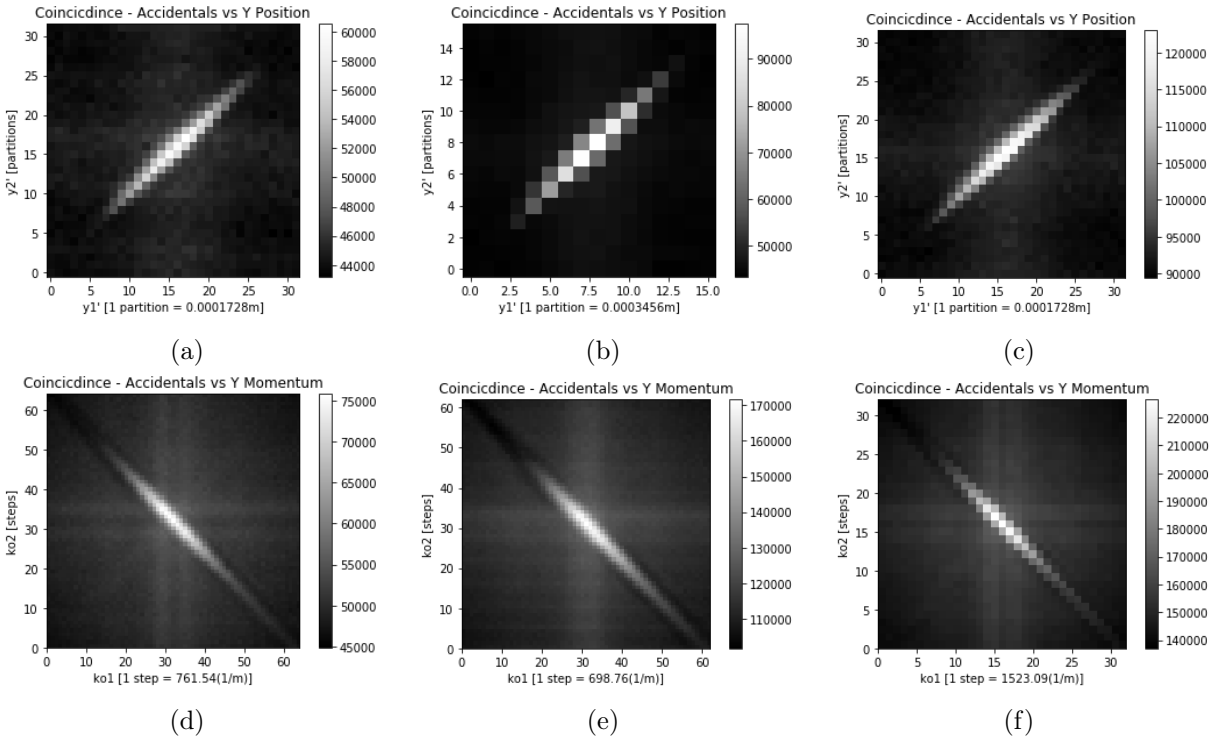

Figure B.1: (a) $t_{aq} = 15s$, $R = 32$, 45mW Pump, $\sigma_{x_-} = (1.527 \pm 0.008) \times 10^{-4}m$.
(b) $t_{aq} = 15s$, $R = 16$, 45mW Pump, $\sigma_{x_-} = (1.622 \pm 0.004) \times 10^{-4}m$.
(c) $t_{aq} = 30s$, $R = 32$, 45mW Pump, $\sigma_{x_-} = (1.500 \pm 0.005) \times 10^{-4}m$.
(d) $t_{aq} = 5s$, $R = 65$, 45mW Pump, CPWO at $\theta_x = 0.0175^o$, $\sigma_{k_+} = (1431 \pm 3)m^{-1}$.
(e) $t_{aq} = 10s$, $R = 63$, 45mW Pump, CPWO at $\theta_x = 0.01875^o$, $\sigma_{k_+} = (1538 \pm 2)m^{-1}$,
(f) $t_{aq} = 15s$, $R = 33$, 45mW Pump, CPWO at $\theta_x = 0.0175^o$, $\sigma_{k_+} = (1471 \pm 3)m^{-1}$

Gaussian profile on a constant noise floor when using H_2 to generate holograms. We did not see this phenomenon for H_1. As the offset in transverse momentum set by the CPWO in H_2 increases, the dip encompasses more joint momentum modes. As seen in Fig. B.2, we can reason that the lack of coincidence in the dark bands is most likely a direct result of the quantum state and its interaction with the holograms. If there was some alignment or lack of detection issues, we would expect to also see a drop in the single count rates for individual photons for those modes where we see the dip. We can also reason that all the coincidence is captured by the coincidence window, which in this case is 2ns wide, centered on bin number 186. It is interesting that the accidentals also provide no information on the structure of the dips. Further investigation into the biphoton state that leaves the DMDs could be made to identify whether the modes encompassed by the dips are in fact not present in the quantum state as a result of using H_2 or if the lack of coincidence is due to some mechanism attributed to alignment and matched filtering.

B.3 Position Measurements Using CPWO

We also performed a joint position scan where the partitions were further modulated by the binary hologram for a transverses momentum offset, as in Fig. B.3 (a). This may be a useful type of measurement for future experiments where the coupling mechanism is strongly dependent on the shift in the ideal detection window imposed by the CPWO for joint transverse momentum scans. This way both the position and the momentum projections are both offset by the same transverse momentum component. The result is a valid position correlation measurement, as in Fig. B.3 (b).

Full Data set for Coincidence Dip Investigation

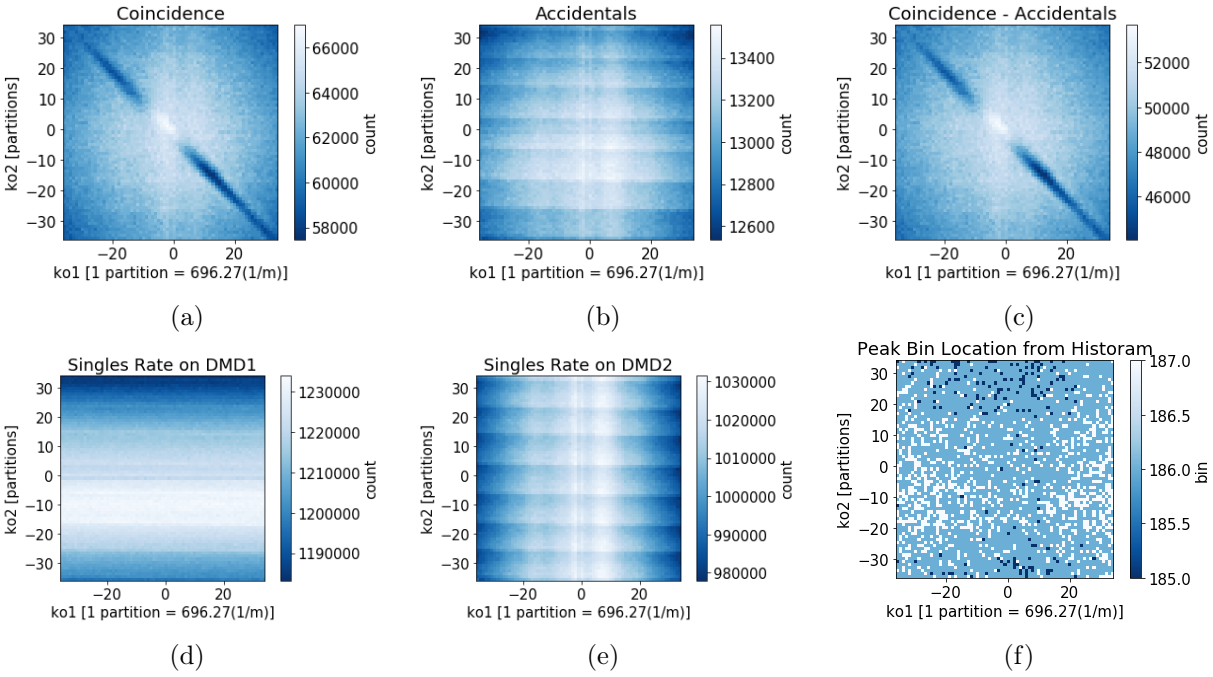

Figure B.2: Joint momentum data taken with H_2 with a CPWO of $\theta_x = 0.0475$. Striations in the accidentals and singles rates are a result of fluctuations in pump power, which are more easily visible when total scan times are long, particularly long acquisition time along with high resolution.

Joint Position Measurements Using a CPWO

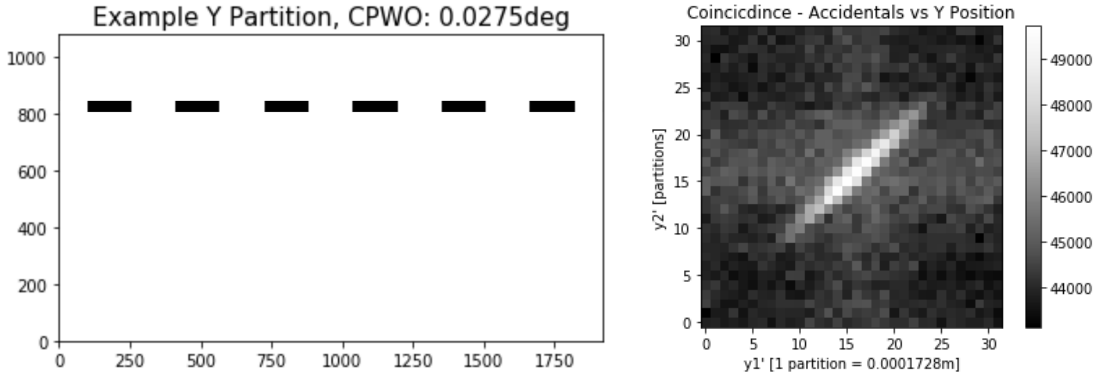

Figure B.3: (a) A sample of a position partition that is displayed on the DMD modulated by a CPWO corresponding to $\theta_x = 0.0275^o$. (b) Joint position scan using the CPWO, $t_{aq} = 15s$, $R = 32$. The resulting correlation width from a double Gaussian fit is $\sigma_{x_-} = (1.85 \pm 0.03) \times 10^{-4} m$

Appendix C

Addition Calculations

C.1 Spherical Component Holograms and Applications

Among the object fields that can be encoded in a hologram, that of a spherical wavefront is especially interesting. A spherical object wavefront with unit amplitude is defined by Goodman [39] as :

$$a(x,y) = \exp\left(ik\sqrt{f^2 + (x-x_0)^2 + (y-y_0)^2}\right) \tag{3.1.1}$$

We will call a spherical wavefront whose focal point is f $S(f)$, the x and y dependence is implied. In the paraxial regime, this field can be approximated as a parabolic wavefront:

$$S(f) = \exp\left(ik\left(\frac{(x-x_0)^2}{2f} + \frac{(y-y_0)^2}{2f}\right)\right) \tag{3.1.2}$$

Table C.1 includes various holograms that we explored the potential use for throughout this experiment. Notice that in the paraxial regime, $S(f)^* = S(-f)$, therefore we can write Case G from Table C.1. When illuminated by a columnated laser and viewed on a plane $z = f$ away from the hologram, the hologram Case G will produce a hologram component that is in focus and another that is out of focus, both centered on the optical axis. In order to vary the focal point in transverse coordinates in the plane $z = f$, we show that shifting the transverse coordinates of the center of the spherical object is equivalent to shifting the wavefront by a

Case	$A(x,y)$	$a(x,y)$	$H(x,y)$
A	$A(x)$	$a(x)$	$\|A\|^2 + \|a\|^2 + aA^* + a^*A$
B	$e^{ik_C x}$	$a(x)e^{ik_o x}$	$1 + \|a\|^2 + ae^{ix(-k_C+k_o)} + a^*e^{ix(k_C-k_o)}$
C	$e^{ik_C x}$	$a(x)$	$1 + \|a\|^2 + ae^{ix(-k_C)} + a^*e^{ix(k_C)}$
D	1	$a(x)e^{ik_o x}$	$1 + \|a\|^2 + ae^{ix(k_o)} + a^*e^{ix(-k_o)}$
E	1	$a(x)$	$1 + \|a\|^2 + a + a^*$
F	1	$e^{ik_o x}$	$2 + e^{ix(k_o)} + e^{ix(-k_o)}$
G	1	$S(f)$	$2 + S(f) + S(-f)$
H	1	$S(f)e^{ik_o x}$	$2 + S(f)e^{ix(k_o)} + S(-f)e^{ix(-k_o)}$
I	1	$e^{ik_C y}e^{ik_o x}$	$2 + e^{iy(k_C)}e^{ix(k_o)} + e^{iy(-k_C)}e^{ix(-k_o)}$

Table C.1: Holograms used though out this project for testing and measurements. The convention k_C is used for CPWO terms, where the shift in momentum is typically a constant in an experiment. k_o is used in the representation of the object field, which we typically vary in an experiment.

CPWO.

We can solve for the equivalent CPWO that corresponds to a transverse coordinate shift in the center of the spherical wavefront by equating:

$$\exp(ik_C x)S(f, x_0 = 0) = S(f : x_0 \neq 0) \tag{3.1.3}$$

Let $k_C = k\sin(\theta_C)$, we can expand:

$$\exp(ik\sin(\theta_C)\,x)\exp\left(ik\left(\frac{(x)^2}{2f}\right)\right) = \exp\left(ik\left(\frac{(x-x_0)^2}{2f}\right)\right) \tag{3.1.4}$$

Eq. 3.1.4 is solved when $\sin(\theta_C) = \frac{-x_0}{f}$. We can then choose to control the focal point by varying θ_C, the angle of the CPWO applied to the object field. Table C.1 Case H is an example of the hologram of a spherical object wavefront whose focal point is shifted in x. Notice that if the focal point, represented by $S(f)$, is shifted in the positive $\hat{x}$ direction, then the out-of-focus term $S(f-)$ will be shifted in the negative $\hat{x}$ direction. Since an illuminated hologram always produces 3 components, the out-of-focus term will always be present when encoding a spherical wavefront.

Centered and 0.25^o Offset Spherical Wavefront Holograms at Various Focal Distances

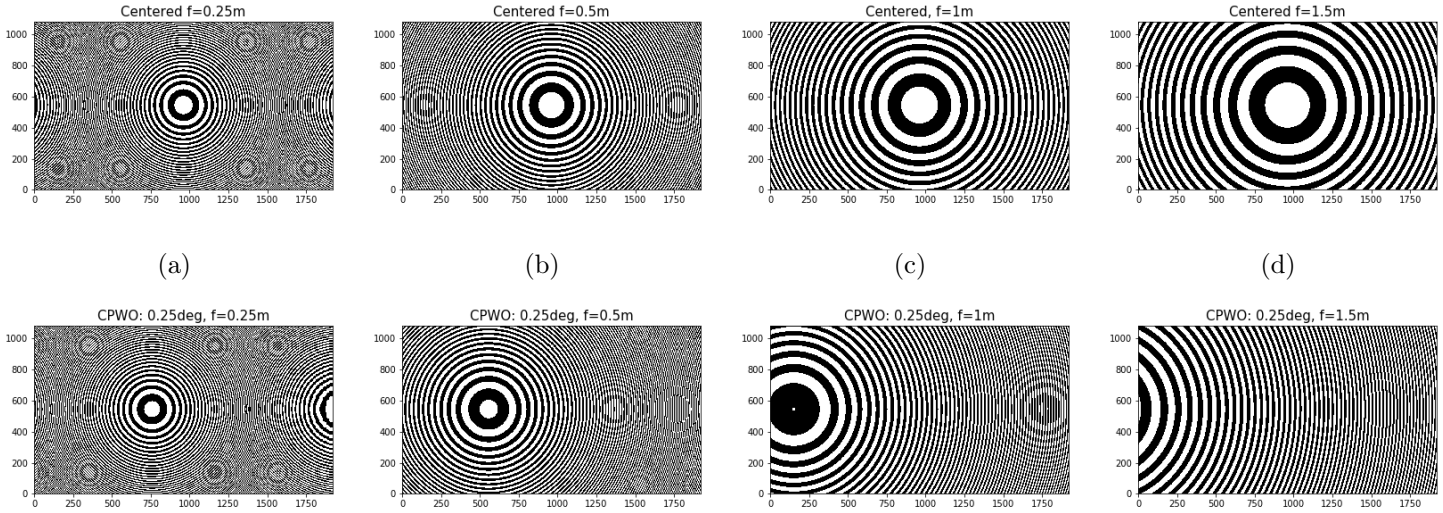

Figure C.1: (a)-(d) are binary holograms for spherical wavefronts with no transverse angular component for various focal distances. (e)-(h) are holograms for the same set of focal distances but each has a 0.25^o offset in x. We are unsure if the apparent circular patterns that arise in the high spatial frequency regions of the holograms have any effect.

From Fig. C.1 and Fig. C.2 we can see the interesting structure of the binary holograms that encode spherical wavefronts at various angle offsets and focal lengths. Most notably the aliasing effects and apparent revival of circular patterns in the holograms. We found that with a 633mn visible HeNe laser incident on a DMD displaying a spherical wavefront hologram, we can reliably produce a focused point of light at the desired location in 3D space. Recall that the diffraction imposed on the reflected field follows the diffraction grating equation $n\lambda = d \sin\theta$ where d is the separation between elements of the grating, in this case, the mirrors. We would expect for 810nm light the first diffraction order to appear 8.627^o offset from the center beam in either direction. This is a property of the DMD regardless of what is displayed. It is interesting that when we calculate the hologram for a focal point 8.627^o offset from the center, as in Fig. C.2 (e), rather than a high spatial frequency pattern we might expect for a large diffraction angle, we get a complete revival of what looks like a centered spherical hologram, as in Fig. C.1 (c). Since each diffraction order gets its own copy of the three hologram components,

Select Angle Offset for Spherical Wavefront Holograms at $f = 1m$

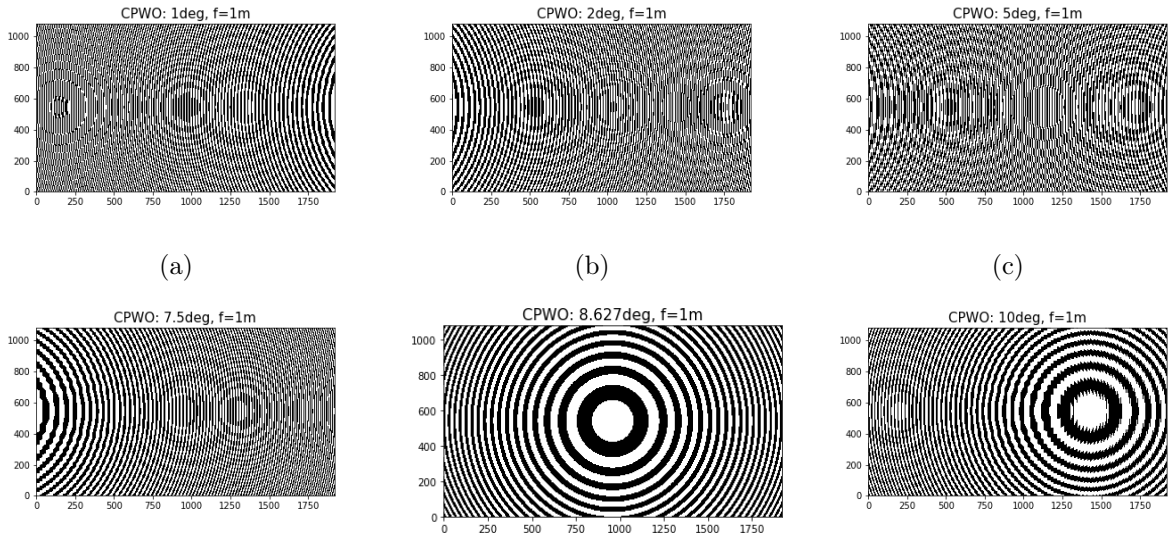

Figure C.2: Binary holograms for spherical wavefronts with significant angular offset. Each Hologram is calculated for $f = 1m$.

when we offset the focal point by a multiple of the angular diffraction spacing, the focal point appears as if it were not offset at all. We are interested to see if this technique can be used for the production of arbitrary 3D fields as well as sensing technology.

C.2 Effect of Optical Magnification on Correlation Widths

The ray transfer matrix for the optical system with magnification $M = 5$ from the NLC to the DMD is exactly:

$$\begin{bmatrix} x' \\ \theta' \end{bmatrix} = \begin{bmatrix} -5 & 0 \\ -\frac{1}{100} & -\frac{1}{5} \end{bmatrix} \times \begin{bmatrix} x \\ \theta \end{bmatrix}$$

Where the primed variables represent the coordinate and angle in the plane of the DMD and the unprimed variables for the plane of the crystal. In the paraxial regime, we can drop the x dependence for θ'. We can also say that $k_i = k \sin\theta_i \approx k\theta_i$. The resulting coordinate transformation associated with the magnification is:

$$x_i' = Mx_i \tag{3.2.5}$$

$$k_i' = \frac{k_i}{M} \tag{3.2.6}$$

We can substitute the magnification relations into the biphoton EPR state Eq. 2.3.22 and 2.3.23 and determine the relationship between the correlation width before and after magnification. First, we write:

$$\Phi(k_1', k_2') = N_k \exp\left(-\frac{(Mk_1' - Mk_2')^2}{8\sigma_{k_-}^2}\right) \exp\left(-\frac{(Mk_1' + Mk_2')^2}{8\sigma_{k_+}^2}\right) \tag{3.2.7}$$

$$\Psi(x_1', x_2') = N_x \exp\left(-\frac{(\frac{x_1'}{M} - \frac{x_2'}{M})^2}{8\sigma_{x_-}^2}\right) \exp\left(-\frac{(\frac{x_1'}{M} + \frac{x_2'}{M})^2}{8\sigma_{x_+}^2}\right) \tag{3.2.8}$$

Call the correlation widths we measure in the measurement plane $\sigma_{x\pm}'$ and $\sigma_{k\pm}'$. We then write the state fully defined in terms of the variables in the measurement plane:

$$\Phi(k_1', k_2') = N_k \exp\left(-\frac{(k_1' - k_2')^2}{8{\sigma_{k_-}'}^2}\right) \exp\left(-\frac{(k_1' + k_2')^2}{8{\sigma_{k_+}'}^2}\right) \tag{3.2.9}$$

$$\Psi(x_1', x_2') = N_x \exp\left(-\frac{(x_1' - x_2')^2}{8{\sigma_{x_-}'}^2}\right) \exp\left(-\frac{(x_1' + x_2')^2}{8{\sigma_{x_+}'}^2}\right) \tag{3.2.10}$$

We determine that the relationship between the correlation widths in the measurement plane and the plane of the NLC is:

$$\sigma_{x_\pm}' = M\sigma_{x_\pm} \tag{3.2.11}$$

$$\sigma_{k_\pm}' = \frac{\sigma_{k_\pm}}{M} \tag{3.2.12}$$

It is clear that the individual correlation widths are scaled by a factor of M. When we

evaluate the variance product, we see that the magnification of the system does not affect the strength of the violation of the locality condition:

$$\sigma'_{x_-}\sigma'_{k_+} = M\sigma_{x_-}\frac{\sigma_{k_+}}{M} = \sigma_{x_-}\sigma_{k_+} \tag{3.2.13}$$

Therefore the locality conditions and entanglement witnesses from Table 2.1 do not change form in the measurement plane. We choose to represent our findings in Sec. 5 in terms of the correlations in the plane of the NLC as it provides a straightforward comparison to the theoretical values predicted by the SPDC state.

Bibliography

[1] A. Einstein, B. Podolsky, and N. Rosen. Can quantum-mechanical description of physical reality be considered complete? *Phys. Rev.*, 47:777–780, May 1935. 1.1.1

[2] E. G. Cavalcanti, S. J. Jones, H. M. Wiseman, and M. D. Reid. Experimental criteria for steering and the einstein-podolsky-rosen paradox. *Phys. Rev. A*, 80:032112, Sep 2009. 1.1.1, 1.1.1

[3] Ryszard Horodecki, Paweł Horodecki, Michał Horodecki, and Karol Horodecki. Quantum entanglement. *Rev. Mod. Phys.*, 81:865–942, Jun 2009. 1.1.1

[4] David McIntyre. *Quantum Mechanics: A Paradigms Approach*. Pearson, first edition, 1 2012. 1.1.1, 2.1, 2.1, 2.1

[5] Nicolas Brunner, Daniel Cavalcanti, Stefano Pironio, Valerio Scarani, and Stephanie Wehner. Bell nonlocality. *Rev. Mod. Phys.*, 86:419–478, Apr 2014. 1.1.1

[6] Charles H. Bennett and Gilles Brassard. Quantum cryptography: Public key distribution and coin tossing. *Theoretical Computer Science*, 560:7–11, 2014. Theoretical Aspects of Quantum Cryptography – celebrating 30 years of BB84. 1.1.1

[7] Artur K. Ekert. Quantum cryptography based on bell's theorem. *Phys. Rev. Lett.*, 67:661–663, Aug 1991. 1.1.1

[8] S. P. Walborn, D. S. Lemelle, D. S. Tasca, and P. H. Souto Ribeiro. Schemes for quantum key distribution with higher-order alphabets using single-photon fractional fourier optics. *Phys. Rev. A*, 77:062323, Jun 2008. 1.2

[9] S. P. Walborn, D. S. Lemelle, M. P. Almeida, and P. H. Souto Ribeiro. Quantum key distribution with higher-order alphabets using spatially encoded qudits. *Phys. Rev. Lett.*, 96:090501, Mar 2006. 1.2

[10] Leonardo Neves, G. Lima, J. G. Aguirre Gómez, C. H. Monken, C. Saavedra, and S. Pádua. Generation of entangled states of qudits using twin photons. *Phys. Rev. Lett.*, 94:100501, Mar 2005. 1.2

[11] M. A. Solí s-Prosser, A. Arias, J. J. M. Varga, L. Rebón, S. Ledesma, C. Iemmi, and L. Neves. Preparing arbitrary pure states of spatial qudits with a single phase-only spatial light modulator. *Optics Letters*, 38(22):4762, nov 2013. 1.2

[12] Cosmo Lupo. Towards practical security of continuous-variable quantum key distribution. *Phys. Rev. A*, 102:022623, Aug 2020. 1.2

[13] Mitchell A. Cox and Alice V. Drozdov. Converting a texas instruments dlp4710 dlp evaluation module into a spatial light modulator. *Appl. Opt.*, 60(2):465–469, Jan 2021. 1.2, 3.1.3, 4.1.6

[14] Xinchao Ruan, Wenhao Shi, Guojun Chen, Wei Zhao, Hang Zhang, and Ying Guo. High-rate continuous-variable quantum key distribution with orbital angular momentum multiplexing. *Entropy*, 23(9), 2021. 1.2

[15] Daniele Cozzolino, Davide Bacco, Beatrice Da Lio, Kasper Ingerslev, Yunhong Ding, Kjeld Dalgaard, Poul Kristensen, Michael Galili, Karsten Rottwitt, Siddharth Ramachandran, and Leif Katsuo Oxenløwe. Orbital angular momentum states enabling fiber-based high-dimensional quantum communication. *Phys. Rev. Applied*, 11:064058, Jun 2019. 1.2

[16] Vijay S. S. Sundaram. *Integration of a Visible-Telecom Photon Pair Source with Silicon Photonics for Quantum Communication.* PhD thesis, Rochester Institute of Technology, 2021. 1.2

[17] Baptiste Courme, Patrick Cameron, Daniele Faccio, Sylvain Gigan, and Hugo Defienne. Manipulation and certification of high-dimensional entanglement through a scattering medium. *arXiv*, 7 2022. 1.2

[18] Lukas Achatz, Evelyn A Ortega, Krishna Dovzhik, Rodrigo F Shiozaki, Jorge Fuenzalida, Sören Wengerowsky, Martin Bohmann, and Rupert Ursin. Certifying position-momentum entanglement at telecommunication wavelengths. *Physica Scripta*, 97(1):015101, jan 2022. 1.2

[19] Zhan Zheng, Hailong Wang, Bing Cheng, and Jietai Jing. Entanglement in a four-wave mixing process. *Opt. Lett.*, 42(14):2754–2757, Jul 2017. 1.2

[20] Robert W. Boyd. *Nonlinear Optics*. Academic Press, fourth edition, 4 2020. 1.2, 2.2.1, 2.2.1, 2.2.2, 2.2.2

[21] J. J. Sakurai and Jim Napolitano. *Modern Quantum Mechanics*. Cambridge University Press, third edition, 10 2020. 2.1, 2.1

[22] M. D. Reid, P. D. Drummond, W. P. Bowen, E. G. Cavalcanti, P. K. Lam, H. A. Bachor, U. L. Andersen, and G. Leuchs. Colloquium: The einstein-podolsky-rosen paradox: From concepts to applications. *Rev. Mod. Phys.*, 81:1727–1751, Dec 2009. 2.1

[23] Christopher Gerry and Peter Knight. *Introductory Quantum Optics*. Cambridge University Press, 2004. 2.2.1

[24] James Schneeloch and John C Howell. Introduction to the transverse spatial correlations in spontaneous parametric down-conversion through the biphoton birth zone. *Journal of Optics*, 18(5):053501, apr 2016. 2.2.2, 2.3, 2.3, 2.4, 3.1.6, A

[25] Keiichi Edamatsu. Entangled photons: Generation, observation, and characterization. *Jpn. J. Appl. Phys*, 46:865–942, Jun 2007. 2.2.2

[26] Coherent Connection. Cube - compact diode laser modules. 3.1.1, 5.1.2

[27] PCO Pixelfly. pco.pixelfly usb ultra-compact 14 bit ccd camera, Jun 2019. 3.1.1

[28] Excelitas Technologies. SPCM-AQ4C - single photon counting module 4 channel array data sheet. 3.1.2, 3.1.2

[29] Swabian Instruments. Time tagger user manual. 3.1.2

[30] Texas Instruments. DLP DLCR4710EVM-G2 - full HD DLP4710 chipset evaluation module. 3.1.3

[31] Texas Instruments. DLP4710 - DLP® 0.47 1080p DMD. 3.1.3, 5.1.1

[32] Ayman F. Abouraddy, Bahaa E. A. Saleh, Alexander V. Sergienko, and Malvin C. Teich. Entangled-photon fourier optics. *J. Opt. Soc. Am. B*, 19(5):1174–1184, May 2002. 3.1.7

[33] James Schneeloch, Christopher C. Tison, Michael L. Fanto, Paul M. Alsing, and Gregory A. Howland. Quantifying entanglement in a 68-billion-dimensional quantum state space. *Nature Communications*, 10(1):2785, Jun 2019. 4.1.1

[34] John C. Howell, Ryan S. Bennink, Sean J. Bentley, and R. W. Boyd. Realization of the einstein-podolsky-rosen paradox using momentum- and position-entangled photons from spontaneous parametric down conversion. *Phys. Rev. Lett.*, 92:210403, May 2004. 4.1.1

[35] Paul-Antoine Moreau, Fabrice Devaux, and Eric Lantz. Einstein-podolsky-rosen paradox in twin images. *Phys. Rev. Lett.*, 113:160401, Oct 2014. 4.1.1

[36] M. P. Edgar, D. S. Tasca, F. Izdebski, R. E. Warburton, J. Leach, M. Agnew, G. S. Buller, R. W. Boyd, and M. J. Padgett. Imaging high-dimensional spatial entanglement with a camera. *Nature Communications*, 3(1):984, Aug 2012. 4.1.1

[37] Hugo Defienne, Matthew Reichert, and Jason W. Fleischer. General model of photon-pair detection with an image sensor. *Phys. Rev. Lett.*, 120:203604, May 2018. 4.1.1

[38] Lukas Achatz, Evelyn A Ortega, Krishna Dovzhik, Rodrigo F Shiozaki, Jorge Fuenzalida, Sören Wengerowsky, Martin Bohmann, and Rupert Ursin. Certifying position-momentum entanglement at telecommunication wavelengths. *Physica Scripta*, 97(1):015101, jan 2022. 4.1.1

[39] Joseph W Goodman. *Introduction To Fourier Optics*. McGraw-Hill Science/Engineering/Math, second edition, 1 1996. 4.1.1, 4.1.2, 4.1.2, 4.1.3, 4.1.4, C.1